ELASTICITY AND PLASTICITY OF NANOPOROUS GOLD: IMPLICATIONS OF MOLECULAR DYNAMICS SIMULATIONS

Vom Promotionsausschuss der
Technischen Universität Hamburg-Harburg
zur Erlangung des akademischen Grades
Doktor-Ingenieur (Dr.-Ing.)
genehmigte Dissertation

von

DINH BAO NAM NGO

aus

HAI PHONG

2017

Erstgutachter: Prof. Jörg Weissmüller
Zweitgutachter: Prof. Karsten Albe
Vorsitzender: Prof. Erica T. Lilleodden

Tag der mündlichen Prüfung: 23. Juni 2017

urn:nbn:de:gbv:830-88217214

ACKNOWLEDGMENTS

I would like to thank all the people who have supported me and contributed to the success of this thesis over the past couple of years.

Firstly, I would like to express my sincere gratitude to my supervisor, Prof. Jörg Weissmüller, for his continuous support during my Ph.D. research. This work could not have been finished without his encouragement and patient guidance.

I would like to thank my unofficial supervisor, Prof. Karsten Albe. It is always a pleasure to learn new things in a great fun way from him.

My sincere thank also goes to Dr. Jürgen Markmann for his constant effort in mentoring youger members of our group.

I thank my fellow WMH group members for the stimulating discussions and for all the fun we have had in the last years.

Finally, I thank my family for their love, support, and understanding.

ABSTRACT

Nanoporous gold is emerging as a functional material with potential applications in many areas, such as actuation, catalysis, and sensing. The material is also a candidate for studies of mechanics at the nanoscale. This work presents an effort to investigate the elasticity and plasticity of nanoporous gold by using molecular dynamics simulations.

First, this work addresses the underlying atomistic mechanisms that govern the mechanical responses of the material by studying the uni-axial compression of a realistic nanoporous gold sample created by mimicking spinodal decomposition. In excellent agreement with the experimental data of mm-sized samples, the simulation results highlight the exceedingly weak and compliant nature of nanoporous gold. Driven by the capillary forces, the material already experiences plastic deformation prior to the onset of straining. Uniaxial deformation starts with an extended regime of elastic-plastic transition and an unusually high compliance. In addition to the material densification, subsequent plastic flow is accompanied by Taylor work hardening; the dislocation-starvation scenario is thus not supported. At the same time, the material undergoes substantial stiffening, yet the values according to the prediction of the relevant Gibson-Ashby law are never reached.

The attention is then directed to the influences of the disordered topology due to nodal shift on the behavior of the material. For that purpose, the focus is put on the behavior of the diamond-like nanoporous gold - a model suggested and justified recently as a suitable topological representation of the random interconnected network of ligaments in nanoporous metals. Under compression, both the ordered diamond-lattice sample and its disordered counterparts exhibit a well-defined elasticity with high modulus preceding the yield behavior at high strength. The current simulation data suggest a transition from stretching to bending in deformation mode of many ligaments in the network of the diamond-lattice structures when the nodal shift is introduced; though the structures are still stretch-dominated. The nodal shift has strong influence on the elastic modulus, yield strength, elastic-plastic transition, and lateral expansion of the diamond-lattice structures. Yet, not all aspects of the mechanical behavior of dealloyed nanoporous gold are captured in the diamond-lattice structures, even with the optimal nodal shift as is suggested in the previous development of the model.

Finally, the influence of the ligament connectivity on the elasticity of nanoporous gold is investigated. For that purpose, two different methods are used to create samples via mimicking spinodal decomposition, namely via Monte Carlo simulation and via superposition of composition waves. Both techniques lead to samples that resemble the ligament network of nanoporous gold. Yet, the mechanical properties of these samples are substantially different. Although the simulation data support the influence of ligament connectivity on the elastic modulus of nanoporous gold, a concrete quantitative relation between measures of connectivity and the elasticity of nanoporous gold can not be resolved. Thus, other factors must be taken into account in order to explain the anomalous compliance of nanoporous gold. Among them, surface effects play a crucial role.

CONTENTS

1 INTRODUCTION 1

2 METHODS 5
- 2.1 Sample preparation . . . 5
  - 2.1.1 Monte Carlo simulation . . . 5
  - 2.1.2 Superposition of composition waves . . . 7
- 2.2 Molecular dynamics . . . 10
- 2.3 Interatomic potential . . . 13
- 2.4 Simulation procedure . . . 13
- 2.5 Analysis of simulation data . . . 14
  - 2.5.1 Defect structures . . . 14
  - 2.5.2 Surface reconstruction . . . 16
  - 2.5.3 Analysis of ligament connectivity . . . 17
  - 2.5.4 Visualization . . . 18

3 DEFORMATION OF SPINODAL NANOPOROUS GOLD 19
- 3.1 Initial microstructure . . . 19
- 3.2 Relaxation behavior . . . 20
- 3.3 Stress-strain behavior . . . 22
- 3.4 Origin of the early yielding . . . 23
- 3.5 Transverse strain and surface area . . . 26
- 3.6 Defect structures and strain hardening . . . 27
- 3.7 Evolution of effective Young's modulus . . . 30
- 3.8 Summary . . . 32

4 DEFORMATION OF DIAMOND-LATTICE STRUCTURES 33
- 4.1 Diamond-lattice structure as a topological representation of NPG . 33
- 4.2 Atomistic diamond-lattice structures . . . 35
- 4.3 Relaxation behavior . . . 37
- 4.4 Stress strain behavior . . . 37
- 4.5 Yield strength and elastic modulus . . . 38
- 4.6 Ligament deformation mode . . . 41
- 4.7 Microstructural changes . . . 42
- 4.8 Dislocation density . . . 43
- 4.9 Summary . . . 45

5 INFLUENCE OF LIGAMENT CONNECTIVITY ON ELASTIC MODULUS 47
5.1 A missing brick in the Gibson-Ashby scaling law: ligament connectivity 47
5.2 Microstructures and stress-strain behavior 49
5.3 Evolution of elastic modulus 51
5.4 Evolution of connectivity 52
5.5 Elastic modulus *vs.* scaled connectivity density 55
5.6 Influence of surface effects 58
5.7 Summary 60

6 SUMMARY AND OUTLOOK 63

REFERENCES 65

LIST OF PUBLICATIONS 75

LIST OF FIGURES

Figure 1.1 Micrograph of a nanoporous gold structure created by dealloying. This structure has ligament size of 63 ± 6 nm and solid fraction of 0.26 ± 0.01. Note the disordered network of ligaments. Reprinted from N. Huber *et al.* Acta Materialia 67 (2014): 252-265, with permission from Elsevier. 1

Figure 1.2 Typical stress strain curve of mm-sized nanoporous gold samples. This Figure depicts the experimental stress-strain curve (interspersed with unload segments) of the sample shown in Figure 1.1. The inset illustrates the calculation of the effective elastic moduli (as tangent moduli [23]) from the unload segments. Reprinted from N. Huber *et al.* Acta Materialia 67 (2014): 252-265, with permission from Elsevier. 2

Figure 2.1 Two-dimensional square-lattice Ising model. Pair interaction is ϵ_{AB} between A and B, 0 otherwise. Site i has 2 neighbors of type A and 2 neighbors of type B. The energy associated with i is thus ϵ_{AB}. Since this configuration has 10 A–B bonds, its energy is $10\epsilon_{AB}$. 6

Figure 2.2 Example of NPG sample created via mimicking spinodal decomposition by Monte Carlo simulation. (a) Initial binary mixture with 32% of A atoms (green) and 68% B of atoms (red). (b) Phase separation lead to a structure that consists of two intertwined networks of A atoms and B atoms. (c) A porous structure with solid fraction of 0.32 was obtained after removing all B atoms. For brevity, surface and bulk atoms in (c) are coded in different colors. . . 7

Figure 2.3 Example of NPG sample created via superposition of composition waves. Figure (a) shows the color-coded composition. This composition was generated from 48 waves. (b) After imposing a threshold on the composition, we obtained a nanoporous structure with solid fraction of 32%. Figure (c) shows an example of a textured structure obtained from only 6 composition waves. 9

Figure 2.4 Close-ups of the surface of samples shown in Figure 2.2c (left) and Figure 2.3b (right) reveal different surface roughness. Sample created by superposition of composition waves exhibits smoother surface. 10

Figure 2.5 Illustration of the common neighbor analysis (CNA) method. Figure (a) shows a configuration in which we want to analyze the local crystal structure of the central atom (blue). Figure (b) shows bonds between nearest neighbors found in this configuration (within a predefined cutoff radius). The central atom has 12 nearest neighbors. Between the central atom and one of its nearest neighbors (e.g. atom coded in red in Figure (c)), there are $N_{\mathrm{cn}} = 4$ common neighbors (green). $N_{\mathrm{b}} = 2$ bonds are found in these common neighbors (red), with the maximum length of bond chain, N_{lb}, is 1. From these numbers, the local crystal structure is determined as FCC. 15

Figure 2.6 Illustration of the work flow of the Dislocation Extraction Algorithm (DXA). The top-left figure shows a BCC single crystal with lattice defects. From the point cloud representing the atoms, a Delaunay tessellation was generated, with constituent tetrahedra classified as 'good' or 'bad' regions (top-right). These regions are separated by a triangulated interface mesh (bottom-right). Performing Burgers circuit analysis on this interface mesh reveals a prismatic dislocation loop, as shown in the bottom-left figure. Reproduced from Stukowski *et al*. Modelling Simul. Mater. Sci. Eng. 20 (2012) 085007 with permission from AIP. 16

Figure 2.7 Illustration of surface reconstruction via the alpha-shape method (here in 2D). Figure (a) shows a point cloud whose surface is to be constructed. A Delaunay tessellation is generated which comprises triangles that fill the convex hull of the point cloud (Figure (b)). These triangles are marked as 'solid' (grey) if their radius is less than a given probe radius R_{b}, and open space (magenta) if otherwise. Removing the open space region and extracting the surface mesh of the solid region gives us a reconstructed surface (red) of the point cloud (Figure (c)). 17

Figure 2.8 Example of genus of some typical shapes. Genus of a sphere (a) is 0 since it has no handle. A 2-ring torus (b) has two handles and its genus is therefore 2. If one of the two rings of the 2–ring torus is broken (c), there is one handle left; the corresponding genus is thus 1. 18
Figure 3.1 Initial microstructure (a) and reconstructed surface (b) of the NPG studied in this Chapter. This structure was created by mimicking spinodal decomposition via Monte Carlo simulation (see Chapter 2). The sample length is 40.8 nm. Its solid fraction and ligament size are 0.297 and 3.15 nm, respectively. 20
Figure 3.2 Examples of lattice defects in the thermally relaxed (at $T = 300$ K) configuration of the virtual NPG structure shown in Figure 3.1. These pre-existing defects are due to the action of the capillary forces which lead to plasticity even without any help from external load. 21
Figure 3.3 Influence of surface stress on local stress distribution. Figure at left and at right show the local von Mises stress of atoms in the NPG sample before and after the initial energy minimization, respectively. While no dislocations were found in the athermally relaxed structure, bulk atoms already experienced significant stress concentration. Changes are more accentuated where atoms are near the surface or at the thinner part of ligaments. 22
Figure 3.4 Simulated stress–true strain curves ($\sigma - \varepsilon$) of the virtual NPG sample shown in Figure 3.1 at $T = 300$ K (a) and $T = 0.01$ K (b). Red curves are for continuous uni-axial loading. In blue curves, unload segments were interspersed to monitor the evolution of effective elastic modulus. Note the extended elastic-plastic transition followed by pronounced strain hardening. 23
Figure 3.5 Tension-compression asymmetry in behavior of NPG under opposite loading directions. Here shows the stress, σ, versus true strain, ε, of an NPG sample with ligament size of 3.76 nm and solid fraction of 0.302 (see Chapter 5 for details). Tensile strength is 40 MPa, which is almost 3–fold the value of 15 MPa of the strength in compression. 25

Figure 3.6 True transverse strain, $\varepsilon_{\text{trans}}$, vs. true axial strain, ε, of the NPG sample depicted in Figure 3.1 during the deformation event shown in Figure 3.4a. The transverse strain remains small for a wide range of the axial strain. Figure at right shows the sample (reconstructed surface) at $\varepsilon = 0.69$, along with the simulation box prior to the onset of straining (red frame). Note the negligible changes in the lateral dimensions. 26
Figure 3.7 Change of specific surface area, α, of the NPG sample depicted in Figure 3.1 during the deformation event shown in Figure 3.4a. Here, α is scaled to the initial value, α_0, prior to the onset of straining. This graph also shows experimental data of dealloyed NPG samples with ligament size of 53 nm and 29 nm, and solid fraction of 0.266 and 0.260, respectively. Note the loss of surface area of (virtual and experimental) NPG samples. Figures outside the graph illustrate the cold coalescence of ligaments in the virtual NPG sample. At true strain $\varepsilon = 0.073$, two ligaments in the red circle are still at a distance apart. Deformation brings these ligaments towards each other and ultimately welds them at the surface, as is illustrated in the close-up of the surface at $\varepsilon = 0.094$. Experimental data courtesy of Dr. N. Mameka at Helmholtz-Zentrum Geesthacht. 27
Figure 3.8 Evolution of fault density of the NPG sample depicted in Figure 3.1 during the deformation event shown in Figure 3.4a. (a) Accumulation of dislocation density during compression at 300 K. Main contribution comes from Shockley partials. (b) As a result of dislocation activity, twin boundaries and stacking faults populate during compression. Dislocations are already present before the onset of straining, and get their activity immediately upon loading. 28

Figure 3.9 Typical defect structures found in the virtual NPG under compression. Left plot shows a slice cutting through sample at the true compressive strain of 0.80. Loading direction is perpendicular to the plot plane. Magnifications of circled regions are shown on the right, depicting examples of grain boundaries (top) and Lomer–Cottrell locks (bottom) found in the deformed structure. Plasticity happens not only at the ligament junctions, but also in the middle of ligaments. 29
Figure 3.10 Change of effective Young's modulus, Y^{eff}, of NPG during compression. Figure (a) shows the absolute values of Y^{eff} versus true strain, ε. The scaled values of Y^{eff} (to the Young's modulus Y^{bulk} of massive polycrystalline gold) are shown versus the square of solid fraction, φ, in Figure (b). Gibson–Ashby scaling law is also superimposed in (b), along with experimental data from compression test of a dealloyed NPG with ligament size of 40 nm and solid fraction of 0.298 (see Ref. [71] for details). Note the agreement between simulation and experiment. As is clearly seen in this plot, the evolution of Y^{eff} is characterized by two features: exceptionally high initial compliance and ensuing stiffening under compression. At any time during compression, NPG is much more compliant than the prediction of Gibson–Ashby law. Experimental data courtesy of Dr. N. Mameka at Helmholtz-Zentrum Geesthacht. 31
Figure 4.1 Diamond-lattice structure as topological representation of NPG. (a) A micro-graph of experimental NPG shows typical connections at ligament nodes. These connections can be represented by a tetrahedron with spherical nodes at the center and at the vertexes, and ligaments connecting the center with the vertexes. (b) With tetrahedra as building blocks, the unit cell of the representative volume takes the form of a diamond lattice. In this sketch, a, r, R, and l denote the length of a unit cell, ligament radius, node radius, and node-to-node distance, respectively. (c) An ordered diamond-lattice structure. (d) Displacing the node positions of the ordered structure results in a more realistic disordered structure. Figures (a), (c), and (d) are reprinted from N. Huber et al. Acta Materialia 67 (2014): 252-265, with permission from Elsevier. 34

Figure 4.2 Atomistic ordered and disordered diamond-lattice structures studied in this Chapter. Figure (a) shows the ordered diamond-lattice structure created from 4 unit cell. The as-created solid fraction of this structure is 0.302. Figures (b) and (c) depict disordered diamond-lattice structures with as-created solid fraction of 0.358 and 0.301, respectively. A random factor of 0.23 was used to create both samples shown in (b) and (c). 36

Figure 4.3 Simulated stress-true strain (σ-ε) curves of diamond-lattice structures. Unloading segments were interspersed to monitor the evolution of effective elastic modulus. All curves exhibit elastic regimes before yielding. Note that the elastic regimes of the ordered sample $A^{0}_{0.303}$ and the disordered sample $A^{0.23}_{0.360}$ are visually indistinguishable. These curves were simulated with a strain rate of 10^8/s at 300 K. 38

Figure 4.4 Evolution of effective elastic modulus, Y^{eff}, of diamond-lattice structures with stress-strain curves shown in Figure 4.4. ε denotes true strain. All structures show very high initial stiffness. More remarkably, these structures show drastic decrease in the elastic modulus, irrespective of whether or not the nodal shift is introduced. Thus, the stiffening behavior usually observed in experimental NPG samples, as well as in the spinodal decomposition NPG sample reported in Chapter 3, is not reproduced in the diamond-lattice structures. 40

Figure 4.5 True transverse strain, $\varepsilon_{\mathrm{trans}}$, vs. true axial strain, ε, of the diamond-lattice structures during the deformation event shown in Figure 4.3. Short line segments in this plot are from the unload segments during the simulated compression tests. This plot shows that the nodal shift has strong influence on the evolution of $\varepsilon_{\mathrm{trans}}$, though the small lateral expansion observed in experimental NPG is never reproduced. 43

Figure 4.6 Change of specific surface area, α, of the diamond-lattice NPG samples during the deformation event shown in Figure 4.3. Here, α is scaled to the initial value, α_0, prior to the onset of straining. Short line segments in this plot are from the unload segments during the simulated compression tests. For the ordered sample, α decreases in the elastic regime and increases in the plastic regime. Introducing the nodal shift inverts the behavior of α completely: Both disordered samples show decreasing α during the deformation process. 44

Figure 4.7 Evolution of dislocation densities of the ordered diamond-lattice sample and its disordered counterparts during the deformation event shown in Figure 4.3. No dislocation densities were detected in the ordered for true strains $\varepsilon \lesssim 0.05$. Pre-existing dislocation densities were found in the disordered samples prior to the onset of straining and remains almost constant for $\varepsilon \lesssim 0.01$. The ordinate is broken from 2×10^{13} to 10^{14}. Ordinate intervals below and above this broken range are linear-scale and log-scale, respectively. 45

Figure 4.8 Examples of lattice defects in the ordered sample $A^{0}_{0.303}$ and the disordered sample $A^{0.23}_{0.303}$ at the compressive true strain of 0.2. Loading direction is in the x direction. The magnifications exemplifies the observation that plasticity happens not only locally at the transition from the ligaments to the nodes, but also at the middle of the ligaments. To help visualize the results, only halves of the simulation boxes (divided by the rectangles made of opposite edges and face diagonals) are shown. 46

Figure 5.1 Influence of ligament connectivity on the effective solid fraction of NPG. Figure at left illustrates an NPG sample with solid fraction φ. Many ligaments in this sample are broken, resulting in dangling ligaments (grey) which have one end hanging about in the pore space. These dangling ligaments are not responsive to the external load applied on the sample. Other unbroken ligaments (yellow) form load-bearing rings and thus collectively respond to the external load. The behavior of the system at left is therefore equivalent to the behavior of a counterpart system (with effective solid fraction φ_{eff}) in which all dangling ligaments are removed (right). Reprinted from Liu *et al.* Acta Materialia 118 (2016): 77-87, with permission from Elsevier. 48
Figure 5.2 Examples of the initial microstructure of samples studied in this Chapter. These samples were created via mimicking spinodal decomposition by (a) Monte Carlo simulation and by (b) superposition of 48 composition waves. For simulation details, see Chapter 2. Both samples have the same as-created solid fraction $\varphi_{\text{ini}} = 0.302$. Note the disordered network of both samples. For brevity, surface atoms and bulk atoms are coded in different colors. 50
Figure 5.3 Simulated stress–true strain (σ–ε) curves of samples created by Monte Carlo (MC) simulation (green) and wave (W) method (red). Wave samples are much stronger than MC samples of similar solid fraction. These stress-strain curves were simulated with a strain rate of 10^8/s at 300 K. 52
Figure 5.4 Evolution of effective elastic modulus, Y^{eff}, of samples with simulated stress-strain curves shown in Figure 5.3. All samples exhibit substantial stiffening as the deformation proceeds. Wave samples are much stiffer than MC samples of similar solid fraction. 53
Figure 5.5 Comparing simulation data (points) with prediction of the Gibson–Ashby scaling law for elastic modulus (blue lines). Gibson-Ashby law fails to predict not only the initial modulus but also the value of Y^{eff} at different strain stages when the material has already experienced substantial stiffening. 53

Figure 5.6 Evolution of connectivity during deformation. Figures (a) and (b) show the genus density, g_V, and absolute change of genus, Δg, of spinodal decomposition samples during the deformation events shown in Figure 5.3. Note the substantial increase of g_V of all samples during the deformation. This increase is mostly due to formation of new ligament connections, as quantified in (b), as well as exemplified in Figure 3.7. 54

Figure 5.7 Change of scaled genus density of spinodal decomposition samples during the deformation events shown in Figure 5.3. Both definitions of scaled connectivity, namely (a) $g_\mathrm{scaled} = g_\mathrm{V} S_\mathrm{V}^{-3}$ and (b) $\widetilde{g}_\mathrm{scaled} = g_\mathrm{V} \alpha^{-3}$ (see main text for details), are shown. Except for sample MC–0.308, g_scaled decreases during the deformation. $\widetilde{g}_\mathrm{scaled}$ of all samples, on the other hand, increases substantially during the deformation. 56

Figure 5.8 Pre-factor, C_E, in the Gibson-Ashby scaling law versus scaled genus density. This figures are for data points at zero strain. Results for both definitions of scaled connectivity, namely (a) $g_\mathrm{scaled} = g_\mathrm{V} S_\mathrm{V}^{-3}$ and (b) $\widetilde{g}_\mathrm{scaled} = g_\mathrm{V} \alpha^{-3}$ (see main text for details), are shown. The linear relation $C_\mathrm{E} = 5 g_\mathrm{scaled}$ [38] is also shown in (a). No one-to-one relations between the pre-factor and the scaled genus density can be recovered from the present data set. 57

Figure 5.9 Pre-factor, C_E, in the Gibson-Ashby scaling law versus scaled genus density, with $\widetilde{g}_\mathrm{scaled} = g_\mathrm{V} \alpha^{-3}$ (see main text for details), during the deformation events of Figure 5.3. Similar to Figure 5.8, no one-to-one relations between the prefactor and scaled connectivity can be recovered from the data set of this figure. 58

Figure 5.10 Influence of nonlinear effects. Effective Young's modulus, Y_eff, versus plastic strain, ε. Data from molecular dynamics (MD) and linear-elastic finite element method (FEM) simulations for sample MC–0.308. Note the substantially stiffer behavior of the linear elastic solid, in spite of identical network geometry. 60

Figure 5.11 Schematic illustration of shear instability. Graph at left shows the generalized stacking fault energy function, γ, versus shear displacement, u, between adjacent atomic planes. Graph at right shows the associated variation of the shear modulus, G, which scales with the second derivative of $\gamma(u)$. The negative-valued second derivative between the points of inflection of $\gamma(u)$ implies instability to shear. . . 61

1

INTRODUCTION

Nanoporous gold (NPG) has attracted much discussion, thanks to its wide range of potential applications in actuation [1–6], catalysis [7, 8], and sensing [9, 10]. Usually fabricated by selective dissolution, NPG takes the form of an interconnected network of ligaments (Figure 1.1) whose diameter can be tuned between few ten nanometers to few microns [11–13] with long-distance crystallographic coherency [14, 15]. As such, NPG is an excellent candidate for an implementation of mechanical properties of nanoscale wires and pillars into a bulk system, thereby allowing probes into mechanics at the nanoscale from the macroscopic level.

From a mechanical standpoint, bulk NPG is very deformable under compression load [13, 15–18]: Samples of millimeter sizes can be deformed to very large

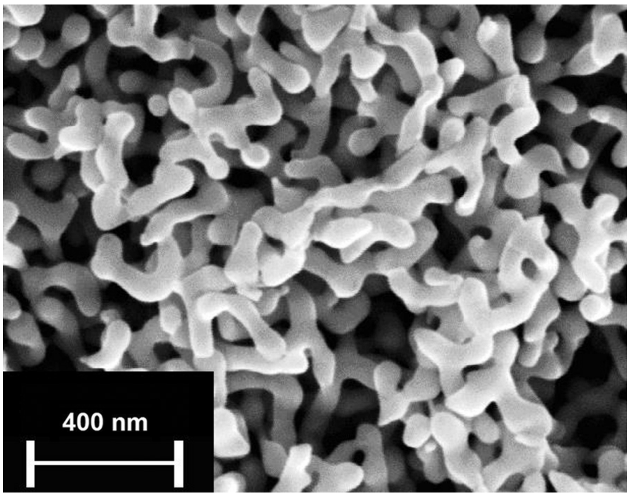

Figure 1.1: Micrograph of a nanoporous gold structure created by dealloying. This structure has ligament size of 63 ± 6 nm and solid fraction of 0.26 ± 0.01. Note the disordered network of ligaments. Reprinted from N. Huber *et al*. Acta Materialia 67 (2014): 252-265, with permission from Elsevier.

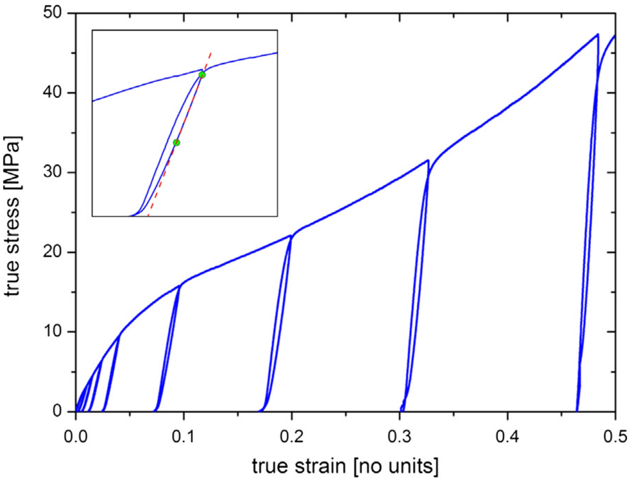

Figure 1.2: Typical stress strain curve of mm-sized nanoporous gold samples. This Figure depicts the experimental stress-strain curve (interspersed with unload segments) of the sample shown in Figure 1.1. The inset illustrates the calculation of the effective elastic moduli (as tangent moduli [23]) from the unload segments. Reprinted from N. Huber *et al.* Acta Materialia 67 (2014): 252-265, with permission from Elsevier.

strains without breaking [15, 16]. The material usually exhibits negligible lateral expansion [15, 19], indicating that the deformation is accompanied by massive densification. The corresponding deformation curve (e.g. Figure 1.2) often features an extended elastic-plastic transition with ill-defined strength followed by pronounced strain hardening [15, 20]. The typical high yield strength of nanoscale wires when considered individually [21, 22], therefore, is not reproduced when they are assembled together in bulk NPG.

Several experimental and simulation studies [24–28] reported the elastic moduli of NPG in the range of $2-3$ GPa. Yet, recent studies [20, 29–31], especially compression tests of mm-sized samples [20, 31], reveal its exceedingly high initial compliance followed by significant stiffening under load [20, 29–31]. That unique elastic behavior is usually demonstrated in terms of the failure of Gibson-Ashby scaling equation [32, 33] in predicting the effective elastic modulus of NPG: The prediction of the scaling law is often more than one order of magnitude stiffer than the experimental value. Since this scaling law has been successfully applied to metal foams [33], its failure when applying to NPG advertises the exotic nature of the elasticity of NPG.

Many attempts have been made to attribute these observations to processes at the atomistic scale as well as topological descriptors at the macroscopic network level. Based on their experimental data, Jin *et al.* [15, 16] promoted lattice defects and their interaction as carrier of plasticity and strain hardening. This suggestion thus contradicts the typical strengthening via dislocation-starvation mechanisms due to limited sources in nanowires [21, 22]. Later works based on Finite Element Method (FEM) simulations of an idealized NPG model supported the dislocation-based mechanisms by pointing out that, apart from topological disorders, the low strength and the subsequent hardening behavior of NPG observed in experiments can only be reproduced if a very high local work hardening is implemented in the constitutive law of the individual ligaments [20, 34]. The analysis therein also connected the topological disorders, specifically nodal shift, to other mechanical properties of NPG, such as small lateral expansion and high compliance. These modeling studies, however, did not succeed in recover the quasi-immediate yielding and deformation-induced stiffening of NPG.

Ligament connectivity is another topological feature that has been emerging in recent discussions of the relation between mechanical properties of NPG and its ligament network [35–39]. Mameka et al. [35] and Jin et al. [36], independently, pointed out that the low strength and high compliance of NPG can be understood as a consequence of defects in the network topology. One might thus interpret these unusual behaviors of NPG in terms of an effective solid fraction that takes into account the contribution of disconnected ligaments [37]. The Gibson-Ashby scaling equations therefore remain their validity if modifications are made to accommodate measures of network connectivity [38]. Yet, these modifications are questionable, as is undoubtedly demonstrated in the work of Hu et al. [39]. There, an almost identical numerical value in the connectivity density of two NPG systems coexisted with hugely different elastic moduli.

While the reference works in Refs. [35–39] root the origin of the high compliance of NPG in the network-level mechanisms, one issue stands out: Elasticity of nanowires is strongly size-dependent (see, e.g. [40] and the references therein). It is therefore to expect that surface-related phenomena also bear their influences on the elastic behavior of NPG. Yet, thus far, a conclusive evidence for the influences of surface effects on the elastic behavior of NPG has not been presented.

Following the ongoing discussion that we summarized above, this work presents our effort to address the mechanical properties of NPG using atomistic simulations.

In Chapter 2, we review the most crucial information concerning simulation methods, as well as techniques used in analyzing simulation data.

The mechanical behavior of a NPG structure created via mimicking spinodal decomposition will be investigated in Chapter 3. There, we will see that the special features of the behavior of NPG can be excellently reproduced by molecular dynamics simulations. Then we will go further to assess the atomistic mechanisms that give rise to the early yielding and subsequent strengthening of NPG.

In Chapter 4, we will depart from the atomistic processes to join the discussion of the influence of topological disorder on the mechanical responses of NPG. A diamond-lattice NPG structure and its disordered counterparts will be examined to test their viability in representing the complex network of NPG.

A study of the influence of network connectivity on the behavior of NPG will be presented in the greater part of Chapter 5. For that purpose, the mechanics of samples created via mimicking spinodal decomposition by different methods will be investigated. Afterwards, we exit the discussion of network topology and assess the influence of surface-related phenomena on the behavior of NPG.

Finally, main findings of this work and an outlook for future studies will be laid out in Chapter 6.

2

METHODS

2.1 SAMPLE PREPARATION

In previous MD studies [27, 28, 41, 42], virtual NPG structures were created via simulating spinodal decomposition with phase field modeling. The structures therein exhibit visually similar topology as compared to that of experimental NPG. Following this approach, we also created virtual NPG samples via mimicking spinodal decomposition, though, by different methods: On-lattice Monte Carlo (MC) simulation [43] and superposition of composition waves [44].

2.1.1 *Monte Carlo simulation*

In the MC simulation, an FCC lattice is created and mapped onto a simulation box of $\langle 100 \rangle$ edges. All the lattice sites are then randomly assigned to one of the two atom types A or B. The temperature T is set to 500 K. Periodic boundary conditions are applied in all three dimensions. We assume an Ising-type interaction between atoms [43]. Only pair interactions between nearest neighbor atoms are allowed: While the energy of a pair of two A atoms or two B atoms is zero, the energy of a pair of an A atom and a B atom is $\epsilon_{AB} = 0.5$ eV. Hence, for a site i, the associated energy is:

$$\mathcal{H}_i = \frac{1}{2} \sum_j \delta_{ij} \tag{2.1}$$

In Equation 2.1, the sum is taken over all nearest neighbor sites of site i. δ_{ij} is equal to ϵ_{AB} if sites i and j are of a same type, 0 otherwise. There is a factor of $1/2$ because the energy δ_{ij} is divided between two bonded atoms. A sketch illustrated the Ising model is given in Figure 2.1.

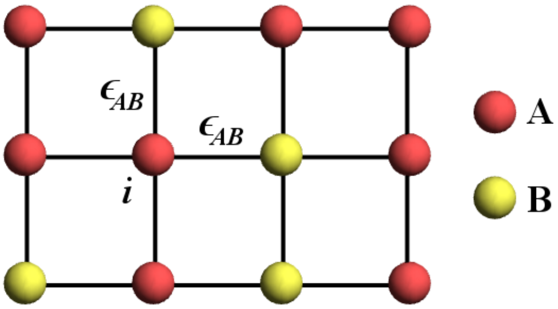

Figure 2.1: Two-dimensional square-lattice Ising model. Pair interaction is ϵ_{AB} between A and B, 0 otherwise. Site i has 2 neighbors of type A and 2 neighbors of type B. The energy associated with i is thus ϵ_{AB}. Since this configuration has 10 A–B bonds, its energy is $10\epsilon_{AB}$.

For the whole system, the Ising-type Hamiltonian representing its energy is the sum of $\mathcal{H}_i$ over all sites:

$$\mathcal{H} = \sum_i \mathcal{H}_i = N_{AB}\epsilon_{AB}, \tag{2.2}$$

with N_{AB} the number of A-B pairs.

Given a particular configuration $\mathbf{s}_\mathrm{c}$ of the system, a new configuration $\mathbf{s}_\mathrm{n}$ is obtained via swapping nearest neighbor sites. The probability for a transition from $\mathbf{s}_\mathrm{c}$ to $\mathbf{s}_\mathrm{n}$ follows the Metropolis algorithm [45]:

$$\mathbb{P}(\mathbf{s}_\mathrm{c} \to \mathbf{s}_\mathrm{n}) = \begin{cases} \exp\left(\dfrac{-\Delta E}{k_\mathrm{B}T}\right) & \text{if} \quad \Delta E > 0 \\ 1 & \text{if} \quad \Delta E \leq 0 \end{cases} \tag{2.3}$$

where ΔE is the change in the energy and k_B is the Boltzmann constant. The phase separation is thus evolved as the system goes through a series of configurations $\mathbf{s}_1 \to \mathbf{s}_2 \to \mathbf{s}_3 \to \cdots$ till the end of the simulation procedure. As a result, the initial random system becomes a structure that consists of two intertwining interconnected networks. Each network is made of one type of atom. After removing one of the two atom types, we get an interconnected network that resembles the microstructure of real NPG structures created by dealloying.

Figure 2.2 depicts an illustration of an NPG sample created by MC simulation. The initial binary mixture of A and B atoms is shown in Figure 2.2a, with the fraction of 0.32 of A atoms. The final configuration of the mixture after the phase separation is shown in Figure 2.2b. Removing B-component of this structure results in an interconnected network of A atoms, as is shown in Figure 2.2c.

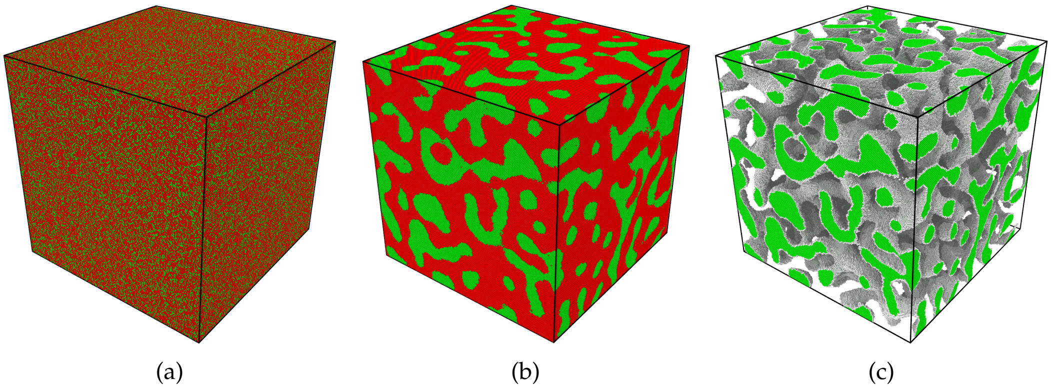

Figure 2.2: Example of NPG sample created via mimicking spinodal decomposition by Monte Carlo simulation. (a) Initial binary mixture with 32% of A atoms (green) and 68% B of atoms (red). (b) Phase separation lead to a structure that consists of two intertwined networks of A atoms and B atoms. (c) A porous structure with solid fraction of 0.32 was obtained after removing all B atoms. For brevity, surface and bulk atoms in (c) are coded in different colors.

2.1.2 *Superposition of composition waves*

Another way to generate NPG structures via spinodal decomposition is to implement the description of phase separation developed by J. W. Cahn in Ref. [44]. According to this theory, the composition of an inhomogeneous solution with average composition c_0 is perturbed by composition waves:

$$c(\mathbf{r}) = c_0 + \sum_{\text{all } \boldsymbol{\beta}} \exp(R(\beta)t) \Big(A(\boldsymbol{\beta}) \cos(\boldsymbol{\beta} \cdot \mathbf{r}) + B(\boldsymbol{\beta}) \sin(\boldsymbol{\beta} \cdot \mathbf{r}) \Big). \tag{2.4}$$

Here, $\mathbf{r}$ denotes the position vector. The sum is taken over all composition waves, with fixed wave number β. While $A(\boldsymbol{\beta})$ and $B(\boldsymbol{\beta})$ are evaluated from the initial fluctuations, the amplification factor $R(\beta)$ in the temporal term $\exp(R(\beta)t)$ determines the growth of fluctuations. Thus, the composition is a superposition of sinusoidal waves with fixed wavelength and random orientation, phase, and amplitude. Note that the simulations in Ref. [44] showed that if a threshold is imposed on the composition c, one obtains an connected structure (see, e.g., Figure 3 in that reference).

In practice, to create NPG structures via implementation of Equation 2.4, we make and impose some conditions. The average composition c is assumed to be $1/2$. No growth of fluctuations is considered. Moreover, the amplitudes of concentration waves are constant. Thus, we can rewrite Equation 2.4 as:

$$c(\mathbf{r}) = \frac{1}{2} + s \sum_{\text{all } \boldsymbol{\beta}} \cos(\boldsymbol{\beta} \cdot \mathbf{r} + \phi(\boldsymbol{\beta})). \tag{2.5}$$

Here, s is an arbitrary scaling factor and $\phi(\boldsymbol{\beta})$ is the random phase. Now, we are left with choosing $\boldsymbol{\beta}$. For that purpose, we use Cartesian coordinates:

$$\boldsymbol{\beta} = \beta_1 \mathbf{e}_1 + \beta_2 \mathbf{e}_2 + \beta_3 \mathbf{e}_3, \tag{2.6}$$

where $\{\mathbf{e}_1, \mathbf{e}_2, \mathbf{e}_3\}$ is the orthogonal basis. Since only one wavelength is allowed, we have:

$$\beta_1^2 + \beta_2^2 + \beta_3^2 = \text{constant}. \tag{2.7}$$

Moreover, we are interested in NPG structures which are periodic with spatial period L_s. That means, for arbitrary integers q_1, q_2, and q_3, we have:

$$c(\mathbf{r} + L_\text{s}(q_1 \mathbf{e}_1 + q_2 \mathbf{e}_2 + q_3 \mathbf{e}_3)) = c(\mathbf{r}). \tag{2.8}$$

From the expression of $c(\mathbf{r})$ in Equation 2.5, this obviously means

$$L_\text{s}(\beta_1 q_1 + \beta_2 q_2 + \beta_3 q_3) = 2\pi m, \tag{2.9}$$

for some integer m. Since Equation 2.9 holds true for arbitrary integers q_1, q_2, and q_3, we must have:

$$\beta_1 = 2\pi \frac{h}{L_\text{s}}, \qquad \beta_2 = 2\pi \frac{k}{L_\text{s}}, \qquad \beta_3 = 2\pi \frac{l}{L_\text{s}}, \tag{2.10}$$

for some integers h, k, and l. Because of the condition in Equation 2.7, h, k, and l must satisfy

$$h^2 + k^2 + l^2 = H, \tag{2.11}$$

where H is an integer constant.

Equations 2.10-2.11 provide the recipe for selecting those $\boldsymbol{\beta}$ vectors. In our implementation, a uniform distribution is used to generate $\phi(\boldsymbol{\beta})$. Note that Equation 2.11 will limit the number of eligible wave vectors, N_{ev}. An illustration of the wave method is shown in Figure 2.3a-b. Figure 2.3a shows the solution with composition color-coded. This composition is a result of a superposition of 48 composition waves. Upon imposing a threshold on the composition, we got a porous network with solid fraction $\varphi = 0.32$. A snapshot of this porous structure is shown in Figure 2.3b. We find that if H leads to small number of wave vectors (say, $N_{\mathrm{ev}} < 30$), the resulting structure is textured and thus not suitable to represent the random network of NPG. Figure 2.3c gives an example of a textured structure created with 6 waves.

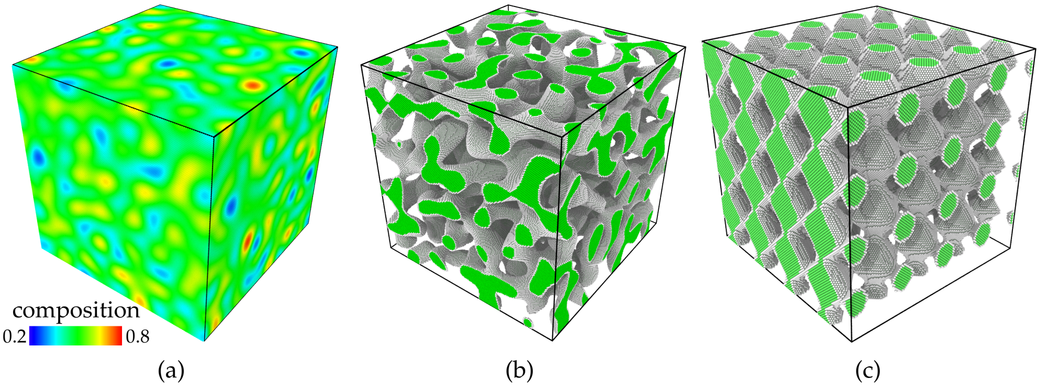

Figure 2.3: Example of NPG sample created via superposition of composition waves. Figure (a) shows the color-coded composition. This composition was generated from 48 waves. (b) After imposing a threshold on the composition, we obtained a nanoporous structure with solid fraction of 32%. Figure (c) shows an example of a textured structure obtained from only 6 composition waves.

In Chapter 5, we will see that the ligament network in the NPG samples created by the wave method has higher connectivity* than that of the samples created by the MC simulation at the same solid fraction. Besides, close-ups (Figure 2.4) at the surface of the wave samples also reveal a smoother surface of the wave samples. Although surface roughness might have influence on the mechanical behavior of nano-scale objects (see, e.g., [46–48]), its influence on the behavior of NPG will not be assessed in the present study.

---

*A measure of the network connectivity will be presented at the end of this Chapter.

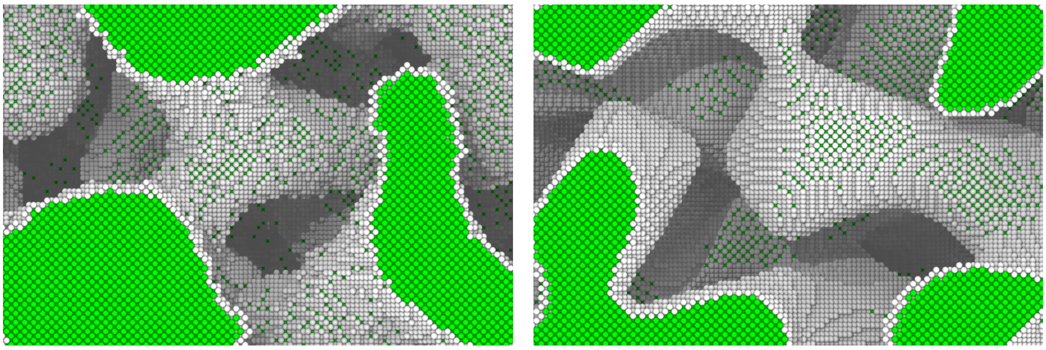

Figure 2.4: Close-ups of the surface of samples shown in Figure 2.2c (left) and Figure 2.3b (right) reveal different surface roughness. Sample created by superposition of composition waves exhibits smoother surface.

2.2 MOLECULAR DYNAMICS

MD gives a framework to study the dynamics of an ensemble of atoms via solving the equations of motion through numerical integration.

We first consider the dynamics of a system of N atoms that is isolated from surrounding. For each atom, let m_i, $\mathbf{r}_i$, and $\mathbf{p}_i$ $(i = 1 \ldots N)$ denote its mass, position vector, and momentum, respectively. The equation of motions of the system read:

$$\frac{\mathrm{d}\mathbf{r}_i}{\mathrm{d}t} = \frac{\mathbf{p}_i}{m_i}, \tag{2.12}$$

$$\frac{\mathrm{d}\mathbf{p}_i}{\mathrm{d}t} = \mathbf{F}_i, \tag{2.13}$$

in which $\mathbf{F}_i$ $(i = 1 \ldots N)$ are forces acting on the atoms

$$\mathbf{F}_i = -\nabla_i \mathcal{U}(\mathbf{r}_1, \mathbf{r}_2, \ldots, \mathbf{r}_N), \qquad i = 1 \ldots N. \tag{2.14}$$

Here, $\mathcal{U}(\mathbf{r}_1, \mathbf{r}_2, \ldots, \mathbf{r}_N)$ is the potential energy of the system and $\nabla_i = \partial/\partial\mathbf{r}_i$ is the gradient operator. If the initial conditions $\mathbf{r}_1(0), \ldots, \mathbf{r}_N(0)$ and $\dot{\mathbf{r}}_1(0), \ldots, \dot{\mathbf{r}}_N(0)$ are given, we can integrate Equations 2.12-2.13 to obtain the trajectories of the atoms. In implementation, the numerical integration can be done via several algorithms of which the Verlet algorithm is the most popular scheme:

$$\mathbf{r}_i(t + \Delta t) \approx 2\mathbf{r}_i(t) - \mathbf{r}_i(t - \Delta t) + \frac{\mathbf{F}_i(t)}{m_i}(\Delta t)^2, \tag{2.15}$$

with Δt the time step.

For the Equations 2.12-2.13, the solution will conserve the total energy Hamiltonian:

$$\mathcal{H}(\mathbf{r},\mathbf{p}) = \sum_{i=1}^{N} \frac{\mathbf{p}_i^2}{2m_i} + \mathcal{U}. \tag{2.16}$$

Note that this conservation law 2.16 only holds if the system is isolated from the surrounding. We now consider situations in which the surrounding acts as heat reservoir (at temperature T) and the system boundary, while keeping the total volume invariant, allows heat exchange. In these circumstances, the equations of motion 2.12 and 2.13 need to be modified to correctly capture the dynamics of the system. An approach for such modifications was first proposed by Nosé [49] and subsequently reformulated by Hoover [50] - thus its name Nosé-Hoover thermostat. There, an additional coordinate ξ, its conjugate momentum p_ξ, and a parameter Q were introduced to represent the surrounding heat reservoir. The corresponding modified equations of motion take the following form:

$$\frac{\mathrm{d}\mathbf{r}_i}{\mathrm{d}t} = \frac{\mathbf{p}_i}{m_i}, \tag{2.17}$$

$$\frac{\mathrm{d}\mathbf{p}_i}{\mathrm{d}t} = \mathbf{F}_i - \frac{p_\xi}{Q}\mathbf{p}_i, \tag{2.18}$$

$$\frac{\mathrm{d}\xi}{\mathrm{d}t} = \frac{p_\xi}{Q}, \tag{2.19}$$

$$\frac{\mathrm{d}p_\xi}{\mathrm{d}t} = \sum_{i=1}^{N} \frac{\mathbf{p}_i^2}{m_i} - N_\mathrm{f} k_\mathrm{B} T, \tag{2.20}$$

where N_f is the number of degrees of freedom of the system*. As is seen in Equation 2.18, the momenta of atoms are modified by a friction term with thermodynamics friction coefficient p_ξ/Q. Equation 2.20 shows that the rate of change of p_ξ is nothing else than the fluctuation in kinetic energy. The Nosé-Hoover thermostat controls this fluctuation to drive the kinetic energy towards the canonical average. During this process, there is a conservation law:

$$\mathcal{H}'(\mathbf{r},\xi,\mathbf{p},p_\xi) = \sum_{i=1}^{N} \frac{\mathbf{p}_i^2}{2m_i} + \frac{p_\xi^2}{2Q} + \mathcal{U} + N_\mathrm{f} k_\mathrm{B} T \xi. \tag{2.21}$$

---

*$N_\mathrm{f} = 3N$ if there are no constraints on the system.

The Nosé-Hoover thermostat mechanism is the precursor for modifications of the equations of motion to capture the dynamics of systems that are exposed to not only constant temperature T but also constant pressure P_{ext} of their surroundings [51–53]. For such a system, its total volume V fluctuates to comply with pressure exerted on the system. Consider, for example, the case of isotropic dilatation of volume, we introduce an additional variable ϵ and its conjugate momentum p_ϵ:

$$\epsilon = \frac{1}{3} \ln\left(\frac{V}{V_0}\right), \tag{2.22}$$

where V_0 is the reference volume. The equations of motion now read [53]:

$$\frac{\mathrm{d}\mathbf{r}_i}{\mathrm{d}t} = \frac{\mathbf{p}_i}{m_i} + \frac{p_\epsilon}{W}\mathbf{r}_i, \tag{2.23}$$

$$\frac{\mathrm{d}\mathbf{p}_i}{\mathrm{d}t} = \mathbf{F}_i - \left(1 + \frac{3}{N_\mathrm{f}}\right)\frac{p_\epsilon}{W}\mathbf{r}_i - \frac{p_\xi}{Q}\mathbf{p}_i, \tag{2.24}$$

$$\frac{\mathrm{d}\epsilon}{\mathrm{d}t} = \frac{p_\epsilon}{W}, \tag{2.25}$$

$$\frac{\mathrm{d}p_\epsilon}{\mathrm{d}t} = 3V(P_{\mathrm{int}} - P_{\mathrm{ext}}) + \frac{3}{N_\mathrm{f}}\sum_{i=1}^{N}\frac{\mathbf{p}_i^2}{m_i} - \frac{p_\xi}{Q}p_\epsilon, \tag{2.26}$$

$$\frac{\mathrm{d}\xi}{\mathrm{d}t} = \frac{p_\xi}{Q}, \tag{2.27}$$

$$\frac{\mathrm{d}p_\xi}{\mathrm{d}t} = \sum_{i=1}^{N}\frac{\mathbf{p}_i^2}{m_i} + \frac{p_\epsilon^2}{W} - (N_\mathrm{f}+1)k_\mathrm{B}T, \tag{2.28}$$

in which W is the mass associated with the barostat and P_{int} is the internal pressure of the system:

$$P_{\mathrm{int}} = \frac{1}{3V}\left(\sum_{i=1}^{N}\frac{\mathbf{p}_i^2}{m_i} + \sum_{i=1}^{N}\mathbf{r}_i \cdot \mathbf{F}_i - 3V\frac{\partial \mathcal{U}}{\partial V}\right). \tag{2.29}$$

For the dynamics described by Equations 2.23–2.28, the following quantity is conserved:

$$\mathcal{H}''(\mathbf{r}, \epsilon, \xi, \mathbf{p}, p_\epsilon, p_\xi) = \sum_{i=1}^{N}\frac{\mathbf{p}_i^2}{2m_i} + \frac{p_\epsilon^2}{2W} + \frac{p_\xi^2}{2Q} + \mathcal{U} + P_{\mathrm{ext}}V + (N_\mathrm{f}+1)k_\mathrm{B}T\xi. \tag{2.30}$$

We emphasize that Equations 2.23–2.28 were developed for the isotropic volume fluctuation. Similar development for the case of full flexibility of volume fluctuations, as well as corresponding adaptation of the Verlet algorithm, can be found in Refs. [51–53].

2.3 INTERATOMIC POTENTIAL

In this work, an embedded-atom method (EAM) potential is used to describe the interaction between gold atoms [54–56]. Within this framework, the total potential energy $\mathcal{U}$ is:

$$\mathcal{U} = \sum_i F(\rho_i) + \frac{1}{2}\sum_{i\neq j}\phi(r_{ij}) \tag{2.31}$$

$$\rho_i = \sum_{j\neq i}\rho_a(r_{ij}). \tag{2.32}$$

In Equations 2.31 and 2.32, r_{ij} is the distance between atoms i and j. $\phi(r_{ij})$ is the short-range pairwise interaction between atoms i and j at a distance r_{ij} apart. For each atom i, ρ_i is the local electron density caused by surrounding atoms whose individual contributions are $\rho_a(r_{ij})$ and $F(\rho_i)$ is the energy needed to embed this atom into the environment with electron density ρ_i. This potential gives following linear elastic properties [56]:

$$\mathrm{C}_{11} = 183\,\mathrm{GPa}, \qquad \mathrm{C}_{12} = 159\,\mathrm{GPa}, \qquad \mathrm{C}_{44} = 45\,\mathrm{GPa}. \tag{2.33}$$

From these elastic constants, we get the Young's modulus, Y^{bulk}, of massive non-textured polycrystaline of gold, using Kröner's formulation [57]:

$$Y^{\mathrm{bulk}} = 78\,\mathrm{GPa}. \tag{2.34}$$

2.4 SIMULATION PROCEDURE

Monte Carlo and MD simulations were carried out with the open-source codes SPPARKS [58] and LAMMPS [59], respectively. Periodic boundary conditions were imposed in all three dimensions.

For each NPG sample, simulation procedure started with an energy minimization using the conjugate gradient algorithm. The minimization was controlled so that at convergence, the relative change in energy and the specified force tolerance were less than 10^{-12} and 10^{-4} eV/Å, respectively. The structure was then thermally relaxed for 1 ns at desired temperature before the onset of straining.

Uniaxial compression test was then simulated by scaling the simulation box length in one dimension at the strain rate of 10^8/s while keeping stress in other dimension at 0 bar. Nosé-Hoover thermostat and barostat with Martyna-Klein-Tuckerman modifications [51–53] (see above) was used to control temperature and pressure.

The time step in all simulations is 2 fs. While most simulations were carried out at $T = 300$ K, for sample studied in Chapter 3, selected runs were done at $T = 0.01$ K to assess conceivable role of thermally activated processes.

2.5 ANALYSIS OF SIMULATION DATA

During the simulation, the instantaneous configuration of NPG samples were exported and analyzed to extract their defect structures, free surface, and connectivity.

2.5.1 *Defect structures*

An atomic pattern matching algorithm [60] based on the adaptive common neighbor analysis (CNA) method [61] was used to detect planar faults, such as stacking faults and twin boundaries. To assign a local crystal structure to an atom via the conventional CNA method [62, 63], one first looks for N bonded nearest neighbor atoms within a cutoff distance, r^c, from the central atom. Then, three numbers are calculated, namely the number of common neighbor atoms which are shared between the central atoms and its bonded atoms, N_{cn}, the number of bonds found in these common neighbors, N_{b}, and the length, i.e. number of bonds, of the longest chain built with these N_{b} bonds, N_{lb}. These numbers form a characteristic signature (N signatures in total, since there are N nearest neighbors) that helps classify the local crystal structure of the central atom (see Table 2.1 for CNA signatures of FCC, HCP, and BCC crystal structures).

	FCC	HCP	BCC
Number of nearest neighbors	12	12	14
Signature	$12 \times (421)$	$6 \times (421)$	$8 \times (666)$
		$6 \times (422)$	$6 \times (444)$

Table 2.1: Common neighbor analysis signatures of FCC, HCP, and BCC crystal structures.

An illustration of the CNA method is given in Figure 2.5. A configuration in which we want to analyze the local crystal structure of the central atom (blue) is shown in Figure 2.5a. Bonds between nearest neighbors found in this configuration (within a predefined cutoff radius) are shown in Figure 2.5b. The central atom has 12 nearest neighbors. Between the central atom and one of its nearest neighbors (e.g. atom coded in red in Figure 2.5c), there are $N_{\mathrm{cn}} = 4$ common neighbors (green). $N_{\mathrm{b}} = 2$ bonds are found in these common neighbors (red), with the maximum length of bond chain, N_{lb}, is 1. From these numbers, the local crystal structure is determined as FCC.

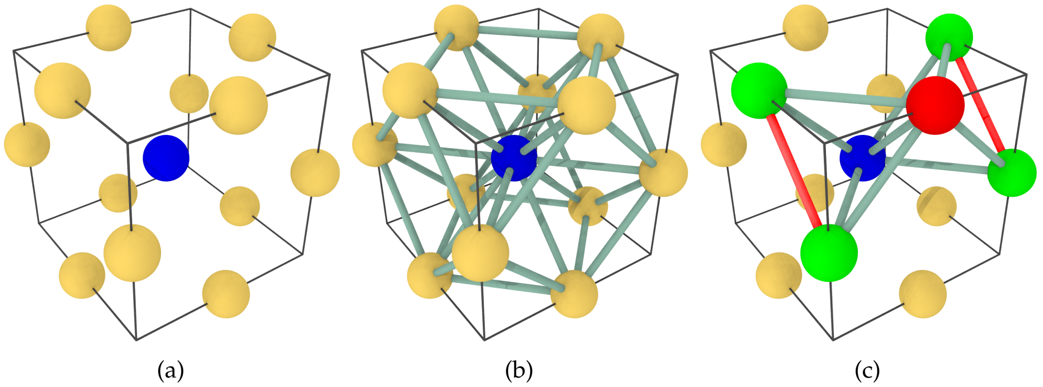
(a) (b) (c)

Figure 2.5: Illustration of the common neighbor analysis (CNA) method. Figure (a) shows a configuration in which we want to analyze the local crystal structure of the central atom (blue). Figure (b) shows bonds between nearest neighbors found in this configuration (within a predefined cutoff radius). The central atom has 12 nearest neighbors. Between the central atom and one of its nearest neighbors (e.g. atom coded in red in Figure (c)), there are $N_{\mathrm{cn}} = 4$ common neighbors (green). $N_{\mathrm{b}} = 2$ bonds are found in these common neighbors (red), with the maximum length of bond chain, N_{lb}, is 1. From these numbers, the local crystal structure is determined as FCC.

The cutoff distance in the conventional CNA is a fixed input parameter [62–64]. In this work, we used a modified version of the CNA method [60] which picks up a local cutoff distance for each atom – thus the name adaptive CNA. Based on the assigned local crystal structures, we can detect atom clusters that are stacking faults or twin boundaries, since the local structure of these atoms is HCP.

Dislocation Extraction Algorithm (DXA) [65, 66] was used to detect and classify lattice dislocations. Given an input structure, the work flow of this algorithm, as is illustrated in Figure 2.6, starts with a Delaunay tessellation whose outputs are triangles for 2D systems and tetrahedra for 3D systems. With the help of the CNA method, the DXA algorithm then classifies the tessellation into good regions and bad regions depending on whether or not they can be mapped to perfect reference crystals. These regions are separated by triangulated interface meshes which enclose all defects in the input crystal. Performing Burgers circuit analysis on the interface meshes will then reveal all dislocations (assorted into Burgers vectors), as well as their densities in the input structure.

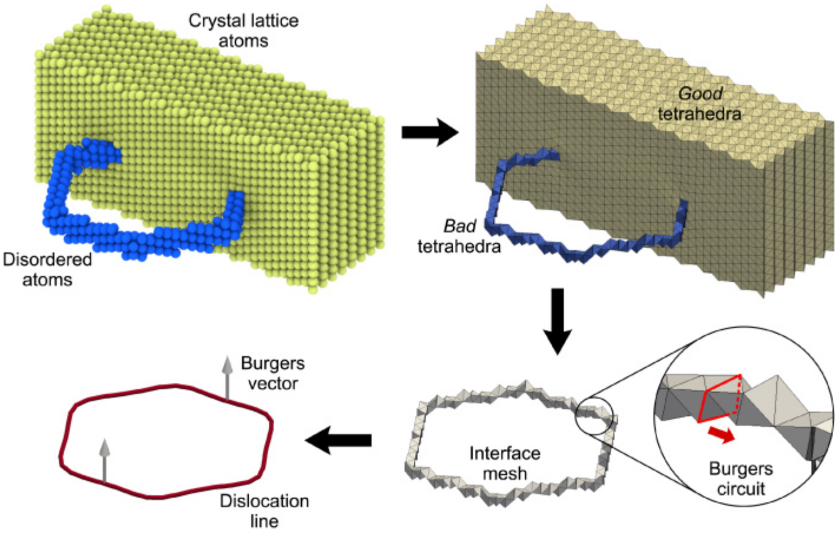

Figure 2.6: Illustration of the work flow of the Dislocation Extraction Algorithm (DXA). The top-left figure shows a BCC single crystal with lattice defects. From the point cloud representing the atoms, a Delaunay tessellation was generated, with constituent tetrahedra classified as 'good' or 'bad' regions (top-right). These regions are separated by a triangulated interface mesh (bottom-right). Performing Burgers circuit analysis on this interface mesh reveals a prismatic dislocation loop, as shown in the bottom-left figure. Reproduced from Stukowski *et al.* Modelling Simul. Mater. Sci. Eng. 20 (2012) 085007 with permission from AIP.

2.5.2 *Surface reconstruction*

For an atomistic structure, its surface is constructed by the alpha-shape method [60, 67]. First, a Delaunay tessellation is generated from the point cloud representing atoms. The tessellation comprises Delaunay tetrahedra that fill the convex hull of the point cloud. For each tetrahedron, if its circumsphere does not fit into a probe sphere with radius R_b, the tetrahedron is considered to be part of the pore space and thus removed. The union of the remaining elements whose radius of the circumsphere does not exceed R_b forms the solid region. Extracting the triangulated surface mesh of this solid region gives us the desired reconstructed surface mesh of the atomistic structure.

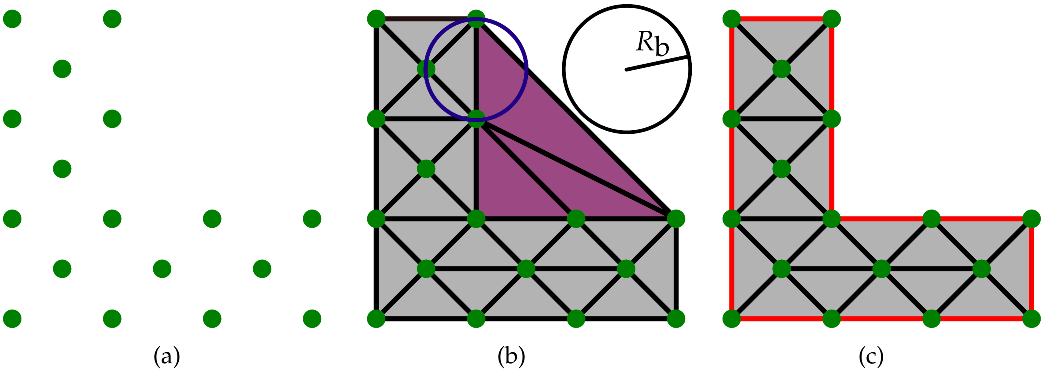

Figure 2.7: Illustration of surface reconstruction via the alpha-shape method (here in 2D). Figure (a) shows a point cloud whose surface is to be constructed. A Delaunay tessellation is generated which comprises triangles that fill the convex hull of the point cloud (Figure (b)). These triangles are marked as 'solid' (grey) if their radius is less than a given probe radius R_b, and open space (magenta) if otherwise. Removing the open space region and extracting the surface mesh of the solid region gives us a reconstructed surface (red) of the point cloud (Figure (c)).

The surface reconstructed by the alpha-shape method depends on the radius R_b [60, 67]. The value of R_b is suggested to be the separation distance between nearest neighbor atoms in the structure [60]. In this work, we choose $R_b = 3$ Å, which is a little bit greater than the separation distance of atoms described by the EAM potential above (2.88 Å).

2.5.3 *Analysis of ligament connectivity*

In Chapter 5, we will study the influence of ligament connectivity on the elastic modulus of NPG samples. For that purpose, we follow Refs. [38, 68, 69] and adopt the "genus", g, as the measure of network connectivity in NPG. In simple words, for an object with a connected and oriented surface, its genus g is the number of handles that it contains. For example, a sphere (Figure 2.8a) has no handle; its genus is thus $g = 0$. A 2-ring torus (Figure 2.8b), has two handles; its genus is therefore $g = 2$. If one of the two rings of the 2–ring torus is broken (Figure 2.8c), there is one handle left; the corresponding genus is thus 1.

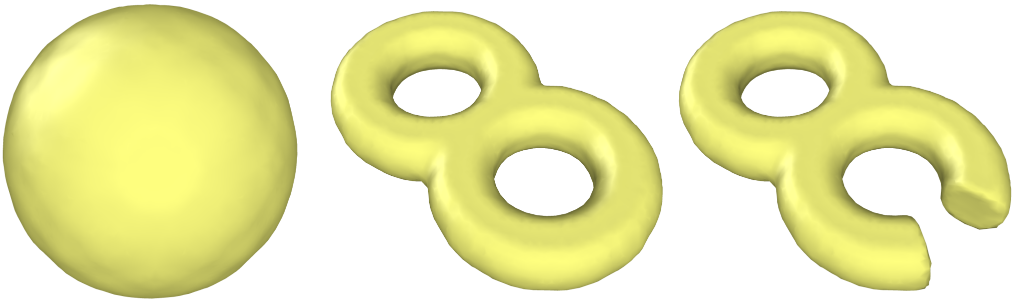

(a) (b) (c)

Figure 2.8: Example of genus of some typical shapes. Genus of a sphere (a) is 0 since it has no handle. A 2-ring torus (b) has two handles and its genus is therefore 2. If one of the two rings of the 2–ring torus is broken (c), there is one handle left; the corresponding genus is thus 1.

Note that if the surface of the object is closed and triangulated, g can be calculated via the Euler characteristic χ:

$$g = 1 - \frac{\chi}{2} \qquad \text{with} \qquad \chi = \#V - \#E + \#F \tag{2.35}$$

where $\#V$, $\#E$, and $\#F$ are the number of vertexes, edges, and faces of the surface. From this equation, once the surface mesh of an NPG structure is reconstructed, the genus of the structure can be immediately calculated, since the alpha-shape reconstruction method results in a triangulated surface mesh (see above).

Since the boundary surfaces of the simulation box cut through many ligaments (see, e.g., Figure 2.2c and Figure 2.3b), a direct analysis on the surface mesh reconstructed from a single representative volume might underestimate the connectivity. To minimize this artifact, the representative volume is replicated in all three dimensions before constructing the surface mesh and performing the topological analysis.

2.5.4 *Visualization*

The open-source software Ovito [70] was used to visualize the simulation results.

3

DEFORMATION OF SPINODAL NANOPOROUS GOLD

In this chapter, we will look into the mechanical behavior of a virtual NPG sample that was created by Monte Carlo simulation. The presentation first serves as a confirmation that simulated computer tests of samples created via mimicking spinodal decomposition can capture the behavior of experimental NPG samples. Based on the simulation data, we will then assess the origin of early yielding and subsequent hardening of NPG.

3.1 INITIAL MICROSTRUCTURE

Figure 3.1a depicts the initial microstructure of the NPG sample that we are going to study in this chapter. This structure was created by mimicking spinodal decomposition via Monte Carlo simulation on a simulation box of 408 Å (100 lattice spacings) in each dimension. Its reconstructed surface is shown in Figure 3.1b. In comparison to the micro-graph of experimental NPG samples (such as the one shown in Figure 1.1), we see that this microstructure resembles the interconnected network of dealloyed NPG well.

The solid fraction φ of the structure showed in Figure 3.1 is 0.297. The alpha-shape surface reconstruction algorithm puts the specific surface area α, i.e. surface area divided by solid volume, of this structure at 1.05/nm. In order to calculate the characteristic ligament size, d, of this sample, we use the conversion rule [71]:

$$d = \frac{1.63(1.25 - \varphi)(1.89 + \varphi(0.505 + \varphi))}{\alpha}. \tag{3.1}$$

This conversion rule is obtained from modeling the network of NPG as a periodic diamond-lattice structure [20] (see Chapter 4 for details of the model). It thus gives a ligament size of 3.15 nm for this virtual NPG sample. That value is one order of magnitude less than the simulation box length ($\sim$ 40 nm). Hence we can rule out the influence of finite-size effects in our simulations.

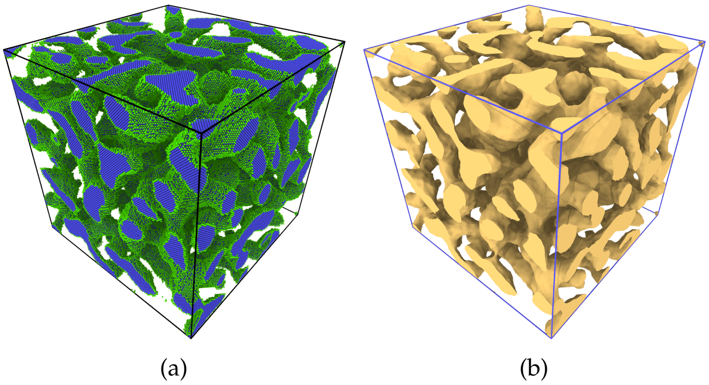
(a) (b)

Figure 3.1: Initial microstructure (a) and reconstructed surface (b) of the NPG studied in this Chapter. This structure was created by mimicking spinodal decomposition via Monte Carlo simulation (see Chapter 2). The sample length is 40.8 nm. Its solid fraction and ligament size are 0.297 and 3.15 nm, respectively.

3.2 RELAXATION BEHAVIOR

The relaxation of the initial porous structure at $T = 0.01$ K and zero external pressure led to a decrease of 2.96% in the total volume. Thus the solid fraction increased to 0.306. Though we did not find any dislocations in the relaxed structure, a very small amount of planar faults was detected: As compared to the system size of ~ 1.2 million atoms, there was a negligible number of 120 atoms in the faulted configurations which corresponds to a density of $\sim 7 \times 10^{-5}$/nm of planar faults. Hence the shrinkage of the sample volume during the relaxation at $T = 0.01$ K is mostly elastic.

There were more structural changes during the thermal relaxation at $T = 300$ K. The solid fraction φ now is 0.308. More importantly, even without any help of the external load during the relaxation, there was a noticeable amount of line and planar defects after this thermal relaxation. The corresponding densities of dislocations, stacking faults, and twin boundaries are $4.8 \times 10^{14}\,\mathrm{m}^{-2}$, $3.2 \times 10^{-3}\,\mathrm{nm}^{-1}$, and $1.4 \times 10^{-3}\,\mathrm{nm}^{-1}$, respectively. Some examples of such defects are shown in Figure 3.9.

We note that the experimental work in Ref. [14] also revealed ensuing volume shrinkage and creation of lattice defects during the synthesis of NPG in fast dealloying; the underlying mechanism was then attributed to the action of surface stress. This was confirmed later in a simulation study [42]. Indeed, irrespective of its size, the boundary surface of a solid exerts forces on the bulk. Those forces are then compensated by the bulk stress with a shear component [72]. When the characteristic size of the solid decreases so that the amount of

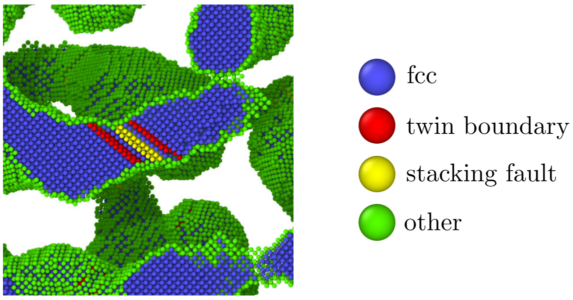

Figure 3.2: Examples of lattice defects in the thermally relaxed (at $T = 300$ K) configuration of the virtual NPG structure shown in Figure 3.1. These pre-existing defects are due to the action of the capillary forces which lead to plasticity even without any help from external load.

surface becomes significant (as in the case of NPG), the shear component in the surface-induced stress becomes pronounced and might thus trigger dislocation nucleation and spontaneous plastic deformation, even without the help of external load. Quantitatively, the surface-induced bulk stress **S** in a solid is calculated via the generalized capillary equation [72]:

$$\int \mathbf{S} \mathrm{d}V = \int \mathbf{s} \mathrm{d}a, \tag{3.2}$$

where V, A, and $\mathbf{s}$ are the solid volume, surface area, and surface stress tensor, respectively. Assuming all the ligaments take the shape of cylindrical wires of diameter d, and approximating the surface stress as isotropic with magnitude f, one gets the principal values of the surface-induced stress in the axial direction, S_A, and radial direction, S_R, as

$$S_\mathrm{A} = -4\frac{f}{d}, \quad S_\mathrm{R} = -2\frac{f}{d}. \tag{3.3}$$

The maximum projected shear stress is found on planes inclined by an angle of $\pi/4$ to the wire axis [73]. Its magnitude τ is:

$$\tau = 2\frac{f}{d}. \tag{3.4}$$

For the EAM potential used in this study, $f \approx 1.1\,\mathrm{J/m^2}$ [74]. With a diameter of $d = 3.15$ nm, the maximum shear stress τ is thus $\tau \approx 0.7$ GPa. It is conceivable that there are many ligaments in the network that have their diameter well below 3.15 nm. Thus, the local surface-induced stresses in these ligaments are well beyond the estimated value 0.70 GPa. Consequently, these ligaments might experience local spontaneous plastic deformation accompanied by creation of the lattice defects.

It might be then argued that if the surface-induced stresses are significant, one should be able to detect the local bulk stress concentration even when no plastic events occur. In fact, a previous simulation study [27] showed that the histogram of the local stress of an NPG structure changed significantly after the relaxation under no external load. To examine this situation in our simulation, the variation of atomistic von Mises stress was kept track during the initial athermal relaxation. Results for a slice cutting through the NPG sample are shown in Figure 3.3. It can be seen that, even though no lattice defects were detected in the athermally relaxed structure, bulk atoms already experienced significant stress concentration. Moreover, the changes are more pronounced when the atoms are near the surface or at the thinner part of ligaments.

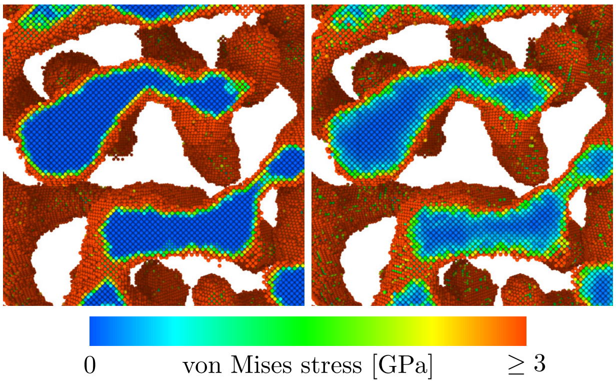

Figure 3.3: Influence of surface stress on local stress distribution. Figure at left and at right show the local von Mises stress of atoms in the NPG sample before and after the initial energy minimization, respectively. While no dislocations were found in the athermally relaxed structure, bulk atoms already experienced significant stress concentration. Changes are more accentuated where atoms are near the surface or at the thinner part of ligaments.

3.3 STRESS-STRAIN BEHAVIOR

Now we examine the behavior of the structure shown in Figure 3.1 in simulated compression tests. The corresponding stress–true strain curves are depicted in Figure 3.4. The behavior at low temperature ($T = 0.01$ K) and at room temperature ($T = 300$K) are shown at left and at right, respectively. While the red curves correspond to the responses of the material under continuous loading, the green curves are for the behavior in load/unload scenarios. We found that the behavior of the virtual NPG sample is practically independent of temperature.

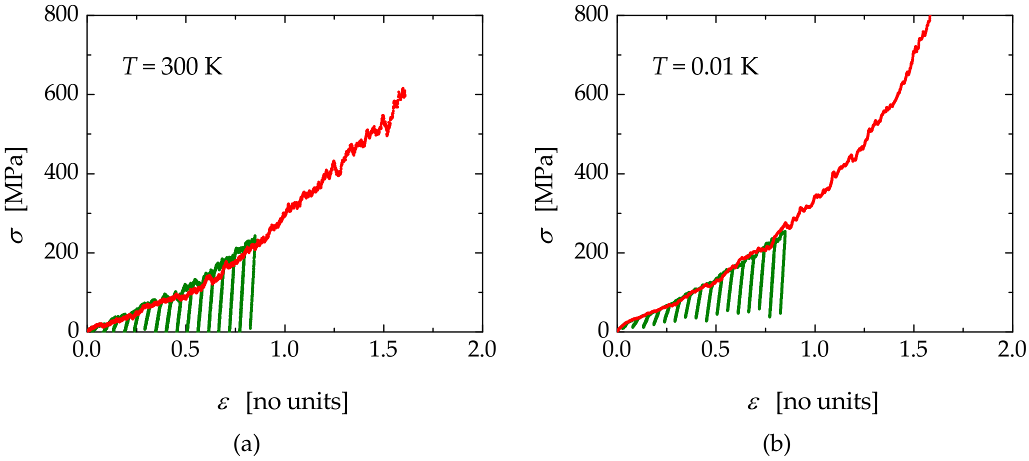

(a) (b)

Figure 3.4: Simulated stress–true strain curves ($\sigma - \varepsilon$) of the virtual NPG sample shown in Figure 3.1 at $T = 300$ K (a) and $T = 0.01$ K (b). Red curves are for continuous uni-axial loading. In blue curves, unload segments were interspersed to monitor the evolution of effective elastic modulus. Note the extended elastic-plastic transition followed by pronounced strain hardening.

As is clearly seen, the virtual NPG started out exceedingly weak: The irreversible unload strains in the small strain regime testify that the material yields to the very least external load. Then the quasi-immediate onset of yielding is followed by an extended elastic-plastic transition and a subsequent pronounced strain hardening. For example in the case of continuous loading, the flow stress at $\varepsilon = 0.1$ is only 18.2 MPa, increases to 93.1 MPa at $\varepsilon = 0.4$, and continues rising to the final value of 591 MPa at the end of the deformation. The simulated behavior of the virtual NPG structure reported here is thus in excellent agreement with experimental results [20, 31, 37] (e.g. the one shown in Figure 1.2): Both data set exhibit a very deformable behavior of NPG in response to the applied load.

3.4 ORIGIN OF THE EARLY YIELDING

While an assessment of the origin of the pronounced hardening observed in the stress strain curve of NPG requires details of microstructural changes and defect structures, we can now address the atomistic mechanisms that lead to the quasi-immediate yielding of the material.

The surface-induced plasticity during the thermal relaxation might have strong influence on the strength of the material. It has been well-established that the mechanical behavior of materials at the nanoscale crucially depends on the preexisting defect structures. Specifically, while dislocation-free whiskers can yield at almost ideal strength, nanoscale pillars containing preexisting dislocations exhibit substantially weaker response [75–77]. Since the thermal relaxation at room temperature led to the creation of lattice defects, it is conceivable that the observed quasi-immediate yielding was fostered by the noticeable initial dislocation density. However, the same weak behavior is also observed at low temperature where no preexisting dislocations were detected. Therefore, the initial dislocation content is not the only reason that causes the immediate yielding.

As the surface-induced pre-stresses are not uniform (see Section 3.3 above), the resolved surface-induced shear pre-stresses are also expected to vary with respect to local ligament thickness and orientation. Hence, during the thermal relaxation, not all but only some ligaments yield under the action of surface stress. These ligaments will thicken and thereby reduce their local pre-stresses. It is then natural to assume that there are ligaments which are pre-stressed to near theoretical strength and thus require only little extra external load to undergo plastic deformation. That is to say, the heterogeneous nature of surface-induced bulk stresses is instrumental in the local yielding events of ligaments and thus effectively in the early yielding of the whole macroscopic ligament network. Furthermore, when the external load increases, more and more ligaments yield, giving rise to the extended elastic-plastic transition.

This line of reasoning is fully supported by our simulations data, as well as reported experimental data from mechanical testing of mm-sized samples [20, 31]. The irreversible strains after unloading in the very small strain regime, while testifying the quasi-immediate yielding, are in accordance with the fact that some ligaments suffer significant surface-induced pre-stress. In the same spirit, the initial increase in the flow stress comes out naturally as a consequence of the depletion of regions with high surface-induced pre-stress: More applied load is needed to yield regions where the influence of pre-stress is less pronounced.

The extended elastic-plastic transition in the stress strain curve of NPG finds its similarity in the deformation curves of massive nanocrystalline metals where deformation events are confined to individual grains with a distribution of crystal orientation and thus a distribution of local Schmid factor [78]. Yet, the stress strain curves of these metals start with a preceding and well-defined elastic regime, which is quite different from the absence of purely elastic deformation of NPG.

To further support our reasoning in favor of surface-induce stress as the significant contributor to the early yielding of NPG in compression, we note that the above picture implies a tension-compression asymmetry: While external compressive load is assisted by the surface-induced stress, tensile load will be counteracted. Thus, the material should exhibit enhanced tensile strength. In order to check the last conjecture, we studied the behavior of an NPG structure whose ligament size and solid fraction after thermal relaxation at $T = 300$ K are 3.76 nm and 0.308, respectively (see Chapter 5 for details). This structure was also created via simulating spinodal decomposition. Figure 3.5 depicts the simulated stress-strain curves of this structure in tension and compression. The asymmetric behavior is clearly demonstrated: The strength (1% offset) in compression is 15 MPa. In tension, the strength is 40 MPa, which is almost 3 times stronger. Similar observation was reported by Farkas *et al.* [27] in their simulation study of NPG. Our present study, along with Ref. [27], thus confirms that the surface-induced bulk stress is responsible for the early yielding in compression but not in tension.

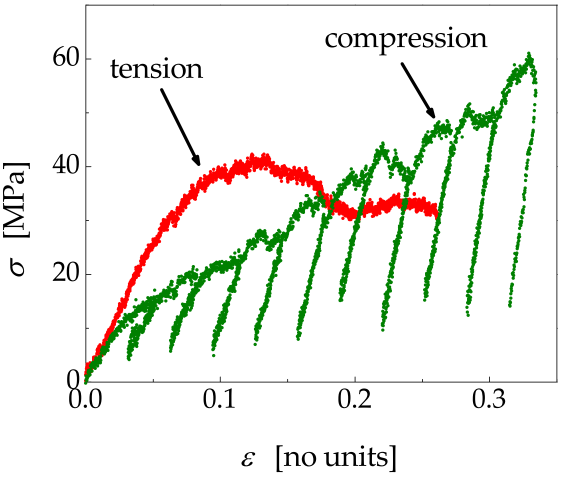

Figure 3.5: Tension-compression asymmetry in behavior of NPG under opposite loading directions. Here shows the stress, σ, versus true strain, ε, of an NPG sample with ligament size of 3.76 nm and solid fraction of 0.302 (see Chapter 5 for details). Tensile strength is 40 MPa, which is almost 3–fold the value of 15 MPa of the strength in compression.

Surface roughness might also contribute to the early yielding of NPG. An examination of the surface of the virtual NPG sample reveals a large amount of step edges and corners (see e.g. Figure3.2). These surface defects are at least geometrically necessary to accommodate the local curvature at the nanoscale. For nanowires, these surface defects lead to local strain concentration, as is experimentally confirmed by imaging with aberration-corrected TEM [79]. As a result, the local stress concentration caused by these surface step edges and corners facilitates dislocation nucleation and therefore reduces the strength of the corresponding nanowires [46, 80, 81]. For NPG, one might expect that these surface defects also cause local stress concentration and thereby contribute to the early yielding of the material - even though the influence must be of minor effect, since the same behavior is also reported for NPG samples with much larger ligament size and smooth surface.

3.5 TRANSVERSE STRAIN AND SURFACE AREA

Figure 3.6 depicts the changes of the true transverse strain of the virtual NPG during the continuous loading. In line with other experimental and simulation studies [15, 19], the lateral dimensions of the NPG sample remained almost invariant even when the axial direction was compressed to half of its initial length (i.e. at true strain $\varepsilon = 0.69$). As a result, the change in the axial direction was directly converted to the decrease in the total volume of the sample. Hence, the NPG structure experienced pronounced increase in solid fraction under compression. At the end of deformation, when 80% of the axial direction had already been reduced, the solid fraction increased to $\varphi = 0.918$ from its initial value $\varphi = 0.308$ before the onset of straining.

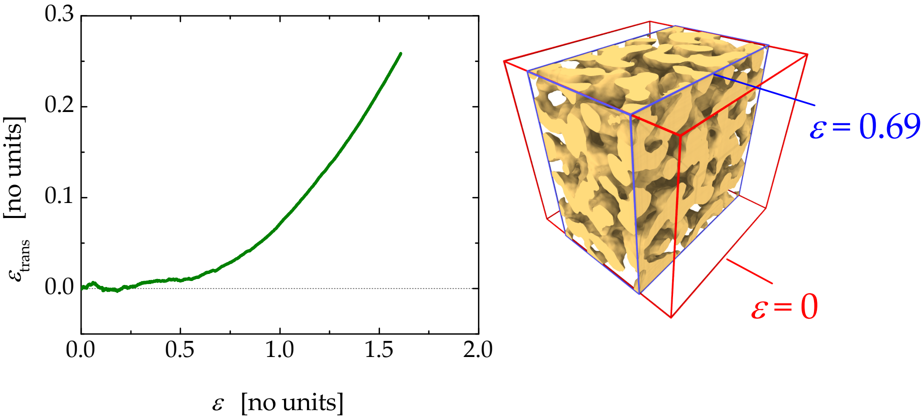

Figure 3.6: True transverse strain, $\varepsilon_{\text{trans}}$, vs. true axial strain, ε, of the NPG sample depicted in Figure 3.1 during the deformation event shown in Figure 3.4a. The transverse strain remains small for a wide range of the axial strain. Figure at right shows the sample (reconstructed surface) at $\varepsilon = 0.69$, along with the simulation box prior to the onset of straining (red frame). Note the negligible changes in the lateral dimensions.

The specific surface area α is another micro-structural factor that was monitored during the deformation. The results (scaled to the initial value α_0 before straining) are shown in Figure 3.7, along with experimental data of dealloyed NPG samples with ligament size of 53 nm and 29 nm, and solid fraction of 0.266

and 0.260, respectively. This plot, while exhibiting good agreement between our simulation data and experimental ones, reveals a continuous loss of free surface. Most of the reduction was found in the later stage of deformation. Conceivably, that loss of surface area is due to the cold coalescence of ligaments: Since compression pushes ligaments towards each other, many of them will come to contact and thus coalesce at surface sites during the deformation. Figure 3.7 gives an illustration of this cold coalescence process. At true strain $\varepsilon = 0.073$, the two ligaments in the red circle are still at a distance apart. Deformation brings these ligaments towards each other and ultimately welds them at the surface, as is illustrated in the close-up of the surface at $\varepsilon = 0.094$.

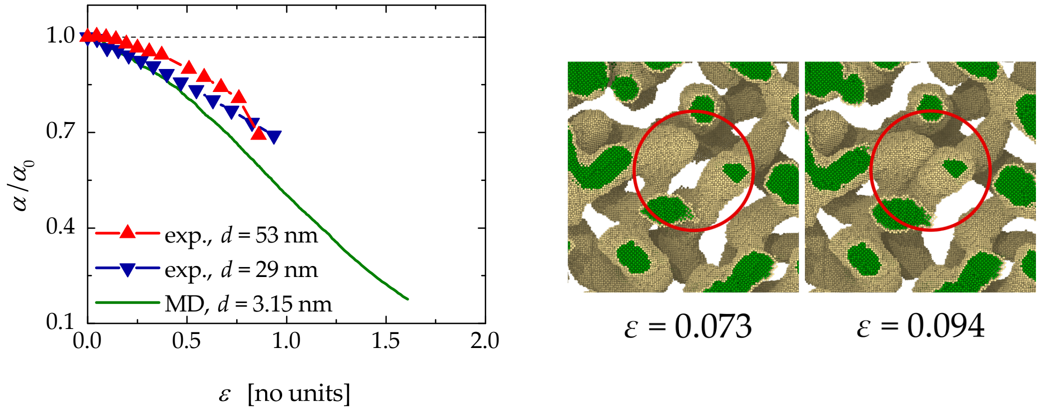

$\varepsilon = 0.073$ $\varepsilon = 0.094$

Figure 3.7: Change of specific surface area, α, of the NPG sample depicted in Figure 3.1 during the deformation event shown in Figure 3.4a. Here, α is scaled to the initial value, α_0, prior to the onset of straining. This graph also shows experimental data of dealloyed NPG samples with ligament size of 53 nm and 29 nm, and solid fraction of 0.266 and 0.260, respectively. Note the loss of surface area of (virtual and experimental) NPG samples. Figures outside the graph illustrate the cold coalescence of ligaments in the virtual NPG sample. At true strain $\varepsilon = 0.073$, two ligaments in the red circle are still at a distance apart. Deformation brings these ligaments towards each other and ultimately welds them at the surface, as is illustrated in the close-up of the surface at $\varepsilon = 0.094$. Experimental data courtesy of Dr. N. Mameka at Helmholtz-Zentrum Geesthacht.

3.6 DEFECT STRUCTURES AND STRAIN HARDENING

Figure 3.8 shows the evolution of defect densities during the continuous loading of the virtual NPG structure. Figures at left and at right correspond to the dislocation density and planar fault density, respectively. It is clear that Shockley partial dislocations were already present in the relaxed structure before any onset of straining. Subsequent loading is then accompanied by a massive accumulation of dislocations. While the density of full dislocations increased continuously, most contribution to the dislocation density at all deformation stages is from Shockley partials. As a result, continuous accumulation of planar fault defects, i.e. stacking faults and twin boundaries, was observed, as is shown in Figure 3.9. It is important to acknowledge that the graphs in Figure 3.8 show that the accumulation of dislocation activities began right after the onset of straining. This is a demonstration of the immediate yielding discussed above.

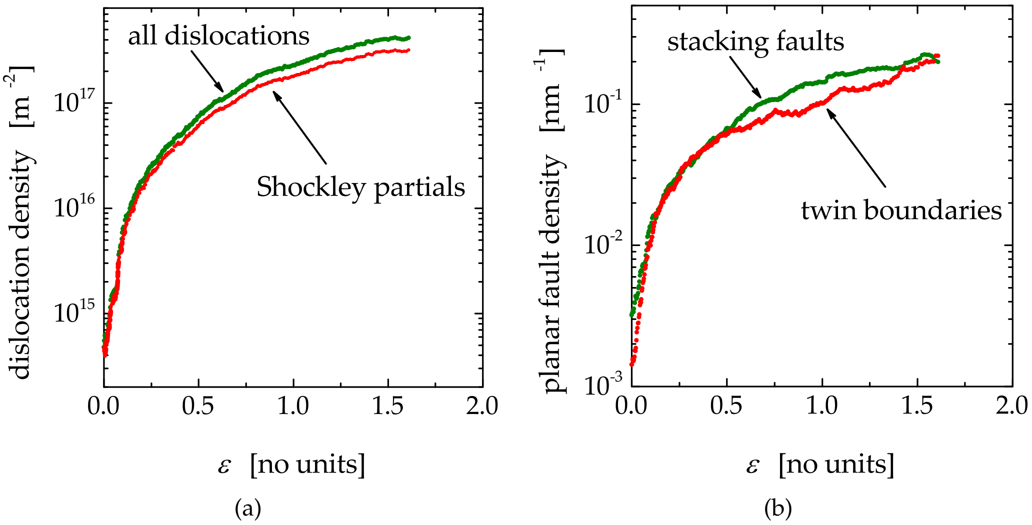

(a)

(b)

Figure 3.8: Evolution of fault density of the NPG sample depicted in Figure 3.1 during the deformation event shown in Figure 3.4a. (a) Accumulation of dislocation density during compression at 300 K. Main contribution comes from Shockley partials. (b) As a result of dislocation activity, twin boundaries and stacking faults populate during compression. Dislocations are already present before the onset of straining, and get their activity immediately upon loading.

Figure 3.9 depicts a typical defect structure of the deformed NPG sample (here at $\varepsilon = 0.8$). In agreement with previous simulation studies [27, 28], many planar defects can be detected. Moreover, grain boundaries and Lomer-Cotrell locks were also found, as is illustrated in the upper and lower magnifications, respectively. While the former conceivably form during the cold coalescence of ligaments (see above), the latter is a direct result of the interaction of dislocations.

Our simulation data thus support an atomistic origin of the hardening behavior of (virtual and experimental) NPG. It is arguable that the deformation-induced changes in microstructure, such as the increase of solid fraction, should be expected to contribute to the hardening of NPG. In fact, suppressing the vol-

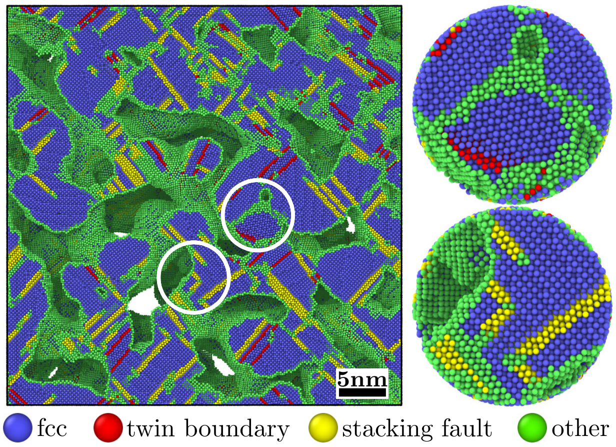

Figure 3.9: Typical defect structures found in the virtual NPG under compression. Left plot shows a slice cutting through sample at the true compressive strain of 0.80. Loading direction is perpendicular to the plot plane. Magnifications of circled regions are shown on the right, depicting examples of grain boundaries (top) and Lomer–Cottrell locks (bottom) found in the deformed structure. Plasticity happens not only at the ligament junctions, but also in the middle of ligaments.

ume change of NPG during compression by infiltrating the pore space with a polymer will eliminate the observed strain hardening [13]. Yet, FEM studies of diamond-lattice NPG structures [20, 34] emphasized that, on top of mere densification effects, Taylor work hardening must be taken into account in the material law for each ligament in order to capture the experimentally observed hardening of NPG. Moreover, electron back scattering diffraction data of the microstructural evolution during continuous compression of NPG [15] revealed a gradual evolution of mosaic spread at a scale much larger than the characteristic ligament size, thus indicating dislocation storage and dislocation interaction within ligaments. In that spirit, the massive accumulation of lattice defects and their interaction in our simulation clearly fall well in line to support and confirm the experimental observation.

For small-scale plasticity, a dislocation-starvation scenario is usually considered as the dominant hardening mechanism [21, 22]. In essence, the basic argumentation for this mechanism is that dislocations in small-scale crystals can easily escape the bulk and annihilate at the surface, leaving behind dislocation-starved materials. Further plastic deformation therefore requires nucleation of new dislocations at high stress. The dislocation densities thus decrease and remain low during the deformation; the strength of the materials meanwhile becomes very high (see, for example, [21, 82]) as compared with the strength of bulk counterparts

The present study, however, shows that the NPG samples are very weak in response to external load. More importantly, the stress-strain curves exhibit pronounced strain hardening carried out by dislocation activities with continuous increase of dislocation densities. The application of dislocation-starvation scenarios to NPG, thus, is not promoted by our simulation data.

The strain rate of MD simulation is much higher compared to that of experiments. When there are competing deformation mechanisms with different strain-rate sensitivity, as in nanocrystalline metals [83–85], the dominant deformation mechanism depends on the strain rate. Specifically, classical MD simulations may overestimate the contributions of dislocation slip [86]. In that respect, we emphasize that our simulation results as well as previous simulation and experimental studies [15, 27, 28] consistently highlight dislocation slip as the only governing process in deformation of NPG. We therefore expect this mechanism to dominate independently of the strain rate, supporting a discussion of simulation and experiment within the same conceptual framework.

3.7 EVOLUTION OF EFFECTIVE YOUNG'S MODULUS

We now turn into the final quantity that was monitored during the deformation: Effective Young's modulus Y^{eff}. The effective modulus of the NPG sample is calculated as the tangent modulus [23] (see Figure 1.1 for an illustration of the calculation) from the unloading segments interspersed in the stress-strain curves. The results at different strain stages are shown in Figure 3.10a. Since the solid fraction φ of NPG increases under compression, we also plotted (Figure 3.10b) the evolution of Y^{eff} (normalized to $Y^{\mathbf{bulk}} = 78$ GPa) versus the square of solid fraction, φ^2, and compared the simulation data with the reference from the relevant Gibson-Ashby scaling law* $Y^{\mathrm{eff}}/Y^{\mathrm{bulk}} = \varphi^2$ [33], along with experimental data from compression test of a dealloyed NPG with ligament size of 40 nm and solid fraction of 0.298 (see Ref. [71] for details)..

The data sets of Figure 3.10 reveal that the (virtual and experimental) NPG samples started out exceedingly compliant at both temperatures. For example, the initial data point of the virtual NPG sample gives an effective modulus $Y^{\mathrm{eff}} = 542$ MPa at room temperature. The corresponding solid fraction is $\varphi = 0.321$. Gibson-Ashby scaling equation predicts an effective modulus of 7.6 GPa, which is fourteen times stiffer than the simulation value. Subsequent deforma-

---

*Note that the Gibson-Ashby scaling law, $Y^{\mathrm{eff}}/Y^{\mathrm{bulk}} = \varphi^2$, was designed for isotropic foam structures with low density. Moreover, φ in the Gibson-Ashby equation denotes the intial density. Nonetheless, it is useful and of interest to use it as referential data.

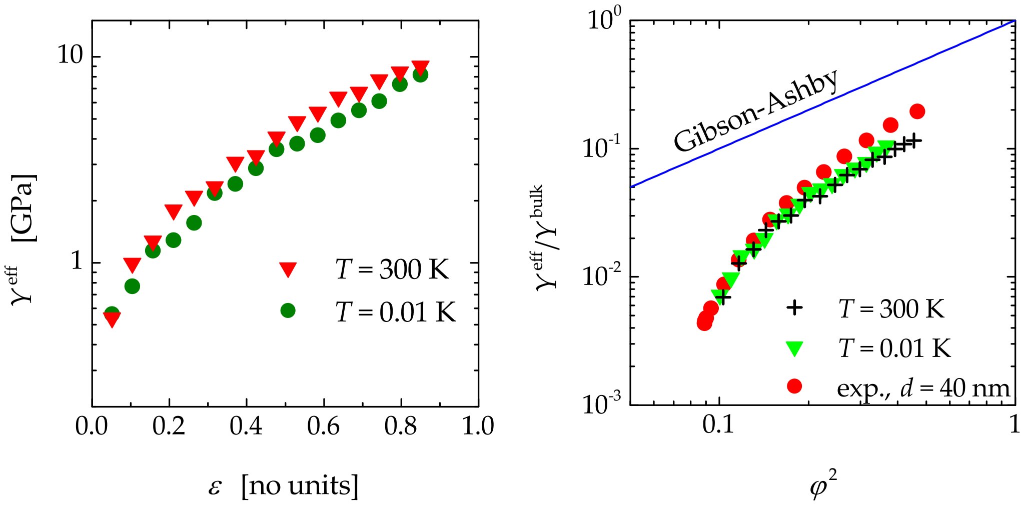

(a) (b)

Figure 3.10: Change of effective Young's modulus, Y^{eff}, of NPG during compression. Figure (a) shows the absolute values of Y^{eff} versus true strain, ε. The scaled values of Y^{eff} (to the Young's modulus Y^{bulk} of massive polycrystalline gold) are shown versus the square of solid fraction, φ, in Figure (b). Gibson–Ashby scaling law is also superimposed in (b), along with experimental data from compression test of a dealloyed NPG with ligament size of 40 nm and solid fraction of 0.298 (see Ref. [71] for details). Note the agreement between simulation and experiment. As is clearly seen in this plot, the evolution of Y^{eff} is characterized by two features: exceptionally high initial compliance and ensuing stiffening under compression. At any time during compression, NPG is much more compliant than the prediction of Gibson–Ashby law. Experimental data courtesy of Dr. N. Mameka at Helmholtz-Zentrum Geesthacht.

tion brought in a substantial stiffening of NPG, leading to the last value of 9.03 GPa at $\varphi = 0.674$, which is about 20–fold stiffer than the value of the initial data point. Despite this deformation–induced stiffening, the virtual NPG sample exhibited a consistently softer behavior as compared to the prediction of the Gibson-Ashby scaling law, as is clearly seen in Figure 3.10b. Remarkably, our simulation data are in excellent agreement when compared with the experimental data shown in Figure 3.10b. They are also in agreement with data from other mechanical tests, such as those from Refs. [19, 20, 31, 37]. The unusually high compliant behavior is thus of intrinsic nature of NPG.

Similar to the quasi-immediate onset of yielding, it is desirable to embark on a discussion of atomistic processes that might give rise to the anomalous compliance of NPG. On the other hand, for a material with complex microstructure, the elasticity of NPG is anticipated to depend very much on its macroscopic, bulk-level factors. Thus, we will now depart from the atomistic regime to investigate the influence on the elastic behavior of NPG of the network topology.

3.8 SUMMARY

In this Chapter, we have presented a study of the mechanical behavior of a virtual NPG sample created by mimicking spinodal decomposition. Requiring no external load, the material already yields to the action of the capillary forces prior to the onset of straining. The simulated compression stress strain curve exhibits quasi-immediate onset of yielding to the smallest applied load, along with exceedingly high initial compliance. Based on our simulation data, we attribute the origin of early yielding to the atomistic processes governed by the surface-induced stress. The origin of the unusually high compliance will be addressed in next Chapters, from both macroscopic standpoint and atomistic framework. As the deformation proceeds, the material becomes stronger and substantially stiffer; though the elastic modulus never approaches the prediction of the relevant Gibson-Ashby scaling equation. Plastic deformation is accompanied by storage of lattice defects and their interaction. Thus, in addition to a mere densification effect, the material strengthens via drastic Taylor hardening. The dislocation-starvation strengthening mechanisms are therefore not supported by our simulation data.

4

DEFORMATION OF DIAMOND-LATTICE STRUCTURES

In the last Chapter, we have studied many aspects of the mechanical responses of a virtual nanoporous gold structure with topology that resembles the topology of experimental structures. So far, the discussion has been focused on underlying atomistic mechanisms that are believed to have strong influences on the behavior of the material, specifically on the early yielding and subsequent strain hardening. In the next two Chapters, we make a detour to assess the role of relevant topological parameters that might impact the behavior of nanoporous gold. Here, we look into the impact of topological disorder.

4.1 DIAMOND-LATTICE STRUCTURE AS A TOPOLOGICAL REPRESENTATION OF NPG

As the Gibson-Ashby scaling laws fail to predict the mechanical behavior of NPG, one might ask: how can we modify or correct these laws so that they reproduce the behavior of NPG? One approach is to tune these semi-empirical laws so that their predictions match experimental data [27, 28, 87]. Another way is to develop new scaling laws based on other models whose topology is suitable to represent the network of NPG [88–91]. These models are then vetted to reveal important parameters which is possibly missing in the Gibson-Ashby laws. Here, we concentrate on a particular model that emerges from the second approach [20, 34]: The diamond-lattice NPG structures.

Based on their examination of the ligament network of experimental NPG samples, Huber et al. [20] observed that the ligament-ligament connections in an NPG network shows similarity with the diamond-lattice structure. They therefore suggested to use regular tetrahedra as building blocks of the ligament network (Figure 4.1a). Consequently, the unit cell which defines structural parameters of the system takes the form of a diamond cubic crystal structure with cylindrical ligaments meeting at spherical nodes (Figure 4.1b). The whole network is thus represented by a diamond-lattice structure (Figure 4.1c). The disordered nature of the NPG network is then captured by randomly displacing the positions of the ligament nodes (Figure 4.1d).

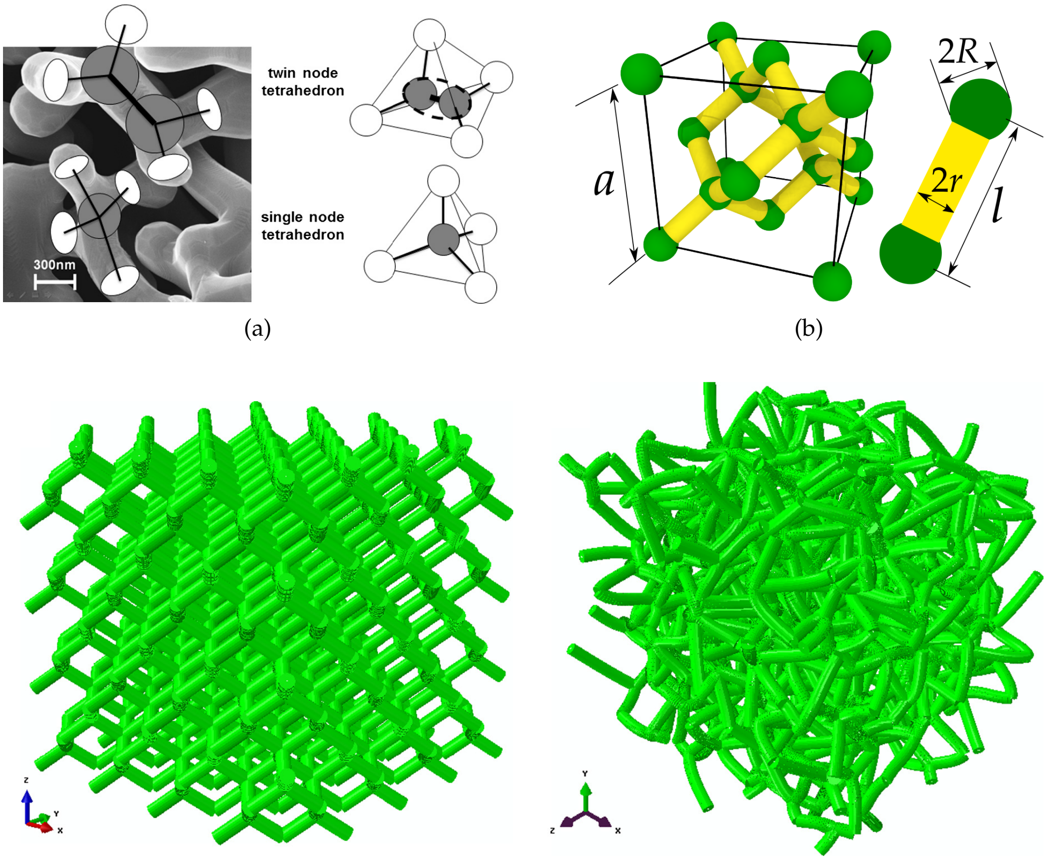

(a) (b)

(c) (d)

Figure 4.1: Diamond-lattice structure as topological representation of NPG. (a) A micrograph of experimental NPG shows typical connections at ligament nodes. These connections can be represented by a tetrahedron with spherical nodes at the center and at the vertexes, and ligaments connecting the center with the vertexes. (b) With tetrahedra as building blocks, the unit cell of the representative volume takes the form of a diamond lattice. In this sketch, a, r, R, and l denote the length of a unit cell, ligament radius, node radius, and node-to-node distance, respectively. (c) An ordered diamond-lattice structure. (d) Displacing the node positions of the ordered structure results in a more realistic disordered structure. Figures (a), (c), and (d) are reprinted from N. Huber et al. Acta Materialia 67 (2014): 252-265, with permission from Elsevier.

The mechanical properties of the diamond-lattice NPG structures (ordered and disordered) were then studied via Finite Element Modeling (FEM) and compared with available experimental and simulation data [20, 34]. As a result, new scaling laws and their generic revision were proposed. Remarkably, these studies revealed that many aspects of the mechanical behavior of NPG can be reproduced by simply tuning the diamond-lattice model. For example, the nearly zero lateral expansion of NPG to very large strains can be reproduced in the diamond model by varying the disorder via monitoring the random displacement of the ligament nodes. The disorder is also responsible for the reduction of the corresponding elastic modulus and yield strength of the diamond-lattice NPG. Moreover, the disorder of the network alone is not enough to account for the pronounced strain hardening in the stress strain curve of NPG; additional work hardening must be included in the material law of each ligament, on top of a mere densification effect.

The results of the FEM analysis in Refs. [20, 34] did not come without drawbacks. While the simulated stress-strain curves show best agreement with experiment for strains between 5% and 15%, the extended elastic-plastic transition of the experiment is not well reproduced. Moreover, though the diamond-lattice models exhibit very compliant behavior, the distinctive initial stiffening usually observed in the experiment did not show up in the simulation.

While the findings in Refs. [20, 34] are promising, especially when considering the possibility to reduce the complex network of NPG to a much simpler system, their drawbacks obviously motivate further study of the viability of these diamond-lattice models to represent the ligament network of NPG. Here, we address this concern via atomistic simulations.

4.2 ATOMISTIC DIAMOND-LATTICE STRUCTURES

For an ordered diamond-lattice NPG structure, geometrical parameters which define its topology are length of a unit cell, a, ligament radius, r, and node radius, R (Figure 4.1b). The node-to-node distance, l, of an ordered structure is thus $l = a\sqrt{3}/4$. To create an ordered diamond-lattice NPG sample, we generated a topology with 4 diamond unit cells. Each unit cell has $\langle 100 \rangle$ edges with length of 38 lattice spacings (i.e. 14.69 nm). Thus, the total length of each direction of the whole topology and the node-to-node distance are 58.75 nm and 6.36 nm, respectively. The ligament radius was set to 2 nm. The node radius was set to $R = r\sqrt{3/2}$ to avoid acute connections [20, 34].

An FCC lattice was created and mapped onto the ordered diamond-lattice topology, resulting in an ordered diamond-lattice NPG sample with solid fraction of $\varphi = 0.302$. Due to the crystallography of the ordered diamond-lattice NPG sample, its ligaments are in $\langle 111 \rangle$ directions. A snapshot of this sample is depicted in Figure 4.2a.

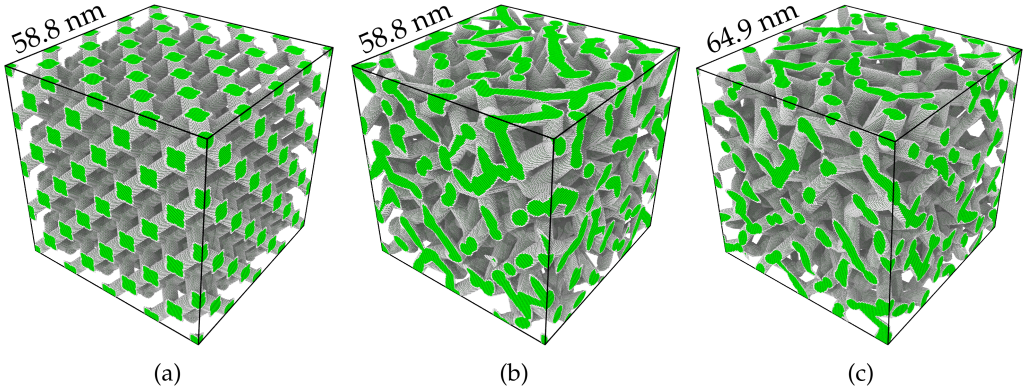

(a) (b) (c)

Figure 4.2: Atomistic ordered and disordered diamond-lattice structures studied in this Chapter. Figure (a) shows the ordered diamond-lattice structure created from 4 unit cell. The as-created solid fraction of this structure is 0.302. Figures (b) and (c) depict disordered diamond-lattice structures with as-created solid fraction of 0.358 and 0.301, respectively. A random factor of 0.23 was used to create both samples shown in (b) and (c).

From the topology of an ordered diamond-lattice structure with the length of a unit cell a, the topology of an disordered diamond-lattice structure is obtained via randomly displacing the node positions. For each node, we denote $d_i\,(i = 1,2,3)$ the displacement in the coordinate direction i, and define the disorder parameter A by the following condition:

$$-A \leq \frac{d_i}{a} \leq +A. \tag{4.1}$$

The suggested value of the disorder parameter is $A = 0.23$ [34]. Using this value of A and a flat distribution, we generated a disordered topology from the ordered topology above (i.e. with 4 unit cells and with $a = 14.69$ nm, $r = 2$ nm, and $R = r\sqrt{3/2}$). Matching this disordered topology with an FCC lattice resulted in a disordered diamond-lattice NPG sample. Since the randomization increases the average ligament length [34], the solid fraction of this disordered diamond-lattice NPG sample effectively increased to 0.358. A snapshot of this structure is shown in Figure 4.2b.

Since it is of interest to compare the behavior of the ordered sample with the behavior of a disordered sample of the same solid fraction, we created a disordered diamond-lattice NPG structure (Figure 4.2c) with 4 unit cells and with $a = 16.22$ nm, $A = 0.23$, $r = 2$ nm, and $R = r\sqrt{3/2}$. The solid fraction of this disordered structure is 0.301.

4.3 RELAXATION BEHAVIOR

There were slight changes in the solid fraction of the diamond-lattice NPG samples during the thermal relaxation under no external load at 300 K (Table 5.1). Though no trace of plasticity was found in the relaxed structure of the perfect diamond model, small amounts of dislocations were found in the disordered diamond structures. Their corresponding dislocation densities are $\sim 3 \times 10^{14}\mathrm{m}^{-2}$, which is about 1.5 times less than the density of preexisting dislocations ($4.8 \times 10^{14}\mathrm{m}^{-2}$) found in the virtual NPG sample studied in Chapter 3.

Sample	L_s [nm]	A	φ_ini	φ_rel	Y^eff [GPa]	σ^y [MPa]
$A^{0}_{0.303}$	58.75	0	0.302	0.303	3.26	142
$A^{0.23}_{0.360}$	58.75	0.23	0.358	0.360	3.21	96
$A^{0.23}_{0.303}$	64.87	0.23	0.301	0.303	2.26	74

Table 4.1: Summary of the mechanical properties of the diamond-lattice structures. L_s, A, φ_ini, φ_rel, Y^eff, and σ^y denote the sample length, nodal shift parameter, initial (as-created) solid fraction, solid fraction after the thermal relaxation at 300 K, initial elastic modulus, and 1% offset strength, respectively.

For brevity, the diamond-lattice structures will be referred to as $A^{0}_{0.303}$, $A^{0.23}_{0.303}$, and $A^{0.23}_{0.360}$ with the superscripts and subscripts denoting the random factor and the relaxed solid fraction of these samples, respectively.

4.4 STRESS STRAIN BEHAVIOR

The stress-strain curves of the diamond-lattice structures in load/unload scenarios are shown in Figure 4.3. For sample $A^{0}_{0.303}$, the curve starts out with a well-defined regime of elasticity before it increases continuously to the maximum stress $\sigma = 185$ MPa at $\varepsilon \approx 0.09$. Then, the deformation curve manifests softening behavior before entering its flow stress regime. Apart from increases of the stress during reloading, the curve exhibits a slightly decreasing trend in this regime. For example, the flow stress is 146 MPa just before the first unload segment. This value decreases to $\sigma = 130$ MPa before the last unload segment.

Elasticity also shows up in the stress strain curves of the disordered samples $A^{0.23}_{0.303}$ and $A^{0.23}_{0.360}$, though the nodal shift smears out the maximum stress observed in the stress-strain curve of the ordered sample $A^{0}_{0.303}$. The elastic-plastic transition region in the deformation curve of the disordered samples is greatly

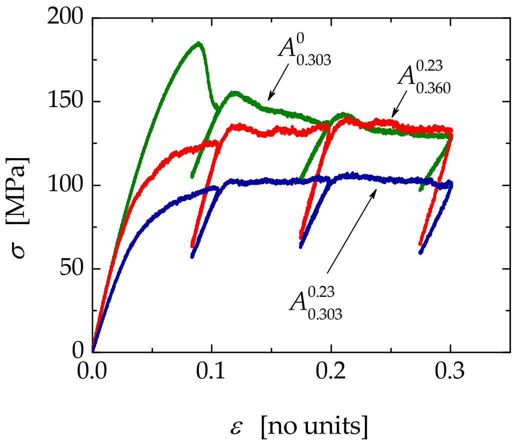

Figure 4.3: Simulated stress-true strain (σ-ε) curves of diamond-lattice structures. Unloading segments were interspersed to monitor the evolution of effective elastic modulus. All curves exhibit elastic regimes before yielding. Note that the elastic regimes of the ordered sample $A^{0}_{0.303}$ and the disordered sample $A^{0.23}_{0.360}$ are visually indistinguishable. These curves were simulated with a strain rate of 10^8/s at 300 K.

broadened. Afterwards, the flow stress of the disordered samples almost follows a plateau at high stress, which is about 130 MPa and 100 MPa for $A^{0.23}_{0.360}$ and $A^{0.23}_{0.303}$, respectively.

It is arguable that the maximum stress in the stress-strain curve of the $A^{0}_{0.303}$ sample is an overshoot in stress due to the very high strain rate of the simulation (10^8/s). However, experimental data on the behavior of macroscopic diamond-lattice foams made of Ti6Al4V ELI [92] reveal the same trend (c.f. Figure 4 in Ref. [92]). The maximum stress is thus not a mere effect of the high strain rate, but rather reflects an intrinsic feature of the deformation curve of highly ordered diamond-lattice foams. Later on in Section 4.5, we will see that this maximum stress actually reflects the high stress due to the deformation mode of the ligaments in the diamond-lattice structure.

4.5 YIELD STRENGTH AND ELASTIC MODULUS

Following suggestion of Ref. [93], the yield strength σ^{y} of the diamond-lattice samples is defined as 1% offset strength. The stress strain data thus give $\sigma^{y} = 142$ MPa for sample $A^{0}_{0.303}$. Using this value, we can calculate the corresponding yield strength of the solid phase σ^{s} with the help of the scaling law for the strength of the ordered diamond-lattice structures (i.e. $A = 0$) [20]:

$$\frac{\sigma^{\mathrm{y}}}{\sigma^{\mathrm{s}}} = c_{\sigma_y}\left(\frac{r}{l}\right)^3\left(1-\sqrt{6}c_R\frac{r}{l}\right)^{-1} \qquad \text{with} \qquad \frac{r}{l} < \frac{1}{\sqrt{6}c_R}. \tag{4.2}$$

In Equation 4.2, $c_{\sigma_y} \approx 1.4$, $rc_R/R = \sqrt{2/3}$, and l is the node-to-node distance. In our case, $c_R = 1$, $\sigma^{\mathrm{y}} = 142$ MPa, $r = 2$ nm and $l = 6.36$ nm for sample $A^{0}_{0.303}$. Equation 4.2 thus puts the yield strength of the solid phase at $\sigma^{\mathrm{s}} = 749$ MPa, which is much greater than the values calculated from the experimental data using the same equation [34]. The reason is possibly because the system is highly ordered and all ligaments are aligned along $\langle 111 \rangle$ directions.

For the disordered samples $A^{0.23}_{0.360}$ and $A^{0.23}_{0.303}$, the values of yield strength are $\sigma^{\mathrm{y}} = 96$ MPa and $\sigma^{\mathrm{y}} = 74$ MPa, respectively. These numbers reveal that although sample $A^{0.23}_{0.360}$ is denser than sample $A^{0}_{0.303}$, it is much weaker. Interestingly, the ratio between the strength of the disordered samples ($96/74 \approx 1.3$) is identical to the ratio of solid fraction raised to the power of 1.5 as in the classical Gibson-Ashby law ($(0.360/0.303)^{3/2} \approx 1.3$). Thus, when it comes to the yield behavior of diamond-lattice NPG, the topological disorder is more relevant than the solid fraction. It is only when the samples posses a similar degree of disorder/order that the solid fraction becomes pertinent.

The initial elastic modulus of the sample $A^{0}_{0.303}$ is $Y^{\mathrm{eff}} = 3.26$ GPa. As is with the yield strength, we compare this value to the prediction of the scaling equation for the perfect diamond-lattice structure [20]:

$$\frac{Y^{\mathrm{eff}}}{Y^{\mathrm{s}}} = c_E\left(\frac{r}{l}\right)^4\left(1+\frac{r}{l}\right)^{-4}\left(1+\frac{r}{l}\right)^2 \qquad \text{with} \qquad c_E = 5.8, \tag{4.3}$$

where Y^{s} is the elastic modulus of the ligaments. Since all ligaments in the ordered sample $A^{0}_{0.303}$ are directed along the $\langle 111 \rangle$ directions, the elastic modulus in that direction must be used as Y^{s} in Equation 4.3 - thus $Y^{\mathrm{s}} = 124$ GPa for the current EAM potential. With $r = 2$ nm and $l = 6.36$ nm, Equation 4.3 predicts an effective modulus of 4.07 GPa, which is 1.25 times stiffer than the value obtained above.

As compared with the ordered structure, introducing the nodal shift without any correction of solid fraction only slightly decreases the effective modulus: $Y^{\mathrm{eff}} = 3.21$ GPa for sample $A^{0.23}_{0.360}$. Indeed, the elastic regimes of samples $A^{0}_{0.303}$ and $A^{0.23}_{0.360}$ are visually indistinguishable, as is shown in Figure 4.3. When the correction of solid fraction is taken into account in sample $A^{0.23}_{0.303}$, the initial elastic modulus is greatly reduced to a much softer value of $Y^{\mathrm{eff}} = 2.26$ GPa.

The comparison between the initial elastic moduli of samples $A^{0}_{0.303}$ and $A^{0.23}_{0.303}$ testifies that the nodal shift makes diamond-lattice structures significantly softer. Yet, since sample $A^{0.23}_{0.360}$ is as stiff as sample $A^{0}_{0.303}$, it is unclear whether or not the nodal shift can take over the solid fraction to dictate the initial elastic behavior. Similarly to the yield strength, the ratio between initial elastic moduli of samples with identical nodal shift follows the classical Gibson-Ashby scaling relation ($3.21/2.26 \approx 1.42$ for the ratio of Y^{eff} as compared to $(0.360/0.303)^2 \approx 1.41$ for the ratio of squared solid fraction).

Figure 4.4 depicts the elastic moduli of the diamond-lattice structures at different strain states. In contrast to significant stiffening under compression of dealloyed NPG, the effective modulus of these structures decreases drastically as the deformation proceeds. For example, the effective modulus of sample $A^{0.23}_{0.303}$ calculated from the last unload segments is only 1.5 GPa, which is a reduction by a factor of 1.5 from its initial modulus of 2.26 GPa.

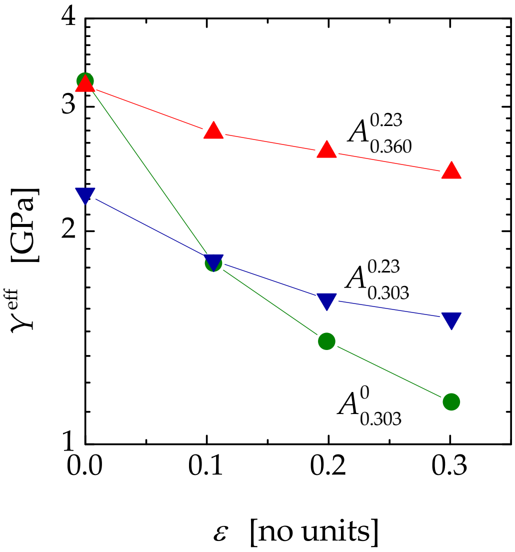

Figure 4.4: Evolution of effective elastic modulus, Y^{eff}, of diamond-lattice structures with stress-strain curves shown in Figure 4.4. ε denotes true strain. All structures show very high initial stiffness. More remarkably, these structures show drastic decrease in the elastic modulus, irrespective of whether or not the nodal shift is introduced. Thus, the stiffening behavior usually observed in experimental NPG samples, as well as in the spinodal decomposition NPG sample reported in Chapter 3, is not reproduced in the diamond-lattice structures.

4.6 LIGAMENT DEFORMATION MODE

The results shown above reveal that, irrespective of the influence of the nodal shift, the stress strain curve of the diamond-lattice model always starts with a well-defined elastic regime. Moreover, yield behavior is always preceded by a high modulus. Nodal shift broadens the elastic-plastic transition regime, lessens the yield strength, and enhances the strain hardening. Yet, the low level of flow stress and, especially, the quasi-immediate yielding of the experimental NPG, as well as the virtual NPG reported in Chapter 3, is never reached.

In terms of deformation mechanisms, the observed initial elasticity and yield behavior of the diamond model can be interpreted as an indication of transition between different deformation modes in many constituent ligaments, namely from stretching to bending.

The diamond-lattice structure belongs to a larger group of periodic lattice-structured materials. Thus, similarly to constituent beams in lattice-structured materials, ligaments in the diamond-lattice structure can be deformed via either bending or stretching [*] [95, 96]. While the former changes the length of a ligament along its axial axis, the latter rotates it about an axis perpendicular to the axial axis. Since the stretching mode requires very high stress as compared to the bending-mode, a bending-dominated structure is soft and weak; a stretching-dominated structure is otherwise strong and stiff [96]. The stress strain curve of a stretching-dominated structure typically exhibits post-yield softening due to plastic buckling or brittle collapse [96] (see, e.g. a schematic sketch of typical stress strain curves of stretching-dominated structures shown in Figure 12 in Ref. [96])

Indeed, the discussion above reveals the high stiffness and strength as well as the post-yield softening of the ordered sample $A^{0}_{0.303}$, thus promoting it as a stretching-dominated structure. In fact, the symmetry of the structure requires all of its ligaments to be deformed by a similar deformation mode. When the nodal shift is introduced, the structure loses its symmetry and many ligaments become slender due to their elongation [34]. Hence, the deformation modes of some ligaments might be switched to bending, leading to the reduction in strength and stiffness of the whole structure. Evidently, the argument is supported by our current data, especially when comparing between samples $A^{0}_{0.303}$ and $A^{0.23}_{0.303}$ where there is no density effect due to nodal shift. Moreover, because the strength and stiffness of disordered samples remain high, most of the ligaments are still deformed by stretching.

---

[*] Recently, Jiao et al. [94] have shown that a ligament in NPG structure can also be *locally* twisted, though the effective deformation of the ligament is still either bending or stretching mode.

Another observation supports our speculation/assumption is the fact that the elastic modulus of the diamond-lattice structures decreases drastically during the deformation, as is documented in Figure 4.4. This loss of modulus can be understood as a natural consequence of plastic buckling at high stress of ligaments that are deformed by stretching.

4.7 MICROSTRUCTURAL CHANGES

One of the key findings of Refs. [20, 34] is that the small lateral expansion of experimental NPG can be captured in the diamond-lattice model by increasing the nodal shift parameter A. Moreover, the optimal value of A is $A \approx 0.23$ [34] with which the elastic Poisson's ratio ν_E of the disordered structures approaches the experimental value of dealloyed NPG ($\nu_E \approx 0.2$ calculated from unload segments of stress strain curves [19]). Our simulation data also support the influence of the nodal shift on the lateral expansion and elastic Poisson's ratio of the diamond-lattice structures. Though, the experimental value of $\nu_e \approx 0.2$ of NPG is never reached.

Figure 4.5 depicts the change in transverse strains of the diamond-lattice structures. It is evident that the lateral expansion of the disordered samples are less than that of the ordered sample. The transverse strain of sample $A^{0}_{0.303}$ at $\varepsilon = 0.30$ is 0.11. For samples $A^{0.23}_{0.303}$ and $A^{0.23}_{0.360}$, the corresponding values are 0.07 and 0.08, respectively. As a comparison, at the same axial strain $\varepsilon = 0.30$, the transverse strain of the spinodal sample studied in the last Chapter is almost zero.

Linear fits in the regime of small strains of the stress-strain curves show that the $\nu_E = 0.42$ for sample $A^{0}_{0.303}$. The nodal shift reduces that value to $\nu_E = 0.35$ in the disordered samples. Thus, the elastic Poisson's ratio of the disordered samples in atomistic simulation is more than 1.7 times greater than the prediction of the FEM analysis for diamond structures of identical nodal shift [34].

The fact that all diamond models show more pronounced lateral expansion than the virtual NPG sample studied in the last chapter means that the deformation-induced change in the solid fraction will be less significant or even negligible. Indeed, the ratio of solid fraction $\varphi/\varphi_{\text{relaxed}}$ at $\varepsilon = 0.30$ is 1.08 for sample $A^{0}_{0.303}$. For samples $A^{0.23}_{0.303}$ and $A^{0.23}_{0.360}$, the respective ratios are 1.15 and 1.17, respectively. At that same strain, that ratio of the virtual NPG sample studied in the last Chapter is 1.34.

The change of specific surface area (scaled to the corresponding value before the onset of straining), α/α_0, during compression of the diamond-like samples is shown in Figure 4.6. As is demonstrated, after very small decreases for strains less than about 10%, the ratio α/α_0 of sample $A^{0}_{0.303}$ slightly increases. Though, even at the maximum increase by the end of the deformation, that ratio is only

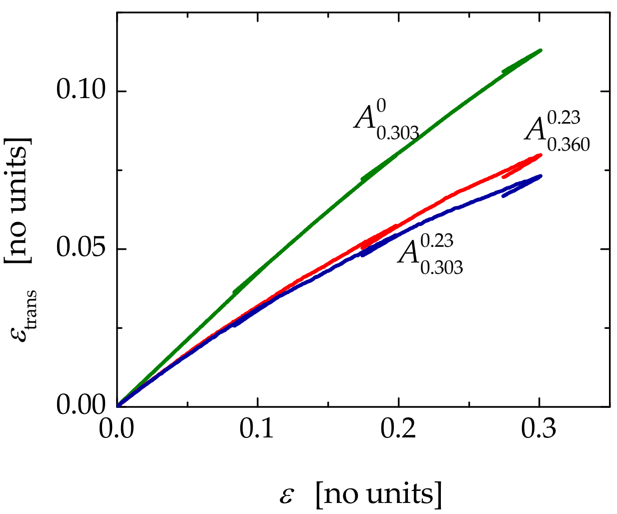

Figure 4.5: True transverse strain, $\varepsilon_{\mathrm{trans}}$, vs. true axial strain, ε, of the diamond-lattice structures during the deformation event shown in Figure 4.3. Short line segments in this plot are from the unload segments during the simulated compression tests. This plot shows that the nodal shift has strong influence on the evolution of $\varepsilon_{\mathrm{trans}}$, though the small lateral expansion observed in experimental NPG is never reproduced.

about 1.01. For the disordered samples, the specific surface area continuously decreases during the compression. Though the change is minor (at most less than about 4%), we can say that the nodal shift has strong impact on the evolution of α.

4.8 DISLOCATION DENSITY

The evolution of dislocation density of the diamond-lattice structures is shown in Figure 4.7. It can be seen that while the initial dislocation density of sample $A^{0}_{0.303}$ is zero, the corresponding values for the disordered samples are non-zero, thus confirming the observation of dislocations in these samples during the initial thermal relation.

No dislocations were detected in the ordered sample $A^{0}_{0.303}$ until $\varepsilon \approx 5\%$. From there to $\varepsilon \approx 0.09$, their density increases slightly. Afterwards, more and more dislocations are nucleated and multiplied, thus leading to the continuous accumulation of dislocation density. We note that $\varepsilon \approx 0.09$ is about the strain at which the stress strain curve of sample $A^{0}_{0.303}$ attains its maximum and starts entering its softening regime. The observation therefore supports our previous assumption on ligament deformation modes.

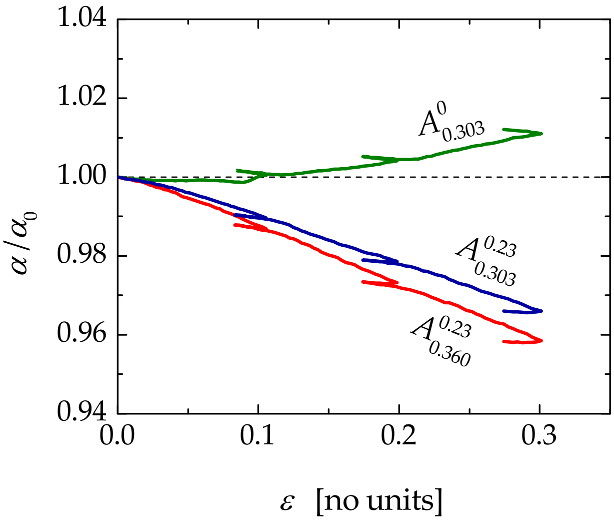

Figure 4.6: Change of specific surface area, α, of the diamond-lattice NPG samples during the deformation event shown in Figure 4.3. Here, α is scaled to the initial value, α_0, prior to the onset of straining. Short line segments in this plot are from the unload segments during the simulated compression tests. For the ordered sample, α decreases in the elastic regime and increases in the plastic regime. Introducing the nodal shift inverts the behavior of α completely: Both disordered samples show decreasing α during the deformation process.

For the disordered samples $A^{0.23}_{0.303}$ and $A^{0.23}_{0.360}$, their dislocation density stays almost constant for strains up to $\varepsilon \approx 0.01$. Then, their dislocation density keeps increasing until the end of deformation. Note that the evolution of dislocation density in the disordered structures confirms the observation from FEM [20], as well as from our simulation data (Section 4.3), that nodal shift broadens the elastic-plastic transition though the initial elasticity never ceases to exist.

Examples of the defect structures of the ordered sample $A^0_{0.303}$ and the disordered sample $A^{0.23}_{0.303}$ at $\varphi = 0.2$ are shown in Figure 4.8. It can be seen, especially in the magnifications, that plastic events can happen at practically any sites along the length of a ligament. Our observation, thus, does not support the results of Ref. [20] where plasticity is reported to happen solely at the ligament-to-node transition.

The presentation here confirms that dislocations are the carrier of the plasticity in diamond-lattice structures. Moreover, since the dislocation density of disordered samples is much higher than that of the ordered sample, it also endorses dislocations and their interactions as the underlying mechanisms for the improvement of strain hardening in the stress strain curves of the disordered

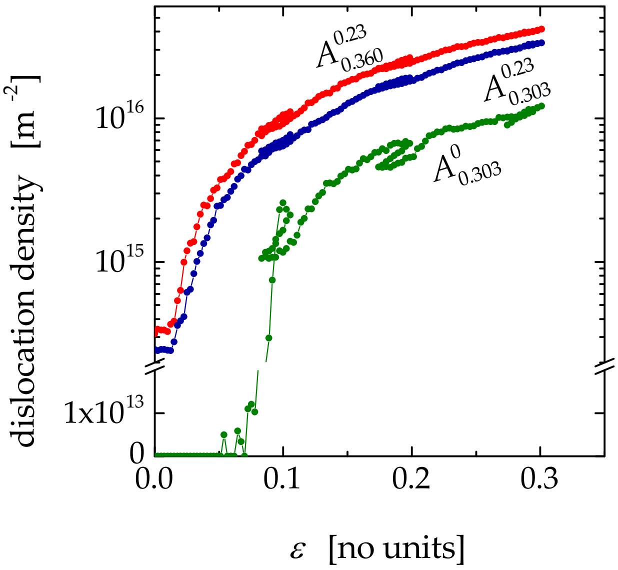

Figure 4.7: Evolution of dislocation densities of the ordered diamond-lattice sample and its disordered counterparts during the deformation event shown in Figure 4.3. No dislocation densities were detected in the ordered for true strains $\varepsilon \lesssim 0.05$. Pre-existing dislocation densities were found in the disordered samples prior to the onset of straining and remains almost constant for $\varepsilon \lesssim 0.01$. The ordinate is broken from 2×10^{13} to 10^{14}. Ordinate intervals below and above this broken range are linear-scale and log-scale, respectively.

samples. The very high Taylor work hardening employed in the FEM analysis in Refs. [20, 34] is thus also supported by our simulation results.

4.9 SUMMARY

The mechanical behavior of an ordered diamond-lattice sample and its disordered counterparts was investigated. Under compression the stress-strain curves of these samples exhibit a well-defined elasticity with high modulus preceding the yield behavior at high strength. The present simulation data suggest a transition from stretching to bending when a nodal shift is introduced; though the structures are still stretch-dominated. The nodal shift has strong influence on the elastic modulus, yield strength, elastic-plastic transition, and lateral expansion of the diamond-lattice structures. Yet, many aspects of the mechanical behavior of dealloyed NPG is not captured, even with the optimal nodal shift as is suggested in the previous development of the model.

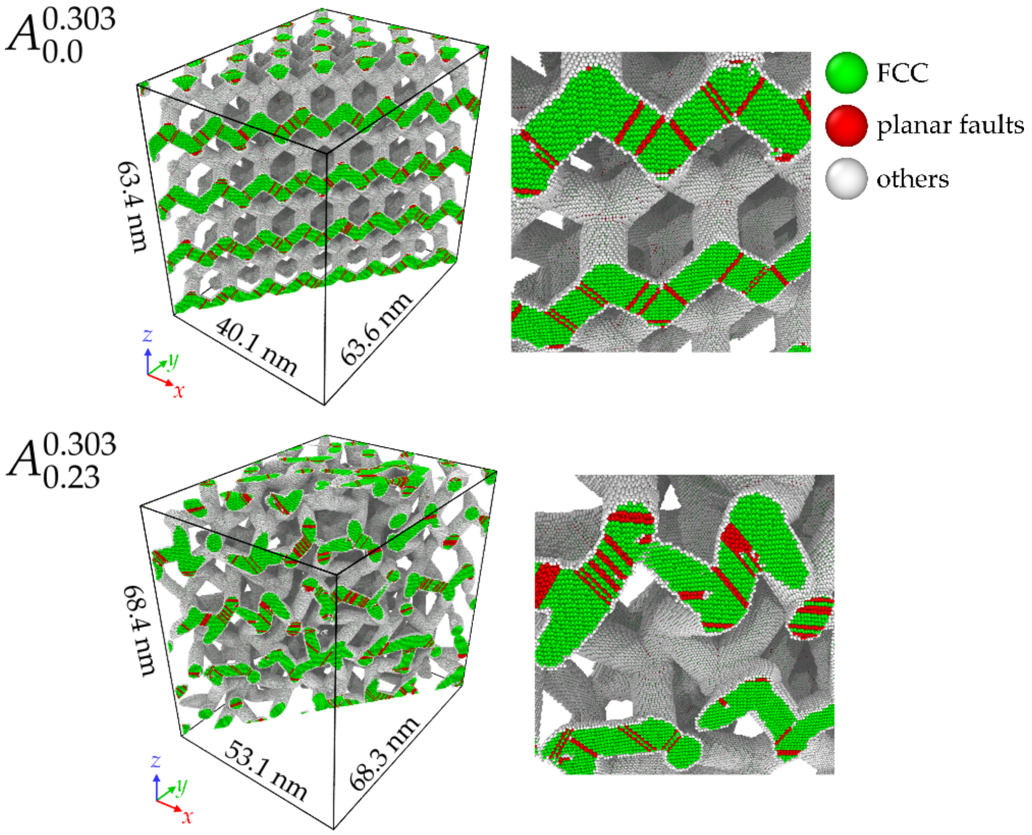
$A^{0.303}_{0.0}$
63.4 nm
40.1 nm
63.6 nm
z
y
x
FCC
planar faults
others
$A^{0.303}_{0.23}$
68.4 nm
53.1 nm
68.3 nm
z
y
x

Figure 4.8: Examples of lattice defects in the ordered sample $A^{0}_{0.303}$ and the disordered sample $A^{0.23}_{0.303}$ at the compressive true strain of 0.2. Loading direction is in the x direction. The magnifications exemplifies the observation that plasticity happens not only locally at the transition from the ligaments to the nodes, but also at the middle of the ligaments. To help visualize the results, only halves of the simulation boxes (divided by the rectangles made of opposite edges and face diagonals) are shown.

5

INFLUENCE OF LIGAMENT CONNECTIVITY ON ELASTIC MODULUS

In the previous Chapter, we studied the influence of the first (macroscopic) topological parameter that might influence the behavior of NPG, namely the topological disorder caused by nodal shift. In that context, our attention was put on the position of the nodes rather than on how the nodes are connected. In the greater part of this Chapter, we will look into the situation where ligament connectivity or the lack thereof might influence the elastic behavior of NPG. Afterwards, we will come back to the discussion of the relevant atomistic processes that might give rise to the anomalous compliance of NPG.

5.1 A MISSING BRICK IN THE GIBSON-ASHBY SCALING LAW: LIGAMENT CONNECTIVITY

The discussion concerning how the network connectivity might influence the elastic response of NPG, first raised by Mameka et al. [35], has recently gained its momentum [35–39]. It was based on a simple observation: If we look at the Gibson-Ashby equation for the elastic modulus of a metal foam [33],

$$Y^{\text{eff}} = C_{\text{E}} Y^{\text{bulk}} \varphi^2, \tag{5.1}$$

we see that, in order to predict Y^{eff} from Y^{bulk}, one just need to know the amount of materials contained in the total foam volume ($C_{\text{E}} = 1$ for metal foam). Consequently, constituent elements in the foam network are all assumed to contribute to the effective behavior of foam as a whole. That assumption, however, seems not to hold when we look at the ligament network of NPG: Many "dangling" ligaments that are connected to the network via just one end while the other end is hanging around in the pore space - indeed, some examples of those ligaments in experimental NPG can be seen in Figure 1.1. Those ligaments, though obviously contribute to the solid fraction of the structure, are free to move and thus might not contribute to the macroscopic mechanical behavior of the network.

Only those ligaments which are fully connected with both ends will form load-bearing rings which are responsible for reaction to the external load. A sketch of this situation is shown in Figure 5.1.

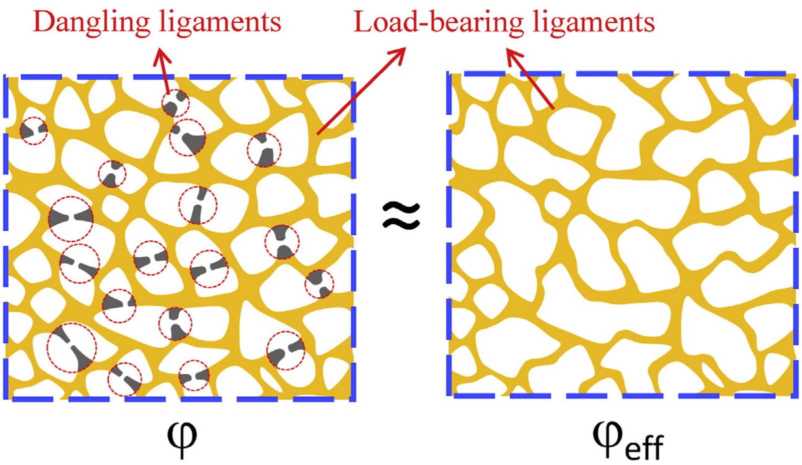

Figure 5.1: Influence of ligament connectivity on the effective solid fraction of NPG. Figure at left illustrates an NPG sample with solid fraction φ. Many ligaments in this sample are broken, resulting in dangling ligaments (grey) which have one end hanging about in the pore space. These dangling ligaments are not responsive to the external load applied on the sample. Other unbroken ligaments (yellow) form load-bearing rings and thus collectively respond to the external load. The behavior of the system at left is therefore equivalent to the behavior of a counterpart system (with effective solid fraction φ_{eff}) in which all dangling ligaments are removed (right). Reprinted from Liu *et al*. Acta Materialia 118 (2016): 77-87, with permission from Elsevier.

Consequently, the material becomes softer under external load due to the existence of disconnected ligaments. Any interpretation or modification of the Gibson-Ashby equation, thus, should be based on an analysis of the connectivity of the ligament network.

Following that line of argument, there have been several attempts to describe the connectivity of ligament network and its relation to the elastic modulus of NPG [37–39] - though their conclusions are not always mutually consistent.

Based on their experimental data for coarse NPG samples (ligament diameter > 30 nm), Liu et al. [37] suggested a modification to the Gibson-Ashby scaling equation via replacing the solid fraction φ of NPG by an effective solid fraction φ_{eff} that reflects the disconnectivity in the ligament network:

$$Y^{\mathrm{eff}} = Y^{\mathrm{bulk}} \varphi_{\mathrm{eff}}^{2}. \tag{5.2}$$

Yet, the corresponding discussion in Ref. [37] did not lead to any quantifiable measure for the connectivity of the ligament network. It, however, emphasizes the dependence of the elastic modulus of NPG on the synthesis protocol as well as heat treatment prior to straining because these two procedures lead to substantial changes in the network connectivity.

Mangipudi et al. [38] took another route to tackle the problem. They retained the solid fraction of NPG as an important parameter. Yet, they argued that the prefactor C_E should not necessarily be any constants, but rather a varying parameter that depends on a measure of connectivity of the ligament network. Then, they employed the concept of "scaled genus" [68, 69] to quantify the connectivity of NPG structures. Remarkably, their analysis revealed a striking linear relation between the prefactor C_E and the scaled genus. This implies that the huge discrepancy in reported elastic modulus of NPG, be them from nanoindentation, from macroscopic mechanical testing, or from molecular dynamics simulation, can be reconciled by simply redefining the prefactor C_E as a function of network connectivity. The classical Gibson–Ashby scaling equations thus remain their validity when taking into account the ligament connectivity.

The later work by Hu et al. [39], however, offered a different perspective. They suggested that although the ligament connectivity is obviously an important factor that is needed in describing the elasticity of NPG, it seems not to permeate into the discussion via simplistic correction of the Gibson-Ashby equation. In fact, using FEM analysis, they went further to compare the elastic modulus of the Gibson-Ashby model with that of the reconstructed model of an experimental NPG structure. While both samples have similar solid fraction and scaled connectivity, the reconstructed model is much more compliant. The Gibson-Ashby cubic model, thus they argued, is not a viable choice to represent the ligament network of NPG.

Despite some difference in their results, the studies in Refs. [37–39] all promote the importance of the ligament connectivity in the discussion of the elastic modulus of NPG. Motivated by the findings in these works, we will join this discussion with data from molecular dynamics simulations.

5.2 MICROSTRUCTURES AND STRESS-STRAIN BEHAVIOR

To obtain NPG samples with different connectivity, we used two different methods to mimic spinodal decomposition, namely via Monte Carlo simulation and via superposition of 48 composition waves (see Chapter 2 for details). For each method, three samples at different densities were generated. To rule out the influence of surface effects, all samples were prepared so that their ligament diameter is almost identical ($\sim$ 3.8 nm in accordance with the conversion rule 3.1). Examples of the microstructures of these samples are shown in Figure 5.2.

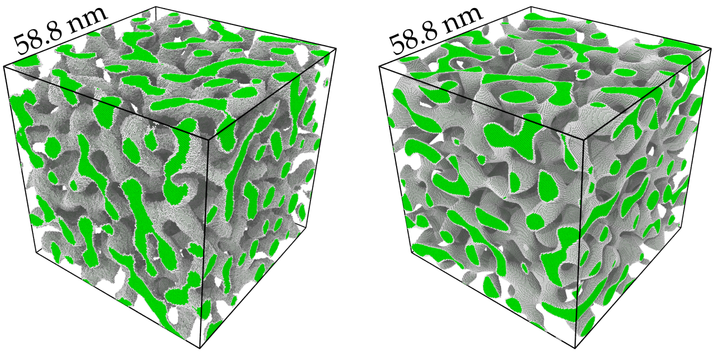

(a) (b)

Figure 5.2: Examples of the initial microstructure of samples studied in this Chapter. These samples were created via mimicking spinodal decomposition by (a) Monte Carlo simulation and by (b) superposition of 48 composition waves. For simulation details, see Chapter 2. Both samples have the same as-created solid fraction $\varphi_{\text{ini}} = 0.302$. Note the disordered network of both samples. For brevity, surface atoms and bulk atoms are coded in different colors.

As is discussed in Chapter 3, plasticity due to the action of capillary forces during the initial thermal relaxation at 300 K leads to dislocation nucleation during the thermal relaxation and slightly increased the solid fraction of these structures. Take for example the wave NPG sample with the as-created solid fraction of 0.340, its solid fraction increased to 0.349 after the initial thermal relaxation. Thus, for brevity, the NPG samples in this chapter will be denoted either by MC–φ_{relaxed} for Monte Carlo samples or W–φ_{relaxed} for wave samples, with φ_{relaxed} denoting the solid fraction after the thermal relaxation.

The stress-true strain curves of the MC and wave samples are shown in Figure 5.3. It is remarkable that, if we compare the behavior of MC and wave samples with similar initial solid fraction, the wave samples are stronger than the MC samples: Their flow stress levels are always higher than that of the respective MC sample with similar initial solid fraction. For example, at $\varepsilon = 0.1$, the flow stress of sample W–0.349 is $\sigma \approx 63$ MPa, as compared to $\sigma \approx 21$ MPa of sample MC–0.346.

Both sets of data for the MC and wave samples feature quasi-immediate yielding and pronounced strain hardening. Since this observation is consistent with the behavior of the sample created by Monte Carlo simulation in Chapter 3, the detailed discussions concerning early yielding and strengthening mechanisms of

Sample	L_s [nm]	φ_{ini}	φ_{relaxed}	α [1/nm]	d [nm]
W—0.313	58.75	0.302	0.313	0.890	3.70
W—0.349	56.71	0.340	0.349	0.852	3.79
W—0.388	54.26	0.380	0.388	0.834	3.87
MC–0.308	58.75	0.302	0.308	0.877	3.76
MC–0.346	58.75	0.340	0.346	0.854	3.78
MC–0.386	58.75	0.380	0.386	0.832	3.88

Table 5.1: Summary of microstructural information of samples created via mimicking spinodal decomposition by different methods. L_s, φ_{ini}, φ_{relaxed}, α, and d denote the sample length, initial (as-created) solid fraction, solid fraction after thermal relaxation at 300 K, ratio of surface area per solid volume, and characteristic ligament size, respectively.

the sample in that chapter can be transferred and applied to the set of samples that we are investigating in this chapter.

5.3 EVOLUTION OF ELASTIC MODULUS

Figure 5.4 shows the evolution of the effective elastic modulus, Y^{eff}, calculated from unload segments of the stress-strain curves plotted in Figure 5.3. The graphs show that all samples experience substantial stiffening during the compression, irrespective of how they were created or what their solid fraction is. For example, the initial value of Y^{eff} of the wave sample W–0.349 is 1.76 GPa. After deformation, that value increases more than 2 times, to the final value of 3.70 GPa.

Figure 5.4 shows that the effective elastic moduli of the wave samples are way greater than those of the MC samples of similar initial solid fraction. To give an instance: As compared to the initial $Y^{\text{eff}} = 3.70$ GPa of the wave sample W–0.349, the corresponding value of sample MC–0.346 is only 890 MPa, which is about 2 times more compliant.

How are these values compared to the prediction of the Gibson-Ashby equation? The results of $Y^{\text{eff}}/Y^{\text{bulk}}$ versus φ^2 for the initial modulus and solid fraction are shown in Figure 5.5a, along with the Gibson-Ashby scaling law. The same plot, but for the values calculated from the unload segments, is shown in Figure 5.5b. Once again, these figures obviously demonstrate systematic failures of the Gibson-Ashby equation in predicting the elastic moduli of virtual NPG samples:

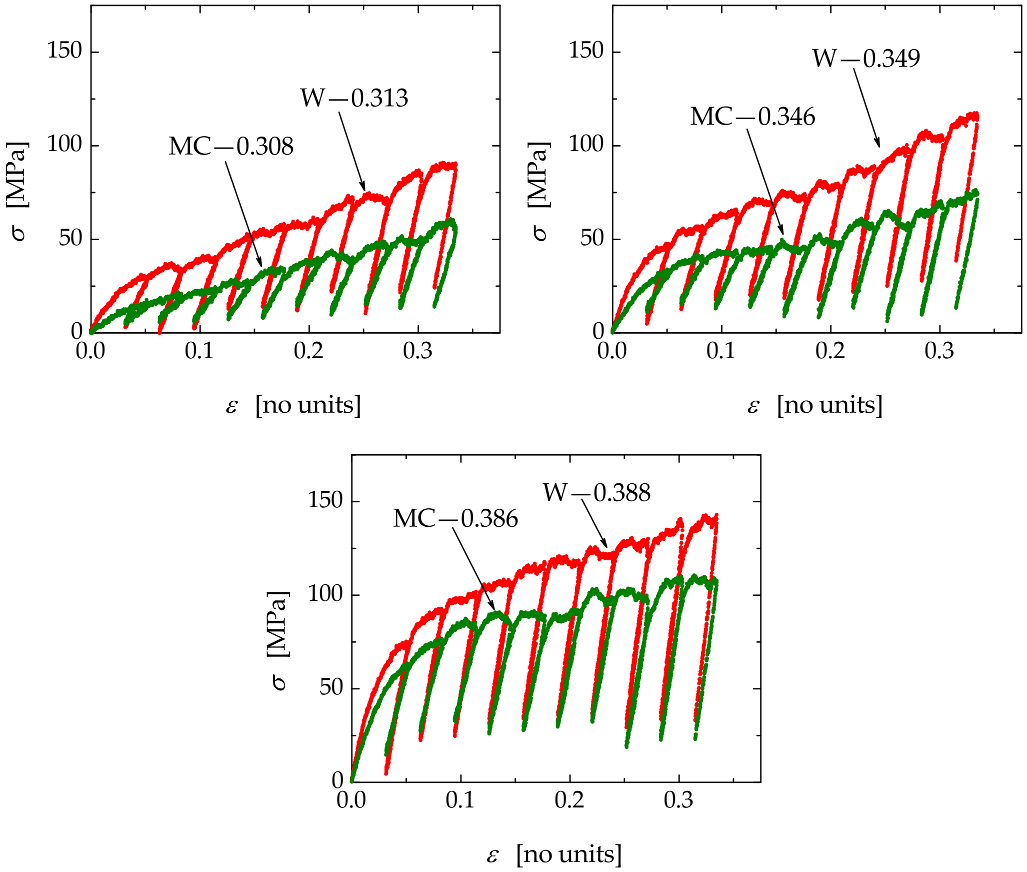

Figure 5.3: Simulated stress–true strain (σ–ε) curves of samples created by Monte Carlo (MC) simulation (green) and wave (W) method (red). Wave samples are much stronger than MC samples of similar solid fraction. These stress-strain curves were simulated with a strain rate of 10^8/s at 300 K.

It fails to predict not only the initial modulus but also the value of Y^{eff} at different strain stages when the material has already experienced substantial stiffening.

5.4 EVOLUTION OF CONNECTIVITY

We now assess the evolution of connectivity during the deformation of the virtual NPG samples. Here, we follow Refs. [38, 68, 69] and adopt the genus, g, as the measure of network connectivity*. For that purpose, the surface of the virtual NPG samples at different strain states was reconstructed via alpha-shape

---

*Note that one might also use the so-called connectivity, C, of a system, as in Ref. [39, 97, 98]. g and C are interchangeable, since $C = 1 - \chi$, and therefore, $C = 2g - 1$.

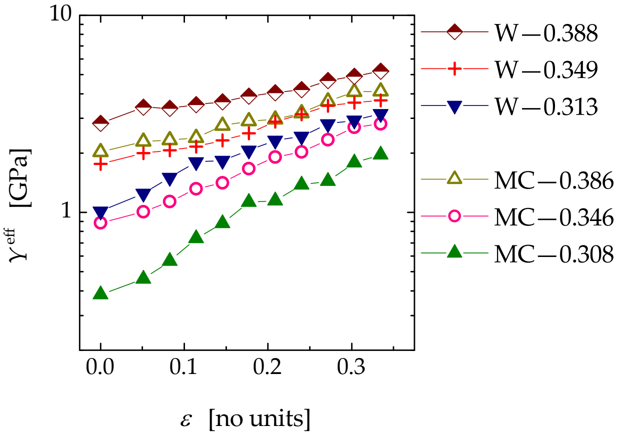

Figure 5.4: Evolution of effective elastic modulus, Y^{eff}, of samples with simulated stress-strain curves shown in Figure 5.3. All samples exhibit substantial stiffening as the deformation proceeds. Wave samples are much stiffer than MC samples of similar solid fraction.

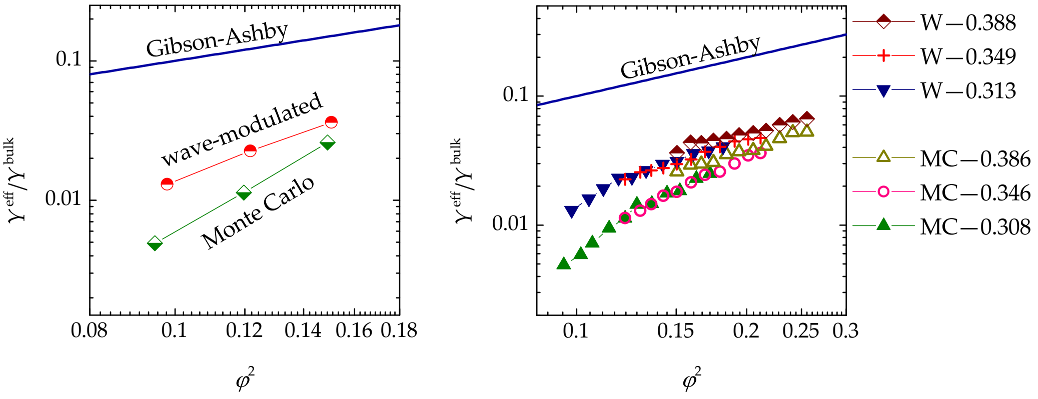

(a)

(b)

Figure 5.5: Comparing simulation data (points) with prediction of the Gibson–Ashby scaling law for elastic modulus (blue lines). Gibson-Ashby law fails to predict not only the initial modulus but also the value of Y^{eff} at different strain stages when the material has already experienced substantial stiffening.

method (see Chapter 2). The obtained reconstructed surface is a triangulated surface mesh, which allows direct calculation of g via Euler characteristic, χ,

$$g = 1 - \frac{\chi}{2} \qquad \text{with} \qquad \chi = \#V - \#E + \#F, \qquad \text{(Equation 2.35)}$$

where $\#V$, $\#E$, and $\#F$ are the number of vertexes, edges, and faces of the reconstructed surface. From here, we also get the genus density, g_V, which is define as genus g divided by the total volume V:

$$g_V = \frac{g}{V}. \tag{5.3}$$

The results for genus density g_V of the virtual NPG samples at different deformation states are shown in Figure 5.6a. The absolute change of genus, Δg, is plotted in Figure 5.6b.

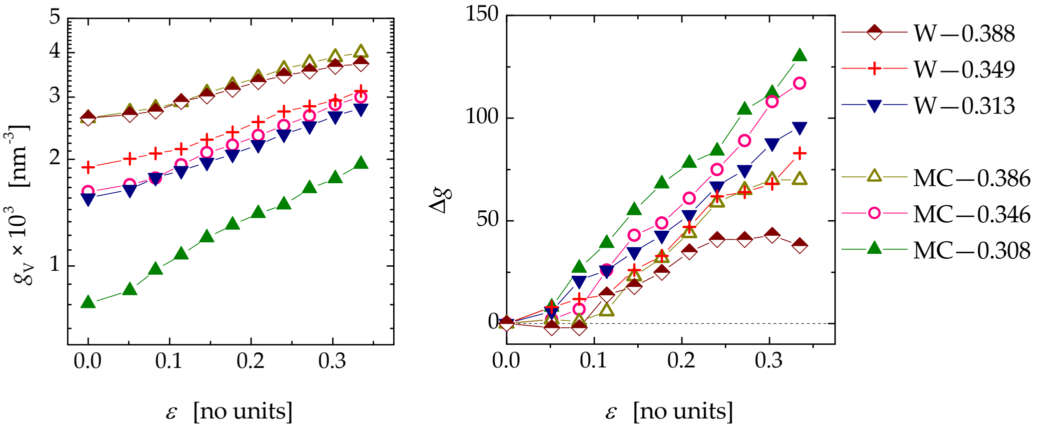

(a)

(b)

Figure 5.6: Evolution of connectivity during deformation. Figures (a) and (b) show the genus density, g_V, and absolute change of genus, Δg, of spinodal decomposition samples during the deformation events shown in Figure 5.3. Note the substantial increase of g_V of all samples during the deformation. This increase is mostly due to formation of new ligament connections, as quantified in (b), as well as exemplified in Figure 3.7.

In Figure 5.6a, we see that g_V of all samples increases as the deformation proceeds. The reason for the increase, apart from the ensuing reduction of total volume, is because of the creation of new connectivity (Figure 5.6b). Indeed, as is pointed out in Chapter 3, compression of NPG leads to the coalescence of ligaments and thus new connectivity is formed where the surface is cold-welded.

Comparing between the data of the MC and wave samples we see that, if the initial solid fraction φ is ~ 0.30 or ~ 0.34, then the initial value of g_V of the wave samples are greater than that of the MC samples. Yet, when the initial solid fraction φ is ~ 0.38, g_V of the MC and the wave samples are almost identical ($\sim 2.62 \times 10^{-3}\,\text{nm}^{-3}$). Note that, by construction, the MC samples were subject to coarsening processes during MC simulations. The generation of wave samples involved only predefined composition waves and thus did not entail any coarsening. Our observation is therefore consistent with previous studies [68, 69] where the connectivity in bi-continuous systems were analyzed: For solid fraction $\varphi \lesssim 0.36$, coarsening leads to loss of connectivity.

When discussing the connectivity of bi-continuous systems, an important information is the scaled genus density g_{scaled} [68, 69]. This parameter is simply defined as the genus density g_{V} multiplied by a measure of characteristic volume and, therefore, independent of length scale. If we use a cube with edge length of $1/S_{\mathrm{V}}$ as characteristic volume, then:

$$g_{\mathrm{scaled}} = \frac{g_{\mathrm{V}}}{S_{\mathrm{V}}^3} \qquad \text{with} \qquad S_{\mathrm{V}} = \frac{S}{V}, \tag{5.4}$$

in which S and V are the total surface area and total volume of the NPG structure, respectively. On the other hand, if the specific surface area α, i.e. surface area divided by the solid volume, is in place of S_{V}, we have :

$$\widetilde{g}_{\mathrm{scaled}} = \frac{g_{\mathrm{V}}}{\alpha^3}. \tag{5.5}$$

The results for both definitions of g_{scaled} are plotted in Figure 5.7. As is can be seen, there is no clear trend in the change of g_{scaled} during the deformation: While the graphs of sample MC–0.308 and large-strain states of sample MC–0.346 shows increasing g_{scaled}, all other graphs exhibit decreasing tendency. On the contrary, $\widetilde{g}_{\mathrm{scaled}}$ increases under compression of all NPG samples.

5.5 ELASTIC MODULUS *VS.* SCALED CONNECTIVITY DENSITY

Figure 5.4 and Figure 5.6 offers the first glimpse of the relation between the ligament connectivity of NPG samples and the corresponding elastic modulus: The increase of g_{V} happens at the same time when the effective elastic modulus Y^{eff} of NPG samples also increases substantially. The influence of connectivity on elastic behavior of NPG proposed in Refs. [35, 37–39] is thus somewhat backed up by our data. Yet, the simulation data of samples MC–0.386 and W–0.388 show that their elastic moduli are substantially different (2.03 GPa vs. 2.83 GPa), despite the fact that these two samples have almost identical amount of connectivity in a unit volume ($\sim 2.62 \times (10\mathrm{nm})^{-3}$).

For a quantitative relation between the elastic modulus of NPG structure and its ligament connectivity, we first need to single out the influence of solid fraction. For that purpose, we take the same approach of Mangipudi et al. [38] and assume

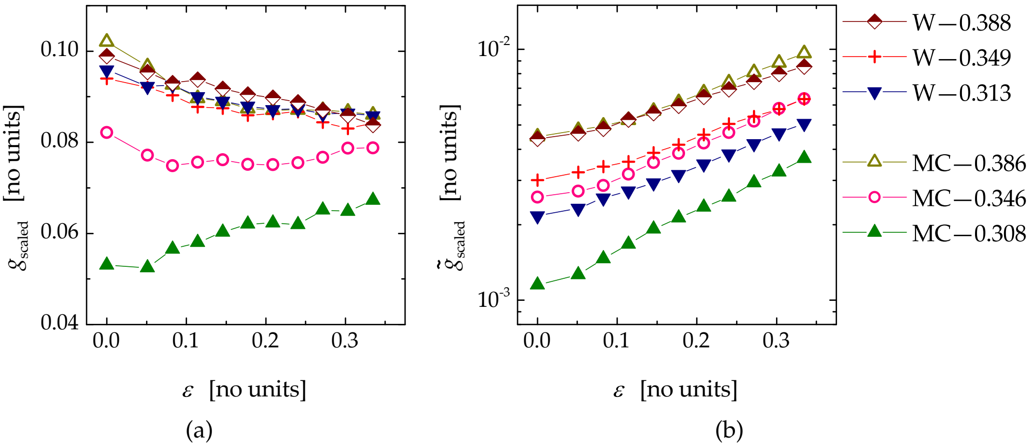

Figure 5.7: Change of scaled genus density of spinodal decomposition samples during the deformation events shown in Figure 5.3. Both definitions of scaled connectivity, namely (a) $g_{\mathrm{scaled}} = g_V S_V^{-3}$ and (b) $\tilde{g}_{\mathrm{scaled}} = g_V \alpha^{-3}$ (see main text for details), are shown. Except for sample MC–0.308, g_{scaled} decreases during the deformation. $\tilde{g}_{\mathrm{scaled}}$ of all samples, on the other hand, increases substantially during the deformation.

that the density effect directly goes into the power law φ^2 as in the Gibson-Ashby equation. Influence of other factors - including connectivity - therefore goes into the prefactor C_E. On a side note, at any deformed state with the solid fraction φ of the NPG structure, $\varphi\sqrt{C_E}$ is nothing else than the effective solid fraction φ_{eff} in Equation 5.2.

The values of C_E calculated from the initial modulus and solid fraction of the virtual NPG samples are plotted against the corresponding g_{scaled} in Figure 5.8a, along with the linear relation $C_E = 5g_{\mathrm{scaled}}$ suggested by Mangipudi et al. [38]. As is clearly seen, our data do not follow the linear relation $C_E = 5g_{\mathrm{scaled}}$. In fact, the current data do not demonstrate any linear relation between C_E and g_{scaled} at all. If we break the data sets down to the samples created by different methods, we observe a monotonic relation between C_E and g_{scaled} of the MC samples. Yet, that trend does not show up in the data set for the wave samples: There is a scatter by a factor of almost 1.8 in C_E while their g_{scaled} values are almost around 0.095.

If $\tilde{g}_{\mathrm{scaled}}$ is used instead of g_{scaled}, we get a better relation between the initial values of C_E and scaled genus density, as is plotted in Figure 5.8b. Indeed, for samples created by the same method, C_E increases when $\tilde{g}_{\mathrm{scaled}}$ increases. Yet, again, there is no linear relation between C_E and $\tilde{g}_{\mathrm{scaled}}$ if data of all samples are taken into account.

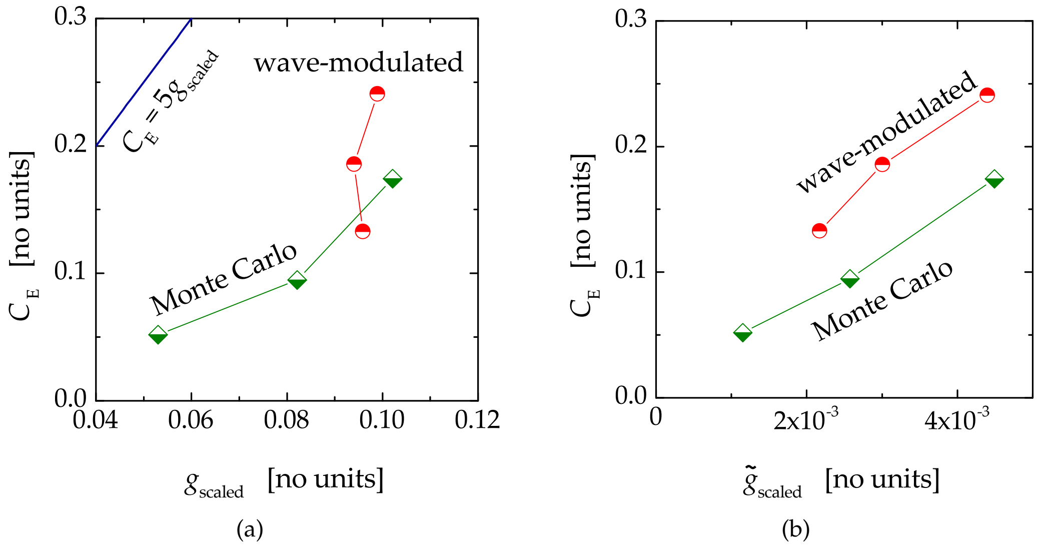

Figure 5.8: Pre-factor, C_E, in the Gibson-Ashby scaling law versus scaled genus density. This figures are for data points at zero strain. Results for both definitions of scaled connectivity, namely (a) $g_{\mathrm{scaled}} = g_\mathrm{V} S_\mathrm{V}^{-3}$ and (b) $\tilde{g}_{\mathrm{scaled}} = g_\mathrm{V} \alpha^{-3}$ (see main text for details), are shown. The linear relation $C_\mathrm{E} = 5g_{\mathrm{scaled}}$ [38] is also shown in (a). No one-to-one relations between the pre-factor and the scaled genus density can be recovered from the present data set.

Our simulation data at zero strain therefore do not support a direct connection between C_E and g_{scaled} (both definitions). That situation becomes even worse when deformation-induced changes are taken into account. For example, Figure 5.9 shows C_E *vs.* $\tilde{g}_{\mathrm{scaled}}$ calculated at different strain states. It obviously disputes any expected one-to-one relation between C_E and $\tilde{g}_{\mathrm{scaled}}$.

Altogether, as opposed to the results of Ref. [38], a quantitative relation between C_E and scaled genus density cannot be established with our simulation data - for the initial elastic modulus as well as for effective values at deformed states. A similar conclusion was obtained by Hu et al. on different grounds [39]. This, however, does not rule out the influence of ligament connectivity on the elastic modulus of NPG. After all, if we look at each sample separately, their effective modulus increases at the same time when genus density increases. It might be that we need other means to disentangle the influence of ligament connectivity from the influence of solid fraction.

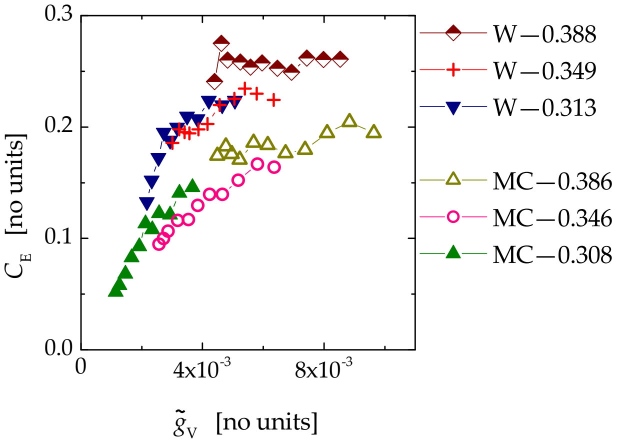

Figure 5.9: Pre-factor, C_E, in the Gibson-Ashby scaling law versus scaled genus density, with $\tilde{g}_{\text{scaled}} = g_V \alpha^{-3}$ (see main text for details), during the deformation events of Figure 5.3. Similar to Figure 5.8, no one-to-one relations between the pre-factor and scaled connectivity can be recovered from the data set of this figure.

5.6 INFLUENCE OF SURFACE EFFECTS

Our detour to investigate the influence of network topology on the behavior of NPG suggested that the anomalous compliance of the material is not a trivial result and the reason for its unique behavior is indeed a riddle. Attempts to explain this behavior with the bulk-level topological disorder or ligament connectivity have not yielded a satisfactory and convincing answer. This prompts us to go back to atomistic level and assess relevant processes that might have an impact on the elastic response of NPG.

In Chapter 3, we have pointed out that surface-induced stress causes plastic deformation, and thus dislocation nucleation, of the virtual samples during the thermal relaxation at 300 K. These samples therefore start out the deformation process with a significant amount of preexisting dislocations. It has been long-documented (e.g. see Refs. [99–102]) that cold-worked materials exhibit reduced effective elastic modulus due to the bow-out of dislocation segments between their anchor points. Take for example polycrystalline pure iron at room temperature [101]: The effective elastic modulus decreased from the original mean value of 210 GPa to a mean value of 196 GPa after deformation to the engineering strain of 0.06. We thus expected the same influence of preexisting dislocations on the effective modulus of NPG. Yet, we have seen in Chapter 3 that the behavior of the NPG sample at $T = 0.01$ K without any preexisting dislocations is practically the same with its behavior at 300 K with preexisting dislocations. The influence of preexisting dislocations is therefore not a decisive factor.

It is well-established that the elasticity of nanowires is size-dependent and strongly impacted by high-order elasticity effects (see, e.g., [40, 103–106]). As an interconnected network of nano-scale filaments, the elastic behavior of NPG, specifically its anomalous compliance, is thus expected to depend on surface-related phenomena, such as pre-strained state of the bulk due to the action of capillary forces [72].

In order to check this argument, we selected several deformed configurations of sample MC–0.308 at different strain states during the simulated compression test. The surface of these deformed configurations was then reconstructed and fed to FEM simulation* to study the elastic behavior. To rule out the influence of complex nonlinear effects that are intrinsic of the EAM potential used in MD, the respective FEM simulation used only the linear elastic constants of the EAM potential. Moreover, the influence of network topology is also ruled out because the input structures for FEM study were constructed from the atomistic configurations.

Results for the elastic moduli in FEM are shown in Figure 5.10, along with the values from molecular dynamics. Clearly, the elastic modulus of the NPG structures exhibits a very much stiffer behavior in FEM than in molecular dynamics simulation. Take for example the initial data points, while the molecular dynamics simulation gives a value of only 380 MPa, the corresponding FEM value is 1.06 GPa - a factor of 2.8 stiffer.

Since FEM used exclusively the linear elastic constants from the EAM potential, the difference presented in Figure 5.10 must come from the the nonlinear effects. We consider this as a decisive evidence of the influence of surface-related phenomena on the elastic behavior of NPG, particularly its anomalous compliance.

It is unclear which of the surface-related phenomena, or their combination, will determine the compliant behavior. For example, one might link the observed behavior to excess elasticity [106–108], as is backed up by recent experimental study [31] where the effective modulus of NPG was shown to change in accordance with changes of surface state. Yet, recent study within the continuum framework based on calculation of density functional theory [109] demonstrated only a minor influence of surface elasticity on effective modulus of nanowires.

Based on our simulation data, we now advocate a possible mechanism that might lead to the anomalous compliance of NPG, namely surface-induced shear instability.

---

*The FEM data presented in this Section were kindly provided by the courtesy of Benedikt Roschning (benedikt.roschning@tuhh.de) at TUHH.

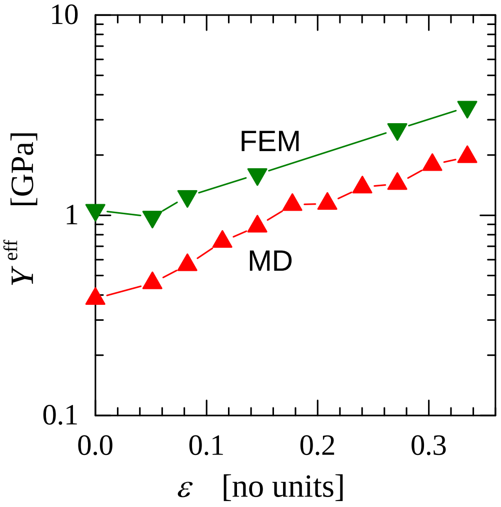

Figure 5.10: Influence of nonlinear effects. Effective Young's modulus, Y_{eff}, versus plastic strain, ε. Data from molecular dynamics (MD) and linear-elastic finite element method (FEM) simulations for sample MC–0.308. Note the substantially stiffer behavior of the linear elastic solid, in spite of identical network geometry.

In Section 3.2, we pointed out that the surface stress induces shear stresses which exceed the theoretical shear strength in some ligaments and closely approach it in others. Since the theoretical shear strength is determined by a point of inflection in the generalized stacking fault energy curve, it entails a vanishing shear modulus. This is illustrated schematically in Figure 5.11. In other words, the surface-induced stress and the concomitant shear will systematically reduce the shear stiffness of the ligaments in NPG. This is well consistent with the anomalous compliance of the material in its initial state. Furthermore one expects that, as the deformation proceeds, more and more of these near-unstable regions will be pushed over to stable faulted or twinned configurations, relaxing their stress and reverting back to a configuration of conventional, high shear stiffness. This agrees with the observed stiffening during the early stages of plastic deformation. Even though the shear instability in this picture seems unusual, it is well supported by all observations of our work.

5.7 SUMMARY

In the greater part of this Chapter, we investigated the influence of the ligament connectivity on the elasticity of NPG. For that purpose, two different methods were used to create samples via mimicking spinodal decomposition, namely via

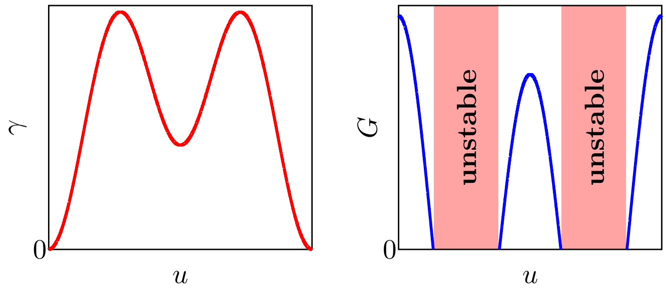

Figure 5.11: Schematic illustration of shear instability. Graph at left shows the generalized stacking fault energy function, γ, versus shear displacement, u, between adjacent atomic planes. Graph at right shows the associated variation of the shear modulus, G, which scales with the second derivative of $\gamma(u)$. The negative-valued second derivative between the points of inflection of $\gamma(u)$ implies instability to shear.

Monte Carlo simulation and via superposition of modulated waves. Both techniques lead to samples that resemble the ligament network of NPG. Yet, the mechanical properties of these samples are vastly different. Although our simulation data support the influence of ligament connectivity on the elastic modulus of NPG, a concrete quantitative relation between measures of connectivity and elasticity has not been resolved.

We then studied the impact of surface-related nonlinear effects on the elastic modulus. The results confirm the nonlinear effects as the origin of the anomalous compliance of NPG - though possibly only at very small length scale. To that end, we attribute the surface-induced shear instability as the underlying process that gives rise to the observed behavior.

6

SUMMARY AND OUTLOOK

We have presented a study of elasticity and plasticity of NPG, using molecular dynamics simulations. The central theme was to explore and explain the unusual weak and compliant behavior of dealloyed NPG that has been extensively reported in experiments. Our attempts have led us to look into possible atomistic processes and potential macroscopic structural parameters that might be relevant.

At the ligament level, we have learned that when it comes to the mechanical response of NPG, surface really matters. It is because of the surface-induced stress that NPG can yield without any help from external load - thus, we always observe preexisting lattice defects in thermally relaxed NPG samples. The heterogeneity of the surface-induced stress - depending on the local geometry and orientation of ligament segments - is also a significant contributor to the elastic-plastic transition in NPG. The tension-compression asymmetry previously reported [27] also roots back to the surface-induced stress: It favors compression over tension. Finally, when we turn off the influence of surface, NPG becomes very much stiffer.

We have also learned that although the NPG network is an assembly of nanoscale ligaments with long-distance lattice coherency, its plasticity bears no similarity to that of the nanowires: While nanoscale wires strengthen via dislocation-starvation mechanisms due to limited sources, the plasticity of NPG is carried by dislocations. Massive accumulation of dislocations and their interaction is observed; thus, in addition to a mere densification effect, NPG strengthen via drastic Taylor work hardening. In that respect, our simulation data and the electron backscattering diffraction data in Ref. [15] mutually support each other.

As for the diamond-lattice structure, our simulation data confirmed the influence of nodal shift. Both modulus and strength of the ordered diamond-lattice structure become very much lower if the nodal shift is introduced along with the correction of solid fraction. The nodal shift also leads to less expansion in the lateral dimensions and enhanced strain hardening due to lattice defects. Moreover, introducing nodal shift also broadens the elastic-plastic transition in the diamond-lattice structure.

The nodal shift, however, cannot remedy the pertinent deformation-induced loss of modulus of the diamond-lattice structure. In relation to the deformation mode at the ligament level, that loss of modulus indicates that the diamond-lattice structure is stretching-dominated. The nodal shift leads to transition from stretching to bending in some ligaments, yet the majority of them are still deformed by stretching. Thus, the initial effective modulus and strength of the disordered diamond-lattice structures remains high.

Ligament connectivity is another bulk-level topological parameter that has been investigated in this work. The simulation data, however, result in mixed messages. It is clear that deformation of virtual NPG (wave and MC) samples leads to increase in both effective modulus and connectivity. Besides, if we compare the initial modulus of wave and MD samples at similar solid fraction of ~ 0.30 or ~ 0.34, respectively, the wave samples have higher connectivity and stiffer behavior. Yet, that observation does not hold for samples with solid fraction of ~ 0.34: The wave and the MC samples have identical connectivity density, albeit the wave sample is much stiffer than the MC sample. Moreover, the linear relation between the prefactor in the Gibson-Ashby equation and the scaled genus density cannot be recovered with our simulation data.

Although our investigation has not been able to exclusively identify which of the surface-related phenomena that is responsible for the anomalous compliance of NPG, the influence of surface effects is undoubtedly demonstrated in our work. It is thus a natural step to discriminate different surface-induced mechanisms that might impact the mechanical behavior of NPG.

Our work clearly states the unsuitability of the Gibson-Ashby model - thus the sole role of solid fraction - in describing the behavior of NPG. Though we have observed a strong influence of topology on the mechanical properties of NPG, it is unclear how to quantitatively connect the topology of NPG to its mechanical behavior. Care and attention should be paid into this direction.

REFERENCES

[1] D. Kramer, R. N. Viswanath, and J. Weissmüller. Surface-Stress Induced Macroscopic Bending of Nanoporous Gold Cantilevers. *Nano Letters* **4** (2004) 793–796.

[2] J. Biener, A. Wittstock, L. A. Zepeda-Ruiz, M. M. Biener, V. Zielasek, D. Kramer, R. N. Viswanath, J. Weissmüller, M. Bäumer, and A. V. Hamza. Surface-Chemistry-Driven Actuation in Nanoporous Gold. *Nature Materials* **8** (2009) 47–51.

[3] H.-J. Jin and J. Weissmüller. Bulk Nanoporous Metal for Actuation. *Advanced Engineering Materials* **12** (2010) 714–723.

[4] H.-J. Jin, X.-L. Wang, S. Parida, K. Wang, M. Seo, and J. Weissmüller. Nanoporous Au-Pt Alloys As Large Strain Electrochemical Actuators. *Nano Letters* **10** (2010) 187–194.

[5] E. Detsi, Z. G. Chen, W. P. Vellinga, P. R. Onck, and J. T. M. De Hosson. Reversible Strain by Physisorption in Nanoporous Gold. *Applied Physics Letters* **99** (2011) 083104.

[6] E. Detsi, Z. G. Chen, W. P. Vellinga, P. R. Onck, and J. T. M. De Hosson. Actuating and Sensing Properties of Nanoporous Gold. *Journal of Nanoscience and Nanotechnology* **12** (2012) 4951–4955.

[7] Y. Ding, M. Chen, and J. Erlebacher. Metallic Mesoporous Nanocomposites for Electrocatalysis. *Journal of the American Chemical Society* **126** (2004) 6876–6877.

[8] C. Xu, J. Su, X. Xu, P. Liu, H. Zhao, F. Tian, and Y. Ding. Low Temperature CO Oxidation over Unsupported Nanoporous Gold. *Journal of the American Chemical Society* **129** (2007) 42–43.

[9] N. V. Lavrik, C. A. Tipple, M. J. Sepaniak, and P. G. Datskos. Enhanced Chemi-Mechanical Transduction at Nanostructured Interfaces. *Chemical Physics Letters* **336** (2001) 371–376.

[10] X. Y. Lang, L. Y. Chen, P. F. Guan, T. Fujita, and M. W. Chen. Geometric Effect on Surface Enhanced Raman Scattering of Nanoporous Gold: Improving Raman Scattering by Tailoring Ligament and Nanopore Ratios. *Applied Physics Letters* **94** (2009) 213109.

[11] R. Li and K. Sieradzki. Ductile-Brittle Transition in Random Porous Au. *Physical Review Letters* **68** (1992) 1168.

[12] F. Kertis, J. Snyder, L. Govada, S. Khurshid, N. Chayen, and J. Erlebacher. Structure/Processing Relationships in the Fabrication of Nanoporous Gold. *JOM* **62** (2010) 50–56.

[13] K. Wang and J. Weissmüller. Composites of Nanoporous Gold and Polymer. *Advanced Materials* **25** (2013) 1280–1284.

[14] S. Parida, D. Kramer, C. A. Volkert, H. Rösner, J. Erlebacher, and J. Weissmüller. Volume Change during the Formation of Nanoporous Gold by Dealloying. *Physical Review Letters* **97** (2006) 035504.

[15] H.-J. Jin, L. Kurmanaeva, J. Schmauch, H. Rösner, Y. Ivanisenko, and J. Weissmüller. Deforming Nanoporous Metal: Role of Lattice Coherency. *Acta Materialia* **57** (2009) 2665–2672.

[16] H.-J. Jin and J. Weissmuller. A Material with Electrically Tunable Strength and Flow Stress. *Science* **332** (2011) 1179–1182.

[17] C. A. Volkert, E. T. Lilleodden, D. Kramer, and J. Weissmüller. Approaching the Theoretical Strength in Nanoporous Au. *Applied Physics Letters* **89** (2006) 061920.

[18] J. Biener, A. M. Hodge, J. R. Hayes, C. A. Volkert, L. A. Zepeda-Ruiz, A. V. Hamza, and F. F. Abraham. Size Effects on the Mechanical Behavior of Nanoporous Au. *Nano Letters* **6** (2006) 2379–2382.

[19] L. Lührs, C. Soyarslan, J. Markmann, S. Bargmann, and J. Weissmüller. Elastic and Plastic Poisson's Ratios of Nanoporous Gold. *Scripta Materialia* **110** (2016) 65–69.

[20] N. Huber, R. Viswanath, N. Mameka, J. Markmann, and J. Weissmüller. Scaling Laws of Nanoporous Metals under Uniaxial Compression. *Acta Materialia* **67** (2014) 252–265.

[21] J. R. Greer and W. D. Nix. Nanoscale Gold Pillars Strengthened through Dislocation Starvation. *Physical Review B* **73** (2006) 245410.

[22] J. R. Greer, W. C. Oliver, and W. D. Nix. Size Dependence of Mechanical Properties of Gold at the Micron Scale in the Absence of Strain Gradients. *Acta Materialia* **53** (2005) 1821–1830.

[23] ASTM. E111 - 04(2010): Test Method for Youngs Modulus, Tangent Modulus, and Chord Modulus (2010).

[24] T. J. Balk, C. Eberl, Y. Sun, K. J. Hemker, and D. S. Gianola. Tensile and Compressive Microspecimen Testing of Bulk Nanoporous Gold. *JOM* **61** (2009) 26–31.

[25] A. Mathur and J. Erlebacher. Size Dependence of Effective Young's Modulus of Nanoporous Gold. *Applied Physics Letters* **90** (2007) 061910.

[26] R. Liu and A. Antoniou. A Relationship between the Geometrical Structure of a Nanoporous Metal Foam and Its Modulus. *Acta Materialia* **61** (2013) 2390–2402.

[27] D. Farkas, A. Caro, E. Bringa, and D. Crowson. Mechanical Response of Nanoporous Gold. *Acta Materialia* **61** (2013) 3249–3256.

[28] X.-Y. Sun, G.-K. Xu, X. Li, X.-Q. Feng, and H. Gao. Mechanical Properties and Scaling Laws of Nanoporous Gold. *Journal of Applied Physics* **113** (2013) 023505.

[29] J. Biener, A. M. Hodge, and A. V. Hamza. Chapter 12. Deformation Behavior of Nanoporous Metals. *Micro and Nano Mechanical Testing of Materials and Devices*. Ed. by F. Yang and J. C. Li. Boston, MA: Springer US, 2008.

[30] A. Hodge, R. Doucette, M. Biener, J. Biener, O. Cervantes, and A. Hamza. Ag Effects on the Elastic Modulus Values of Nanoporous Au Foams. *Journal of Materials Research* **24** (2009) 1600–1606.

[31] N. Mameka, J. Markmann, H.-J. Jin, and J. Weissmüller. Electrical Stiffness Modulation—confirming the Impact of Surface Excess Elasticity on the Mechanics of Nanomaterials. *Acta Materialia* **76** (2014) 272–280.

[32] L. J. Gibson and M. F. Ashby. The Mechanics of Three-Dimensional Cellular Materials. *Proceedings of the Royal Society A: Mathematical, Physical and Engineering Sciences* **382** (1982) 43–59.

[33] L. J. Gibson and M. F. Ashby. Cellular Solids: Structure and Properties. 2. ed. Cambridge solid state science series. Cambridge: Cambridge University Press, 2001.

[34] B. Roschning and N. Huber. Scaling Laws of Nanoporous Gold under Uniaxial Compression: Effects of Structural Disorder on the Solid Fraction, Elastic Poisson's Ratio, Young's Modulus and Yield Strength. *Journal of the Mechanics and Physics of Solids* **92** (2016) 55–71.

[35] N. Mameka, K. Wang, J. Markmann, E. T. Lilleodden, and J. Weissmüller. Nanoporous Gold—Testing Macro-Scale Samples to Probe Small-Scale Mechanical Behavior. *Materials Research Letters* **4** (2016) 27–36.

[36] X.-L. Ye and H.-J. Jin. Corrosion-Induced Strengthening: Development of High-Strength Nanoporous Metals. *Advanced Engineering Materials* **18** (2016) 1050–1058.

[37] L.-Z. Liu, X.-L. Ye, and H.-J. Jin. Interpreting Anomalous Low-Strength and Low-Stiffness of Nanoporous Gold: Quantification of Network Connectivity. *Acta Materialia* **118** (2016) 77–87.

[38] K. Mangipudi, E. Epler, and C. Volkert. Topology-Dependent Scaling Laws for the Stiffness and Strength of Nanoporous Gold. *Acta Materialia* **119** (2016) 115–122.

[39] K. Hu, M. Ziehmer, K. Wang, and E. T. Lilleodden. Nanoporous Gold: 3D Structural Analyses of Representative Volumes and Their Implications on Scaling Relations of Mechanical Behaviour. *Philosophical Magazine* (2016) 1–14.

[40] M. T. McDowell, A. M. Leach, and K. Gall. On The Elastic Modulus of Metallic Nanowires. *Nano Letters* **8** (2008) 3613–3618.

[41] D. Crowson, D. Farkas, and S. Corcoran. Geometric Relaxation of Nanoporous Metals: The Role of Surface Relaxation. *Scripta Materialia* **56** (2007) 919–922.

[42] D. A. Crowson, D. Farkas, and S. G. Corcoran. Mechanical Stability of Nanoporous Metals with Small Ligament Sizes. *Scripta Materialia* **61** (2009) 497–499.

[43] D. Frenkel and B. Smit. Understanding Molecular Simulation: From Algorithms to Applications. 2nd ed. Computational science series. San Diego: Academic Press, 2002.

[44] J. W. Cahn. Phase Separation by Spinodal Decomposition in Isotropic Systems. *The Journal of Chemical Physics* **42** (1965) 93.

[45] N. Metropolis, A. W. Rosenbluth, M. N. Rosenbluth, A. H. Teller, and E. Teller. Equation of State Calculations by Fast Computing Machines. *The Journal of Chemical Physics* **21** (1953) 1087.

[46] B. Hyde, H. D. Espinosa, and D. Farkas. An Atomistic Investigation of Elastic and Plastic Properties of Au Nanowires. *JOM* **57** (2005) 62–66.

[47] P. Mohammadi and P. Sharma. Atomistic Elucidation of the Effect of Surface Roughness on Curvature-Dependent Surface Energy, Surface Stress, and Elasticity. *Applied Physics Letters* **100** (2012) 133110.

[48] P. Mohammadi, L. Liu, P. Sharma, and R. Kukta. Surface Energy, Elasticity and the Homogenization of Rough Surfaces. *Journal of the Mechanics and Physics of Solids* **61** (2013) 325–340.

[49] S. Nosé. A Unified Formulation of the Constant Temperature Molecular Dynamics Methods. *The Journal of Chemical Physics* **81** (1984) 511.

[50] W. G. Hoover. Canonical Dynamics: Equilibrium Phase-Space Distributions. *Physical Review A* **31** (1985) 1695–1697.

[51] G. J. Martyna, M. L. Klein, and M. Tuckerman. Nosé–Hoover Chains: The Canonical Ensemble via Continuous Dynamics. *The Journal of Chemical Physics* **97** (1992) 2635.

[52] G. J. Martyna, M. E. Tuckerman, D. J. Tobias, and M. L. Klein. Explicit Reversible Integrators for Extended Systems Dynamics. *Molecular Physics* **87** (1996) 1117–1157.

[53] G. J. Martyna, D. J. Tobias, and M. L. Klein. Constant Pressure Molecular Dynamics Algorithms. *The Journal of Chemical Physics* **101** (1994) 4177.

[54] M. S. Daw and M. I. Baskes. Semiempirical, Quantum Mechanical Calculation of Hydrogen Embrittlement in Metals. *Physical Review Letters* **50** (1983) 1285–1288.

[55] M. S. Daw and M. I. Baskes. Embedded-Atom Method: Derivation and Application to Impurities, Surfaces, and Other Defects in Metals. *Physical Review B* **29** (1984) 6443–6453.

[56] S. M. Foiles, M. I. Baskes, and M. S. Daw. Embedded-Atom-Method Functions for the Fcc Metals Cu, Ag, Au, Ni, Pd, Pt, and Their Alloys. *Physical Review B* **33** (1986) 7983–7991.

[57] E. Kroener. Berechnung der elastischen Konstanten des Vielkristalls aus den Konstanten des Einkristalls. *Zeitschrift für Physik* **151** (1958) 504–518.

[58] S. Plimpton, C. Battaile, M. Chandross, L. Holm, A. Thompson, V. Tikare, G. Wagner, E. Webb, X. Zhou, C. G. Cardona, and A. Slepoy. Crossing the Mesoscale No-Man's Land via Parallel Kinetic Monte Carlo. *Sandia Technical Report.* SAND 2009-6226. 2009.

[59] S. Plimpton. Fast Parallel Algorithms for Short-Range Molecular Dynamics. *Journal of Computational Physics* **117** (1995) 1–19.

[60] A. Stukowski. Computational Analysis Methods in Atomistic Modeling of Crystals. *JOM* **66** (2014) 399–407.

[61] A. Stukowski. Structure Identification Methods for Atomistic Simulations of Crystalline Materials. *Modelling and Simulation in Materials Science and Engineering* **20** (2012) 045021.

[62] J. D. Honeycutt and H. C. Andersen. Molecular Dynamics Study of Melting and Freezing of Small Lennard-Jones Clusters. *The Journal of Physical Chemistry* **91** (1987) 4950–4963.

[63] D. Faken and H. Jónsson. Systematic Analysis of Local Atomic Structure Combined with 3D Computer Graphics. *Computational Materials Science* **2** (1994) 279–286.

[64] H. Tsuzuki, P. S. Branicio, and J. P. Rino. Structural Characterization of Deformed Crystals by Analysis of Common Atomic Neighborhood. *Computer Physics Communications* **177** (2007) 518–523.

[65] A. Stukowski and K. Albe. Extracting Dislocations and Non-Dislocation Crystal Defects from Atomistic Simulation Data. *Modelling and Simulation in Materials Science and Engineering* **18** (2010) 085001.

[66] A. Stukowski, V. V. Bulatov, and A. Arsenlis. Automated Identification and Indexing of Dislocations in Crystal Interfaces. *Modelling and Simulation in Materials Science and Engineering* **20** (2012) 085007.

[67] H. Edelsbrunner and E. P. Mücke. Three-Dimensional Alpha Shapes. *ACM Transactions on Graphics* **13** (1994) 43–72.

[68] Y. Kwon, K. Thornton, and P. W. Voorhees. The Topology and Morphology of Bicontinuous Interfaces during Coarsening. *EPL (Europhysics Letters)* **86** (2009) 46005.

[69] Y. Kwon, K. Thornton, and P. W. Voorhees. Coarsening of Bicontinuous Structures via Nonconserved and Conserved Dynamics. *Physical Review E* **75** (2007) 021120.

[70] A. Stukowski. Visualization and Analysis of Atomistic Simulation Data with OVITO–the Open Visualization Tool. *Modelling and Simulation in Materials Science and Engineering* **18** (2010) 015012.

[71] B.-N. D. Ngô, A. Stukowski, N. Mameka, J. Markmann, K. Albe, and J. Weissmüller. Anomalous Compliance and Early Yielding of Nanoporous Gold. *Acta Materialia* **93** (2015) 144–155.

[72] J. Weissmüller and J. Cahn. Mean Stresses in Microstructures due to Interface Stresses: A Generalization of a Capillary Equation for Solids. *Acta Materialia* **45** (1997) 1899–1906.

[73] M. E. Gurtin, J. Weissmüller, and F. Larché. A General Theory of Curved Deformable Interfaces in Solids at Equilibrium. *Philosophical Magazine A* **78** (1998) 1093–1109.

[74] S. Swaminarayan, R. Najafabadi, and D. Srolovitz. Polycrystalline Surface Properties from Spherical Crystallites: Ag, Au, Cu and Pt. *Surface Science* **306** (1994) 367–380.

[75] A. T. Jennings, M. J. Burek, and J. R. Greer. Microstructure versus Size: Mechanical Properties of Electroplated Single Crystalline Cu Nanopillars. *Physical Review Letters* **104** (2010) 135503.

[76] H. Bei, S. Shim, G. Pharr, and E. George. Effects of Pre-Strain on the Compressive Stress–strain Response of Mo-Alloy Single-Crystal Micropillars. *Acta Materialia* **56** (2008) 4762–4770.

[77] S.-W. Lee, S. M. Han, and W. D. Nix. Uniaxial Compression of Fcc Au Nanopillars on an MgO Substrate: The Effects of Prestraining and Annealing. *Acta Materialia* **57** (2009) 4404–4415.

[78] L. Li, P. Anderson, M. Lee, E. Bitzek, P. Derlet, and H. Swygenhoven. The Stress–strain Response of Nanocrystalline Metals: A Quantized Crystal Plasticity Approach. *Acta Materialia* **57** (2009) 812–822.

[79] A. Roy, S. Kundu, K. Müller, A. Rosenauer, S. Singh, P. Pant, M. P. Gururajan, P. Kumar, J. Weissmüller, A. K. Singh, and N. Ravishankar. Wrinkling of Atomic Planes in Ultrathin Au Nanowires. *Nano Letters* **14** (2014) 4859–4866.

[80] S. Brochard, P. Beauchamp, and J. Grilhé. Stress Concentration near a Surface Step and Shear Localization. *Physical Review B* **61** (2000) 8707–8713.

[81] J. Diao, K. Gall, and M. L. Dunn. Yield Strength Asymmetry in Metal Nanowires. *Nano Letters* **4** (2004) 1863–1867.

[82] Z. W. Shan, R. K. Mishra, S. A. Syed Asif, O. L. Warren, and A. M. Minor. Mechanical Annealing and Source-Limited Deformation in Submicrometre-Diameter Ni Crystals. *Nature Materials* **7** (2008) 115–119.

[83] M. Meyers, A. Mishra, and D. Benson. Mechanical Properties of Nanocrystalline Materials. *Progress in Materials Science* **51** (2006) 427–556.

[84] V. Yamakov, D. Wolf, S. R. Phillpot, A. K. Mukherjee, and H. Gleiter. Deformation-Mechanism Map for Nanocrystalline Metals by Molecular-Dynamics Simulation. *Nature Materials* **3** (2004) 43–47.

[85] J. Weissmüller and J. Markmann. Deforming Nanocrystalline Metals: New Insights, New Puzzles. *Advanced Engineering Materials* **7** (2005) 202–207.

[86] J. Schäfer, A. Stukowski, and K. Albe. On the Hierarchy of Deformation Processes in Nanocrystalline Alloys: Grain Boundary Mediated Plasticity vs. Dislocation Slip. *Journal of Applied Physics* **114** (2013) 143501.

[87] A. Hodge, J. Biener, J. Hayes, P. Bythrow, C. Volkert, and A. Hamza. Scaling Equation for Yield Strength of Nanoporous Open-Cell Foams. *Acta Materialia* **55** (2007) 1343–1349.

[88] G. Pia and F. Delogu. On the Elastic Deformation Behavior of Nanoporous Metal Foams. *Scripta Materialia* **69** (2013) 781–784.

[89] G. Pia and F. Delogu. Nanoporous Au: Statistical Analysis of Morphological Features and Evaluation of Their Influence on the Elastic Deformation Behavior by Phenomenological Modeling. *Acta Materialia* **85** (2015) 250–260.

[90] G. Pia and F. Delogu. Mechanical Properties of Nanoporous Au: From Empirical Evidence to Phenomenological Modeling. *Metals* **5** (2015) 1665–1694.

[91] G. Pia and F. Delogu. A Phenomenological Approach to Yield Strength in Nanoporous Metal Foams. *Scripta Materialia* **103** (2015) 26–29.

[92] S. Ahmadi, G. Campoli, S. Amin Yavari, B. Sajadi, R. Wauthle, J. Schrooten, H. Weinans, and A. Zadpoor. Mechanical Behavior of Regular Open-Cell Porous Biomaterials Made of Diamond Lattice Unit Cells. *Journal of the Mechanical Behavior of Biomedical Materials* **34** (2014) 106–115.

[93] N. Q. Vo, R. S. Averback, P. Bellon, and A. Caro. Yield Strength in Nanocrystalline Cu during High Strain Rate Deformation. *Scripta Materialia* **61** (2009) 76–79.

[94] J. Jiao and N. Huber. Deformation Mechanisms in Nanoporous Metals: Effect of Ligament Shape and Disorder. *Computational Materials Science* **127** (2017) 194–203.

[95] V. Deshpande, M. Ashby, and N. Fleck. Foam Topology: Bending versus Stretching Dominated Architectures. *Acta Materialia* **49** (2001) 1035–1040.

[96] M. Ashby. The Properties of Foams and Lattices. *Philosophical Transactions of the Royal Society A: Mathematical, Physical and Engineering Sciences* **364** (2006) 15–30.

[97] R. T. DeHoff, E. H. Aigeltinger, and K. R. Craig. Experimental Determination of the Topological Properties of Three-Dimensional Microstructures. *Journal of Microscopy* **95** (1972) 69–91.

[98] H. J. Vogel. Morphological Determination of Pore Connectivity as a Function of Pore Size Using Serial Sections. *European Journal of Soil Science* **48** (2008) 365–377.

[99] H. M. Ledbetter and M. W. Austin. Deformed-polycrystalline-copper elastic constants. *Physica Status Solidi (a)* **104** (1987) 203–212.

[100] H. Ledbetter and S. Kim. Low Temperature Elastic Constants of Deformed Polycrystalline Copper. *Materials Science and Engineering: A* **101** (1988) 87–92.

[101] J. A. Benito, J. Jorba, J. M. Manero, and A. Roca. Change of Young's Modulus of Cold-Deformed Pure Iron in a Tensile Test. *Metallurgical and Materials Transactions A* **36** (2005) 3317–3324.

[102] S. Dai, Y. Wang, F. Chen, X. Yu, and Y. Zhang. Effects of Cold Deformation on Microstructure and Mechanical Properties of Ti–35Nb–9Zr–6Mo–4Sn Alloy for Biomedical Applications. *Materials Science and Engineering: A* **575** (2013) 35–40.

[103] H. Liang, M. Upmanyu, and H. Huang. Size-Dependent Elasticity of Nanowires: Nonlinear Effects. *Physical Review B* **71** (2005) 241403.

[104] G. Yun and H. S. Park. Surface Stress Effects on the Bending Properties of Fcc Metal Nanowires. *Physical Review B* **79** (2009) 195421.

[105] L. Y. Chen, G. Richter, J. P. Sullivan, and D. S. Gianola. Lattice Anharmonicity in Defect-Free Pd Nanowhiskers. *Physical Review Letters* **109** (2012) 125503.

[106] G. Wang and X. Li. Size Dependency of the Elastic Modulus of ZnO Nanowires: Surface Stress Effect. *Applied Physics Letters* **91** (2007) 231912.

[107] R. E. Miller and V. B. Shenoy. Size-Dependent Elastic Properties of Nanosized Structural Elements. *Nanotechnology* **11** (2000) 139–147.

[108] G.-F. Wang and X.-Q. Feng. Effects of Surface Elasticity and Residual Surface Tension on the Natural Frequency of Microbeams. *Applied Physics Letters* **90** (2007) 231904.

[109] B. Elsner, S. Müller, S. Bargmann, and J. Weissmüller. Surface Excess Elasticity of Gold: Ab Initio Coefficients and Impact on the Effective Elastic Response of Nanowires. *Acta Materialia* **124** (2017) 468–477.

LIST OF PUBLICATIONS

PEER-REVIEWED ARTICLES

1. Ngô, B. N. D., Stukowski, A., Mameka, N., Markmann, J., Albe, K., & Weissmüller, J. (2015). Anomalous compliance and early yielding of nanoporous gold. *Acta Materialia*, 93, 144-155.
2. Ngô, B. N. D., Roschning, B., Albe, K., Weissmüller, J., & Markmann., J. (2017). On the origin of the anomalous compliance of dealloying-derived nanoporous gold. *Scripta Materialia*, 130, 74-77.

INVITED TALKS

1. Ngô B. N. D. Anomalous compliance of nanoporous gold: On the influence of ligament connectivity and surface effects. Second International Symposium on Nanoporous Materials by Alloy Corrosion. Lake Bostal, Germany, 23 - 27 September 2016.

CONTRIBUTED TALKS AND POSTERS

1. Ngô, B. N. D., Albe, K., & Weissmüller, J. Molecular dynamics study of nanoporous gold deformation. *Contributed talk.* DPG Spring Meeting. Regensburg, 10 - 15 March 2013.
2. Ngô, B. N. D., Stukowski, A., Albe, K., & Weissmüller, J. Compression behaviour of nanoporous gold studied by molecular dynamics simulation. *Contributed talk.* TMS Annual Meeting & Exhibition 2014. San Diego, CA (USA), 16 - 20 February 2014.
3. Ngô, B. N. D., Albe, K., & Weissmüller, J. Deformation of nanoporous gold: On the importance of topology. *Contributed talk.* DPG Spring Meeting. Dresden, 30 March - 04 April 2014
4. Ngô, B. N. D., Stukowski, A., Albe, K., & Weissmüller, J. Plasticity of nanoporous gold: Implications of molecular dynamics simulations. *Contributed talk.* MSE 2014. Darmstadt, 23 - 25 September 2014.

5. Ngô, B. N. D., Stukowski, A., Mameka, N., Markmann, J., Albe, K., & Weissmüller, J. Uniaxial compression of nanoporous gold studied by atomistic simulations. *Poster.* First International Symposium on Nanoporous Materials by Alloy Corrosion. Lake Bostal, Germany, 28 September - 02 October 2014.
6. Ngô, B. N. D., Stukowski, A., Markmann, J., Albe, K., & Weissmüller, J. Modeling nanoporous gold: On the influence of nodal shifting and ligament size distribution. *Contributed talk.* DPG Spring Meeting. Berlin, 15 - 20 March 2015.
7. Ngô, B. N. D., Stukowski, A., Mameka, N., Markmann, J., Albe, K., & Weissmüller, J. Anomalous compliance and early yielding of nanoporous gold. *Poster*. International Workshop on Hierarchical Multi-scale Materials Systems. Hamburg, 4 - 6 November 2015.
8. Ngô, B. N. D., Roschning, B., Stukowski, A., Markmann, J., Albe, K., & Weissmüller, J. How ligament connectivity determines stiffness of nanoporous gold? *Contributed talk.* DPG Spring Meeting. Regensburg, 06 - 11 March 2016.
9. Ngô, B. N. D., Roschning, B., Stukowski, A., Markmann, J., Albe, K., & Weissmüller, J. Anomalous compliance of nanoporous gold: On the influences of the ligament connectivity and surface effects. *Poster.* Gordon Research Conference on Thin Film and Small Scale Mechanical Behavior. Lewiston, ME (USA), 24 - 29 July 2016.

Elasticity and Plasticity of Nanoporous Gold: Implications of Molecular Dynamics Simulations

Summary

Molecular dynamics simulations of compression tests on virtual nanoporous gold samples created by mimicking spinodal decomposition via Monte Carlo simulations reveal an anomalously compliant and weak behavior. This behavior, while in good agreement with experimental data of millimeter-sized dealloyed nanoporous gold, changes drastically once the network connectivity is varied. Topological disorder due to nodal shift also impacts the effective behavior of the material. Yet, on top of the above-mentioned topological descriptors or the solid fraction, atomistic processes, such as dislocation activity and surface effects, must be taken into account in order to explain the observed behavior of the material.

Elastizität und Plastizität von nanoporösem Gold: Implikationen durch molekulardynamische Simulationen

Zusammenfassung

Molekulardynamische Simulationen von Kompressionsprüfungen an virtuellen nanoporösen Goldproben, die durch Nachahmung spinodaler Entmischung durch Monte-Carlo-Simulationen erstellt wurden, zeigen ein ungewöhnlich nachgiebiges und weiches Verhalten. Dieses Materialverhalten, welches in guter Übereinstimmung mit experimentellen Daten an millimetergroßem, entlegiertem nanoporösem Gold ist, verändert sich drastisch, wenn die Netzwerkkonnektivität verändert wird. Topologische Unordnung verursacht durch Verschiebung der Netzwerkknoten nimmt ebenfalls Einfluss auf das effektive Materialverhalten. Dennoch müssen, zusätzlich zu den oben erwähnten topologischen Beschreibungen und des Feststoffanteils, Prozesse auf atomistischer Ebene wie Versetzungsaktivität und Oberflächeneffekte in Betracht gezogen werden, um das beobachtete Materialverhalten erklären zu können.